Design and optimization of a 3D-printed flow system for semi-automated sample preparation

by

Andrea du Preez

A dissertation submitted in partial fulfilment of the requirements for the degree

Master of Science in Chemistry

Faculty of Science

University of Johannesburg

Supervisor: Prof R. Meijboom

Co-supervisor: Dr E. Smit

June 2021

Table of Contents

Acknowledgements

I would like to acknowledge and thank the following: My supervisors, Dr E. Smit, and Prof R. Meijboom, for their guidance during this research project. The late Mr J. A. Hanekom for assistance with building and maintaining the 3D-printed syringe pumps. Dr K. Potgieter for assistance with 3D-printing the chip reactor and a few flangeless fitting pieces. Mr S. Mokhele and Mr M Trivhani for their assistance with analytical laboratory equipment. The University of Johannesburg, especially the Department of Chemical Sciences. The National Research Foundation (NRF) of South Africa (Grant number: 117842) for funding consumables used in this work and the Global Excellence and Stature (GES) 4.0 for funding my bursary.

Declaration

I, **Andrea du Preez**, declare that the work presented here was performed by myself and my supervisors were the only ones involved in planning the research project and also proof-reading the reported work.

List of abbreviations

2D	Two-dimensional
3D	Three-dimensional
ABS	Acrylonitrile butadiene styrene
ANOVA	Analysis of variance
ANSI	American National Standards Institute
ATR-IR	Attenuated total reflectance infrared
BPR	Back-pressure regulator
C9:0	Pelargonic acid / Nonanoic acid
C11:0	Undecyclic acid / Undecanoic acid
C12:0	Lauric acid / Dodecanoic acid
C14 alkene / 14:1 HC	1-tetradecene
C16:0	Palmitic acid / Hexadecanoic acid
C16:1	Palmitoleic acid / (Z)-Hexadec-9-enoic acid
C18:0	Stearic acid / Octadecanoic acid
C18:1	Oleic acid / (Z)-Octadec-9-enoic acid
C18:2	Linoleic acid / (9Z,12Z)-Octadeca-9,12-dienoic acid
C18:3	Linolenic acid / (9Z,12Z,15Z)-Octadeca-9,12,15-trienoic acid
C22:1	Erucic acid / (Z)-Docos-13-enoic acid
CAD	Computer aided design
CDR	Circular disk reactor
CNC	Computerized numerical control
CSTR	Continuous stirred tank reactor
df	Degrees of freedom
ESI-MS	Electrospray ionization mass spectrometer
F	Test statistic
FA	Fatty acid
FAME	Fatty acid methyl ester
F_{crit}	Critical value of the test statistic
FDM	Fused deposition modelling

FFA	Free fatty acids
FID	Flame ionization detector
GC	Gas chromatography
GC-MS	Gas chromatography-mass spectrometry
GUI	Graphical user interface
H_0	Null hypothesis
H_a	Alternative hypothesis
HC	Hydrocarbon
HIPS	High impact polystyrene
HPLC	High-performance liquid chromatography
ID	Inner diameter
IR	Infrared
M	Metric
MJM	Multi-jet modelling
NR	Not reported
OD	Outer diameter
PCL	Polycaprolactone
PEEK	Polyether ether ketone
PEI	Polyetherimide
PET	Polyethylene terephthalate
PETG	Polyethylene terephthalate glycol
PETT	Polyethylene co-trimethylene terephthalate
Ph. Eur.	European Pharmacopoeia
PLA	Polylactic acid
PP	Polypropylene
PTFE	Polytetrafluoroethylene
PVA	Polyvinyl alcohol
QuEChERS	Quick, easy, cheap, effective, rugged, and safe
R^2	Coefficient of determination
SLA	Stereolithography
SLM	Selective laser melting
SLS	Selective laser sintering
STL	Standard tessellation language

TAG	Triacylglycerol
TFE	Tetrafluoroethylene
TMAH	Tetramethylammonium hydroxide
TMPAH	Trimethylphenylammonium hydroxide
UNF	Unified National Fine
USB	Universal serial bus
UV-Vis	Ultraviolet-visible

Abstract

A low-cost, mostly 3D-printed flow system was designed, manufactured, and evaluated for performing base-catalyzed transesterification of triacylglycerols, in order to determine the fatty acid content of edible oils. The proposed methodology in conjunction with traditional chromatographic analysis, provides a semi-automated sample preparation procedure which requires minimal manual intervention. Specifically, the preparation of reagent mixtures and the transfer of products to gas chromatographic (GC) vials for analysis was carried out manually. Due to enhanced reactivity in flow, lower base-catalyst concentrations (1-1.5 wt.%) were required compared to traditional batch reactions (5 wt.%). The flow system consists primarily of syringe pumps, connectors (i.e., flangeless fittings), and reactors, that were self-manufactured using 3D-printing technology, specifically, fused deposition modelling (FDM). Print settings were fine-tuned to obtain high-quality leak-tight flangeless fittings in polypropylene (PP). The mostly 3D-printed flow system was successfully used to determine the fatty acid content of certified and commercial sunflower oil. Furthermore, additional commercial edible oils (avocado oil, canola oil, extra virgin olive oil, and a blend of canola and olive oil) were analyzed. The obtained results, expressed as a percentage of total fatty acid methyl ester content, were comparable to certified and literature values.

Graphical abstract

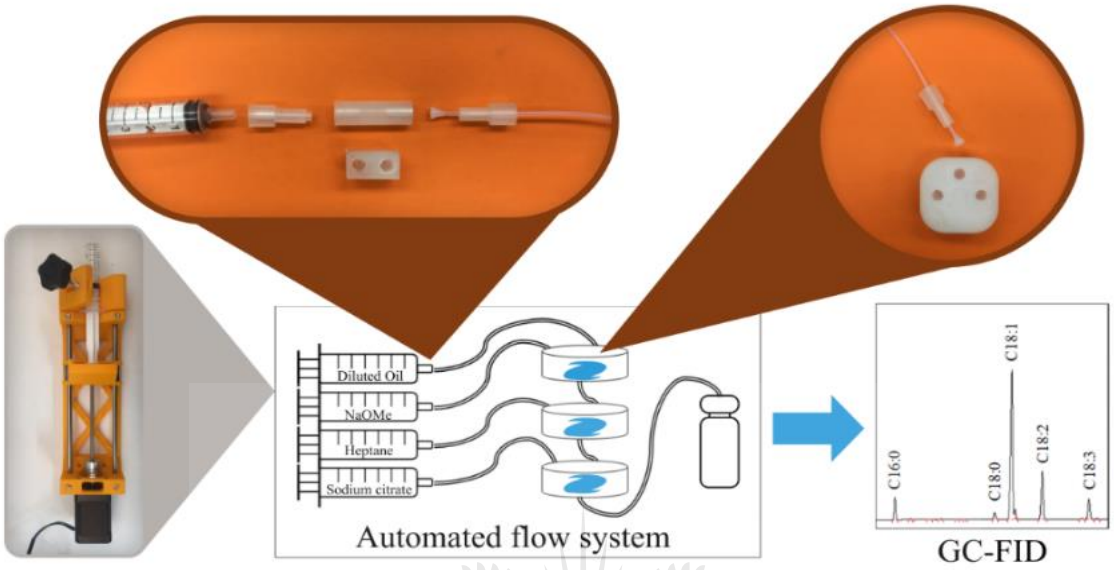

Chapter 1: Introduction

1.1. Background

Analytes are primarily derivatized to increase volatility and reduce polarity, making it more amendable for gas chromatographic analysis [1,2]. In many instances, analytes are derivatized manually. Although these manual batch protocols are relatively simple, they are often laborious and time-consuming [3]. Specialized commercial instruments (i.e., high-end autosamplers) have been demonstrated to perform simple derivatization reactions automatically with direct injection of the final reaction mixture into the gas chromatograph [4,5]. Unfortunately, the costs involved for these fully automated systems do not always outweigh its benefits.

An alternative approach would be to perform derivatization reactions in flow. Reactions in flow have several well-documented advantages compared to conventional batch procedures. These advantages include efficient mixing and precise control of reaction parameters (e.g., temperature and pressure) due to the high surface-to-volume ratios of flow reactors [6]. Furthermore, a flow synthesis improves selectivity and yield because undesired side reactions are minimized, which is usually caused by insufficient mixing and poor heat exchange rates [6,7]. Flow processes are also inherently safer for a multitude of reasons including lower reaction volumes [8], rapid heat dissipation [9], and the ability to accommodate higher pressures [8].

To the best of our knowledge, Ballesteros et al. [10] was the first to develop an automated flow system with in-line GC analysis for the direct determination of the fatty acid content of olive oil and other vegetable oil types in 1993. The authors used a coiled tube reactor that was 500 cm in length with an inner diameter of 0.5 mm. A major disadvantage of their flow system was the required 15 minute long pause to allow for complete transesterification of triacylglycerols. In more recent years, the use of fluidic chip reactors have been demonstrated as an alternative to coiled reactor types [11]. Duong and Roper [12] developed a microfluidic chip using conventional photolithography and wet etching techniques, specifically for the derivatization of free fatty acids with methanolic hydrochloric acid, to produce the corresponding fatty acid

methyl esters. However, the high fabrication costs associated with microreactors [13] in combination with exorbitantly priced commercial flow equipment [7,14] has led to the development of low-cost reactionware for flow chemistry purposes. These low-cost flow systems mainly consist of open-source syringe pumps [15–18] and various flow components [18–23] that have been fabricated by using additive manufacturing in some way.

Even though the significance of 3D-printing in both analytical sample preparation [24] and open-source strategies in separation science [25] have been reviewed, there are surprisingly no reports showcasing the potential of 3D-printing reactionware for the derivatization of triacylglycerols in edible oils using continuous flow. Thus, the work presented here demonstrates the development of a low-cost, mostly 3D-printed, flow system for the automated derivatization of triacylglycerols in edible oils prior to GC analysis.

1.2. Aims and objectives

The aim of this study was to develop a low-cost continuous flow sample preparation method for the base-catalyzed transesterification of triacylglycerols in edible oils. The objectives were to: (i) reproduce the open-source Poseidon syringe pump system as reported by Booeshaghi et al. [16] (ii) calibrate the flow rates of each syringe pump in a set, (iii) design and/or modify various flow components (i.e., connectors and reactors) using computer aided design software, (iv) fabricate various flow components using 3D-printing technology, (v) optimize reaction parameters (i.e., reactor type, flow rate and base-catalyst concentration) for the transesterification of triacylglycerols in edible oils, (vi) compare the proposed flow method to its batch counterpart, (vii) determine the fatty acid content of certified and commercial edible oils using GC-FID, and (viii) compare the fatty acid content of the analyzed edible oils to certified and literature values.

1.3. Problem statement

Automated sample preparation procedures hold great advantages such as minimal sample handling, improved throughput and reproducibility. However, the implementation thereof is often hindered by the prohibitive costs of the equipment. Therefore, a low-cost flow system was developed to automate the base-catalyzed transesterification of triacylglycerols in edible oils. The costs involved were reduced significantly by fabricating the main flow system components that consists of open-source syringe pumps, flangeless fittings, and reactors using 3D-printing technology.

1.4. Hypothesis

A mostly 3D-printed flow system is a low-cost and effective alternative for the base-catalyzed transesterification of triacylglycerols in edible oils.

1.5. Organization

This study is divided into five chapters. Chapter 1 provides a general introduction to the work presented here. Furthermore, an in-depth literature review is given in Chapter 2 where the basic principles and concepts of flow chemistry, 3D-printed reactionware, and transesterification are discussed. Chapter 3 and Chapter 4 are structured similarly with three main sections namely: The Poseidon syringe pump system, 3D-printed flow components, and the base-catalyzed transesterification of triacylglycerols in edible oils. The main difference between these chapters is that Chapter 3 describes all the experimental parameters, whereas Chapter 4 provides detailed discussions and interpretation of experimental results. In Chapter 5, concluding remarks and future recommendations are made. Finally, the Appendices provide supplementary information to the reader with regards to Chapter 3 to Chapter 4.

1.6. References

[1] H.L. Lord, E.A. Pfannkoch, Sample Preparation Automation for GC Injection, in: Comprehensive Sampling and Sample Preparation, Elsevier, 2012: pp. 597–612. https://doi.org/10.1016/B978-0-12-381373-2.00061-2.

[2] Z. Wu, Q. Zhang, N. Li, Y. Pu, B. Wang, T. Zhang, Comparison of critical methods developed for fatty acid analysis: A review, Journal of Separation Science. 40 (2017) 288–298. https://doi.org/10.1002/jssc.201600707.

[3] E. Tammekivi, S. Vahur, O. Kekišev, I.D. van der Werf, L. Toom, K. Herodes, I. Leito, Comparison of derivatization methods for the quantitative gas chromatographic analysis of oils, Analytical Methods. 11 (2019) 3514–3522. https://doi.org/10.1039/C9AY00954J.

[4] S. de Koning, B. van der Meer, G. Alkema, H.-G. Janssen, U.A.Th. Brinkman, Automated determination of fatty acid methyl ester and cis/trans methyl ester composition of fats and oils, Journal of Chromatography A. 922 (2001) 391–397. https://doi.org/10.1016/S0021-9673(01)00926-8.

[5] B. Schilling, R. Bolliger, G. Boehm, Automated Workflow for the Transesterification of Fatty Acid Methyl Esters (FAME) in Fat and Fat Containing Food Samples Using a 90 Sec. Transesterification, https://www.palsystem.com/fileadmin/public/docs/Downloads/Posters/Automated_Generation___Analysis_of_FAME_GC_ISCC_Riva_2014_Poster.pdf (accessed September 30, 2020).

[6] G. Scotti, S.M.E. Nilsson, V.-P. Matilainen, M. Haapala, G. Boije af Gennäs, J. Yli-Kauhaluoma, A. Salminen, T. Kotiaho, Simple 3D printed stainless steel microreactors for online mass spectrometric analysis, Heliyon. 5 (2019) e02002. https://doi.org/10.1016/j.heliyon.2019.e02002.

[7] F.M. Akwi, P. Watts, Continuous flow chemistry: where are we now? Recent applications, challenges and limitations, Chemical Communications. 54 (2018) 13894–13928. https://doi.org/10.1039/c8cc07427e.

[8] M. Baumann, T.S. Moody, M. Smyth, S. Wharry, A Perspective on Continuous Flow Chemistry in the Pharmaceutical Industry, Organic Process Research and Development. (2020). https://doi.org/10.1021/acs.oprd.9b00524.

[9] C.R. Sagandira, M. Siyawamwaya, P. Watts, 3D printing and continuous flow chemistry technology to advance pharmaceutical manufacturing in developing countries, Arabian Journal of Chemistry. 13 (2020) 7886–7908. https://doi.org/10.1016/j.arabjc.2020.09.020.

[10] E. Ballesteros, M. Gallego, M. Valcárcel, Automatic method for on-line preparation of fatty acid methyl esters from olive oil and other types of oil prior to their gas chromatographic determination, Analytica Chimica Acta. 282 (1993) 581–588. https://doi.org/10.1016/0003-2670(93)80123-3.

[11] S.J. Haswell, P. Watts, Green chemistry: synthesis in micro reactors, Green Chemistry. 5 (2003) 240–249. https://doi.org/10.1039/b210539j.

[12] C.T. Duong, M.G. Roper, A microfluidic device for the automated derivatization of free fatty acids to fatty acid methyl esters, The Analyst. 137 (2012) 840–846. https://doi.org/10.1039/C2AN15911B.

[13] B.P. Mason, K.E. Price, J.L. Steinbacher, A.R. Bogdan, T.D. McQuade, Greener approaches to organic synthesis using microreactor technology, Chemical Reviews. 107 (2007) 2300–2318. https://doi.org/10.1021/cr050944c.

[14] J.H. Bannock, S.H. Krishnadasan, M. Heeney, J.C. de Mello, A gentle introduction to the noble art of flow chemistry, Materials Horizons. 1 (2014) 373–378. https://doi.org/10.1039/c4mh00054d.

[15] M.S. Cubberley, W.A. Hess, An inexpensive programmable dual-syringe pump for the chemistry laboratory, Journal of Chemical Education. 94 (2017) 72–74. https://doi.org/10.1021/acs.jchemed.6b00598.

[16] A.S. Booeshaghi, E.d.V. Beltrame, D. Bannon, J. Gehring, L. Pachter, Principles of open source bioinstrumentation applied to the poseidon syringe pump system, Scientific Reports. 9 (2019) 1–8. https://doi.org/10.1038/s41598-019-48815-9.

[17] B. Wijnen, E.J. Hunt, G.C. Anzalone, J.M. Pearce, Open-source syringe pump library, PLoS ONE. 9 (2014). https://doi.org/10.1371/journal.pone.0107216.

[18] J.M. Neumaier, A. Madani, T. Klein, T. Ziegler, Low-budget 3D-printed equipment for continuous flow reactions, Beilstein Journal of Organic Chemistry. 15 (2019) 558–566. https://doi.org/10.3762/bjoc.15.50.

[19] G.W. Bishop, J.E. Satterwhite, S. Bhakta, K. Kadimisetty, K.M. Gillette, E. Chen, J.F. Rusling, 3D-Printed fluidic devices for nanoparticle preparation and flow-injection amperometry using integrated prussian blue nanoparticle-modified electrodes, Analytical Chemistry. 87 (2015) 5437–5443. https://doi.org/10.1021/acs.analchem.5b00903.

[20] V. Dragone, V. Sans, M.H. Rosnes, P.J. Kitson, L. Cronin, 3D-printed devices for continuous-flow organic chemistry, Beilstein Journal of Organic Chemistry. 9 (2013) 951–959. https://doi.org/10.3762/bjoc.9.109.

[21] P.J. Kitson, M.H. Rosnes, V. Sans, V. Dragone, L. Cronin, Configurable 3D-Printed millifluidic and microfluidic "lab on a chip" reactionware devices, Lab on a Chip. 12 (2012) 3267–3271. https://doi.org/10.1039/c2lc40761b.

[22] M.T. Vangunten, U.J. Walker, H.G. Do, K.N. Knust, 3D-Printed Microfluidics for Hands-On Undergraduate Laboratory Experiments, Journal of Chemical Education. 97 (2020) 178–183. https://doi.org/10.1021/acs.jchemed.9b00620.

[23] M.J. Harding, S. Brady, H. O'Connor, R. Lopez-Rodriguez, M.D. Edwards, S. Tracy, D. Dowling, G. Gibson, K.P. Girard, S. Ferguson, 3D printing of PEEK reactors for flow chemistry and continuous chemical processing, Reaction Chemistry and Engineering. 5 (2020) 728–735. https://doi.org/10.1039/c9re00408d.

[24] F. Li, M.R. Ceballos, S.K. Balavandy, J. Fan, M.M. Khataei, Y. Yamini, F. Maya, 3D Printing in analytical sample preparation, Journal of Separation Science. 43 (2020) 1854–1866. https://doi.org/10.1002/jssc.202000035.

[25] J.J. Davis, S.W. Foster, J.P. Grinias, Low-cost and open-source strategies for chemical separations, Journal of Chromatography A. 1638 (2021). https://doi.org/10.1016/j.chroma.2020.461820.

Chapter 2: Literature review

2.1. Flow chemistry principles: Concept, parameters, and components

A flow process can be described as the performance of chemical reactions in channels or tubing instead of standardized glassware [1]. Flow processes are known to be safer [1–4] compared to batch processes because reactions occur at lower volumes, more controlled reaction temperatures, and higher pressures can be accommodated without much risk [1]. Additional advantages over conventional batch procedures include efficient mixing of substrates, improved heat and mass transfer, and shorter reaction times [2,5,6].

A key difference between a reaction carried out in batch mode versus in flow mode, involves substrate concentration changes as the reaction proceeds [4,7]. In a batch mode protocol, the substrate is evenly distributed throughout the flask. The substrate concentration decreases while the product concentration increases over a set reaction time. In flow mode, the substate concentration decreases while travelling down a reactor unit. This concentration reaches a minimum at the reactor outlet. In other words, product yield reaches a maximum at the reactor outlet. The amount of time a substrate spends in a reactor unit is called the residence time. The residence time (t_{res}) of a flow reactor can be calculated from the volume or length (V) of a reactor and the overall flow rate (v) [4,7,8].

$$t_{res} = \frac{V}{v} \quad (1)$$

The overall flow rate is calculated by the sum of all incoming reagent streams. Residence time can be manipulated by changing flow rate and reactor length or volume to obtain optimal reaction conditions [4,7,8].

A standard continuous flow system can be divided into eight basic parts. Each part contributes to the overall success of the flow system. These parts are fluid and reagent delivery systems,

mixing, reactor, quenching, pressure regulation, and sample collection (Figure 2.1). The remaining two parts are in-line analysis and purification techniques which rely on conventional methods and are considered optional [7].

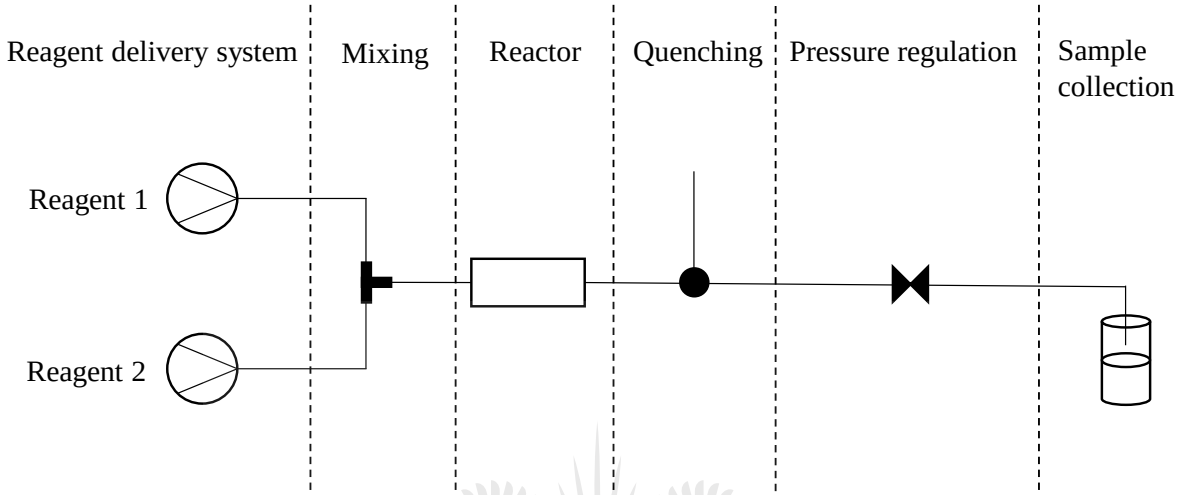

Figure 2.1: *General scheme depicting six of the eight basic parts of a typical flow system (adapted from Plutchack et al. [7]).*

The first part is the fluid and reagent delivery system which facilitates accurate and reliable fluidic flow throughout the entire flow system. Fluidic control in a flow process is crucial because it regulates the residence time and influences the stoichiometry when at least two reagents are combined via a mixer [7]. In flow processes there are two classes of pumping techniques: hydrodynamic flow (pressure-driven pumping) and electro-osmotic (electrokinetic) flow [9,10]. In this work, the focus was on pressure-driven pumping techniques exclusively, because it is the most straightforward fluidic control technique and devices can be constructed out of inexpensive material.

In a pressure-driven flow process, reagents move from the reactor inlet to the outlet via positive displacement. In other words, positive pressure is applied to the reactor inlet, while the discharge zone (outlet) is open to atmospheric pressure. Hydrodynamic flow is affected by channel size, because capillary resistance increases with a decrease in channel size. Thus, only relatively slow flow rates should be considered [9]. Moreover, hydrodynamic pumping techniques result in a parabolic velocity profile [7,9]. This means that the fluid moves faster in

the center of the channel than near the channel walls (Figure 2.2). This could lead to non-uniformity of diffusion coefficients and a distribution of residence time. Thus, a decrease in yields and selectivities could be of consequence [7,9,10].

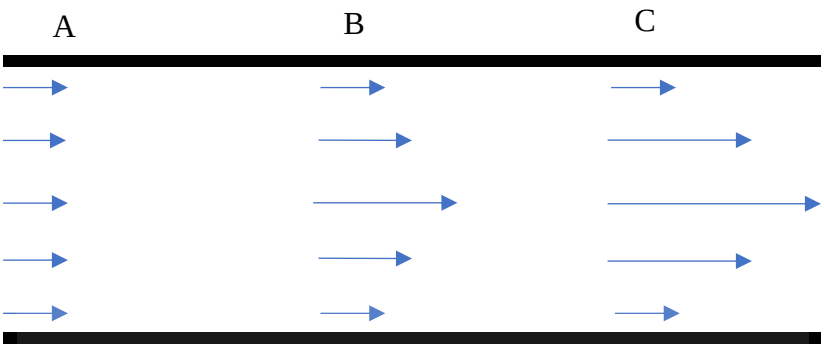

Figure 2.2: *The parabolic velocity profile at the (A) beginning of the channels. As the flow (B, C) progresses through the channels, the liquid moves faster in the middle compared to that at the channel walls (adapted from Mason et al. [9]).*

There are three types of pumps commonly used in flow processes: Piston pumps, syringe pumps, and peristaltic pumps [8]. Choosing the best pumping system to suit the predetermined reaction conditions (system pressure, flow rate and liquid viscosity) is crucial when performing a reaction in flow.

Syringe pumps are equipped with at least one syringe connected to a motorized pushing mechanism that moves the plunger. This movement provides a constant linear flow through each component in the flow system [8]. A syringe pump can only dispense a predetermined amount of liquid over a defined amount of time. Hence reaction time and scale are limited. Moreover, standard versions cannot operate under high pressure conditions [11]. Dual syringe pumps have two independent syringes that operate in sync. In other words, while one syringe dispenses the liquid through the flow system, the other is being filled at the same time. These syringes can also interchange roles [12]. A disadvantage of syringe pumps used in flow are fouling which can occur due to solid formation in reaction channels [9]. In addition, pulsation can be problematic at low flow rates, however this can be overlooked for material synthesis when higher flow rates are more commonly used [13].

The second basic element in a flow system is properly combining at least two reagent streams. This is achieved via a mixer. The mixing principles in flow processes can be divided into two main classes: active and passive mixing [14,15]. Active mixing relies on external energy sources to improve mixing within a flow reactor [15]. A simple example is a magnetic stirrer [16]. Whereas passive mixing relies on the flow energy. In other words, passive mixing occurs due to a combination of pumping speed and flow path [15].

There is a wide variety of mixing techniques available for small scale flow chemistry processes. The simplest and most cost-effective way of combining two or three reagent streams is by using a commercial T-mixer (or a Y-shaped mixer) or a quad-mixer, respectively. These mixers are manufactured in polymers (e.g., polyether ether ketone) and stainless steel [8,13]. Static mixers are a type of mixer that uses fixed shapes inside channels that split, twist, and recombine fluids [14,17] to induce chaotic mixing by eddy formation [15,18]. A packed bed reactor (see below) containing sand, stainless steel chippings, or glass beads can also be used to provide efficient mixing [3].

The third element in a flow system is a reactor. A reactor in a flow system refers to at least one specific place in a flow process where a chemical transformation takes place. Examples of reactors are coil reactors, chip reactors, packed bed reactors, and continuous stirred tank reactors (CSTRs) (Figure 2.3).

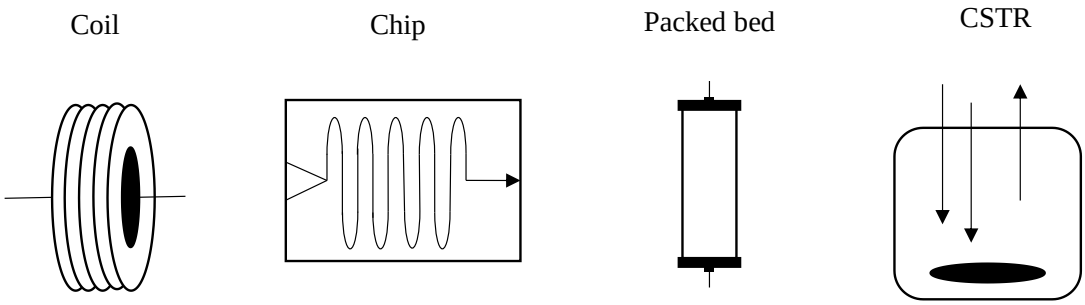

Figure 2.3: *Typical reactors used in flow systems.*

Coil reactors are one of the most popular flow reactors, because it is inexpensive and come in a wide variety of materials such as inert fluoropolymers, stainless steel or special alloys such as Hastelloy [3,7,19]. In addition, these reactors have outer diameters (ODs) of 1/8", 1/16" or 1/32" and various inner diameters (IDs) that can range from 0.01" to 0.04" and 1/16" [7,8]. Stainless steel coil reactors are the best choice when working under elevated temperatures and pressures but is not suited for extremely corrosive conditions. Thus, inert fluoropolymers such as polytetrafluoroethylene (PTFE) or Hastelloy coil reactors can be used instead [7]. One unique advantage of coil reactors is that it can be constructed from catalytically active material, such as copper, to carry out reactions, such as 1,3-dipolar cycloadditions, Sonogashira C-C couplings and Ullmann couplings [19].

Chip reactors are also known as "lab-on-chip" systems [20] can be made from glass, quartz, polymers or stainless steel by specialized manufacturing techniques such as etching, sintering and 3D-printing, to name a few [6,8,9]. Therefore, chip reactors can be either expensive or rather inexpensive depending on the manufacturing technique. Chip reactors usually incorporates a dedicated mixing zone with a multitude of channels with internal volumes that can range from 1 μL to 1 mL [8,20]. The major advantage of chip-based reactors compared to others is that it offers the superior heat transfer capabilities due to high surface-to-volume ratios [6].

Packed bed reactor units are utilized when heterogeneous catalysts or reagents are required to carry out chemical transformations [21,22]. These reactors are cartridge-like tubes made from stainless steel, glass, or polymeric materials where the catalyst is directly packed into the reactor [7]. The catalyst is therefore contained inside the reactor channel and only chemical reagents can enter and products can leave the reactor unit. Thus, reaction and filtration operations occur simultaneously [23]. Consequently, the catalyst is easily recycled [24]. Even though packed bed reactors are considered one of the most straightforward, convenient, and sustainable methods in synthetic flow chemistry [24], there are a few limitations such as uncontrolled fluid dynamics [22], large pressure drop and clogging (both due to small particle size) [25], heat transfer limitations [22], and catalyst leaching [7].

A CSTR is a reactor type that may be relatively large in comparison to the other reactor types. The reagent streams enter a tank where a reaction takes place, followed by the product stream exiting the reactor tank. This process of reagents entering and products leaving the tank occurs simultaneously. Thus, the reactor volume stays constant throughout the reaction [17].

Heating or cooling techniques are usually applied to the reactor in the flow system. Before selecting a heating and/ or cooling technique for a flow system, the thermal resistance of all components should be considered. Specifically, the fabrication material of the reactor, tubing, and connections. For low-cost conventional heating methods, a reactor can be submerged into a traditional water (<95 °C) or oil bath (<300 °C) [3,7,13,26]. Alternatively, more specialized and expensive approaches such as microwave irradiation [26–29] or inductive heating techniques [27,28] can be considered. Reactors can also be submerged into a dedicated cooling bath with ice (<25 °C) [3] or a dry-ice and ethanol mixture (>-78 °C) [8] when cooling of the reaction mixture is required. Alternatively, more consistent, and reliable cryogenic cooling units [7] can also be considered if a reaction requires cooling down to -80 °C [8].

The reaction termination step (quenching) is the fourth essential component in a flow system. This step is dependent on the type of reaction carried out in flow and might not be necessary if the reaction is terminated after products leave the reactor [7]. A quenching reagent can also be incorporated into the flow system by placing an additional mixer or CSTR directly after the reactor. Solution-based quenching followed by phase separation can be achieved by using microseparators containing a hydrophobic membrane to separate aqueous and organic phases [30].

Back-pressure regulators (BPRs) are the fifth essential component in a flow system. BPRs are simple, spring-controlled flow-through valves that can maintain constant upstream pressure assuring constant flow rates [8]. Furthermore, pressuring the flow system allows for reactions to be performed at 100 to 150 °C above boiling point, thus increasing reaction rates up to 1000 times [31]. Furthermore, BPRs prevent the formation of gas bubbles [6]. The sixth element involves sample collection which can be done manually, by collecting products in a vial for

analysis. Alternatively, in-line analysis and purification can be incorporated into the flow system.

Another essential component in flow chemistry is the way in which each basic part is connected to tubing. That is, from the pumps to the mixer, followed by the reactor and so on. This significantly influences the overall performance of a flow system as it is the least reliable component and the first place a leak will be observed. Moreover, this interfacing of fluidic devices and peripherals (external pumps, tubing, etc) can significantly contribute to the overall system cost. Ideally, all connections should (1) have minimal dead volume, (2) avoid cross-contamination of samples, (3) be easy to insert, (4) be removable and reusable, (5) be chemically inert, (6) low-cost, (7) be reliable (i.e., leak free) at standard operating conditions, (8) be compatible with commercial tubing and fittings, and (9) have minimal pressure drop [32,33].

Informative review articles have been published explaining the various methods available to go about connecting the micro-components of a microfluidic device to the macro-environment, specifically when using devices with channel dimensions of orders of microns that can receive fluids in the range of nanolitres (nL) or picolitres (pL) [32,33]. However, when working at a larger scale specifically in the millilitre range, standardized commercial connections and fittings can be implemented without much difficulty.

Good quality fluidic connectors that provide secure, leak-free connections are required to connect tubing to each basic part in a flow system [13,34]. For example, Luer-Lock couplings can be used to connect tubing to syringes. Threaded nuts and ferrules are used to connect tubing to flow accessories such as mixers and reactors. Ferrules are compression fittings that slide over the end of tubing and when secured in place via a nut forms a liquid-tight seal. Commercial nuts and ferrules are usually made from chemically resilient materials such as polyether ether ketone (PEEK) and should only be used under low to medium pressure conditions (<30 bar) [13]. Commercial high-performance liquid chromatography (HPLC) fittings that are well-suited for high pressure conditions are also available and are usually made from stainless steel

[8]. By using these connectors, reactors, and flow accessories, a range of flow configurations can be assembled for multistep reaction protocols and for reaction scale up.

In its simplest form, a linear flow system configuration (Figure 2.4A) can be used in the synthesis of a single product. This is an iterative process where one reactor is placed after the other. Each reactor is responsible for a single transformation until the desired product is obtained. Alternatively, a convergent flow strategy (Figure 2.4C) can be used to synthesize individual fragments of a target molecule. These fragments can be combined towards the end of a flow system to obtain a single product. A divergent flow configuration is utilized when multiple products are synthesized simultaneously (Figure 2.4B) [8,23]. Furthermore, reaction scale up is known to be less problematic in comparison to a batch protocol. There are three approaches to scale up a flow reaction: simply run the process for longer (i.e., scaling-out), use larger reactors (scaling-up), or use multiple reactors placed in a parallel configuration (Figure 2.4D), which is also known as numbering up [23,24].

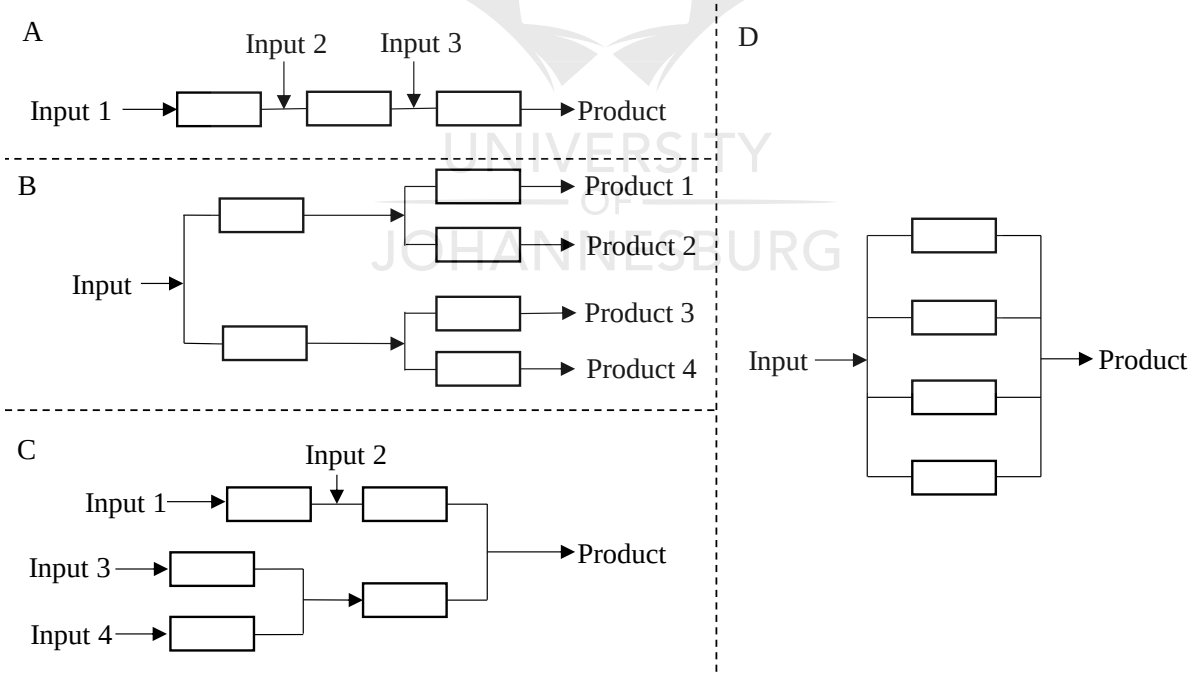

Figure 2.4: *Flow system configurations for different synthetic needs with arbitrary flow reactors. (A) Linear flow configuration. (B) Divergent configuration. (C) Convergent flow configuration. (D) Parallel configuration (adapted from Jas et al. [23]).*

2.2. Off-the-shelf equipment: limitations and associated consequences for research laboratories

Despite all the advantages flow chemistry has to offer in comparison to batch reactions, it has not been widely implemented in research laboratories [1], especially in developing countries. The main reason for this is the prohibitive cost of flow equipment. Moreover, fully integrated commercial flow systems not only come with hefty price tags and exorbitant service contracts, but some reactions parameters might lie outside of the scope of the flow system due to design limitations. Therefore, it is important to realize that no single commercial flow system will be able to carry out all the desired reactions [13]. Even a flow system that has been put together piece-by-piece by readily available commercial parts, such as syringe pumps, fittings, and various flow reactors, could still end up being too expensive for the average research laboratory in a developing country. Thus, a do-it-yourself approach is essential, where flow chemistry reactionware that is inexpensive, robust, and versatile is developed. This can be achieved by combining modern open-source hardware, software, and 3D-printing technology.

2.3. Additive manufacturing

2.3.1. Basic principles of computer aided design for additive manufacturing

Creating three-dimensional (3D) objects start with a conceptualization process, followed by the design and fabrication (Figure 2.5) steps. In additive manufacturing, the design process is independent of the type of 3D-printer utilized and usually starts with the use of computer aided design (CAD) software [35,36] where a complex 3D object is realized by simply combining or subtracting primitive shapes. Most professional CAD software, and some open-source software, can be challenging to master without prior design experience; however, user-friendly versions are widely available free of charge [37] and sometimes only require an internet connection. Alternatively, a 3D-scanner can be used to digitize existing objects [38] or user-created digital design files can be downloaded from online sources. Digital design files are usually saved as standard tessellation language (STL) files which describes the surface geometry of the 3D model in the form of triangulated sections, where each vertex coordinate

is defined in a text file [36,39]. The next step is to convert the STL file to a G-code using slicer software. This software converts the stored information from the STL file into two-dimensional (2D) horizontal cross-sections which allows the 3D object to be fabricated, starting from the foundation, in consecutive layers [35,36,39]. During the slicing process, various parameters (size, orientation, print speed, layer height, extruder and bed temperature, support material etc.) can be fine-tuned to obtain a high-quality 3D object [36,37].

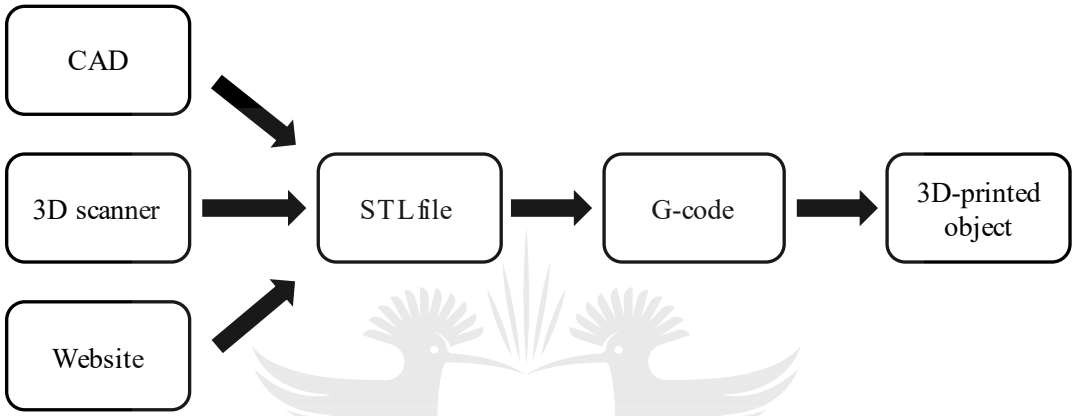

Figure 2.5: *The multi-step design and fabrication process for creating a 3D-printed object. An STL file is obtained by either designing a 3D object using any CAD program. Alternatively, a 3D scanner can copy a physical object or a shared digital design file can be downloaded from the internet. Once the STL file is obtained, it is converted to a G-code via slicing software. This file format requires various printing paraments to be set to obtain a high-quality object. The G-code is then transferred to the 3D-printer to print the object in a layer-by-layer fashion (adapted from V. Saggiomo [37]).*

2.3.2. Basic principles of fused deposition modelling

Fused deposition modelling (FDM) was patented in 1989 by Stratasys LTD co-founder, Scott Crump [36,40]. This technology is currently one of the most popular 3D-printing techniques because it is safe, reliable, and easy to operate but, more importantly, the printer itself and its thermoplastic materials is relatively inexpensive compared to other 3D-printing techniques [37,40]. The only disadvantage of FDM printers is that it has a lower resolution compared to other 3D-printer types [41].

In its simplest form, a pinch roller system (Figure 2.6B) feeds thermoplastic filament (1.75 mm or 3.00 mm diameter) [36,42] reeled on a spool (Figure 2.6A) through a temperature controlled and movable print head (Figure 2.6C) where semimolten material exit the nozzle tip (Figure 2.6E) of the extruder as a thin wire [42,43]. The extruder temperature is usually maintained slightly above the melting point of the thermoplastic filament [44] to allow an easy flow of semimolten material through the extruder nozzle [40]. The print head moves in pre-defined patterns and deposits the semimolten material for each cross-sectional layer (Figure 2.6F) onto a heated build platform (Figure 2.6G) [45]. The semimolten material solidifies shortly after being extruded in the predetermined location on the build platform or on top of a previous layer. This process is repeated for each layer until the target 3D object is obtained [36].

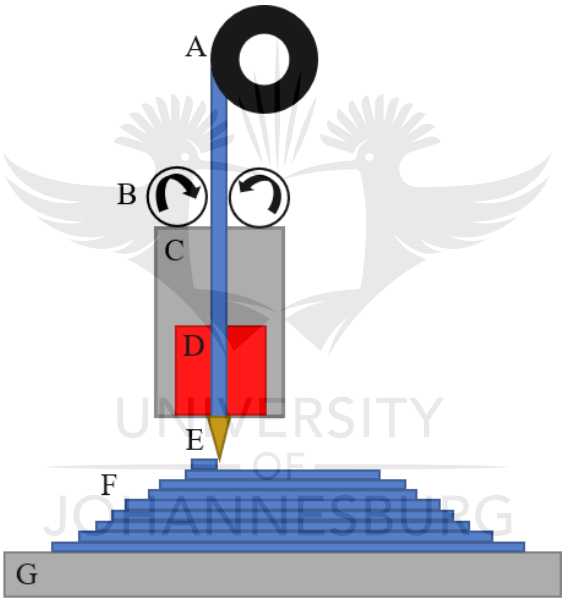

Figure 2.6: *Schematic illustration of a FDM 3D-printer (adapted from Rossi et al. [36]). (A) Thermoplastic filament spool. (B) The pinch roller system that feeds the filament through the extruder. (C) The extruder, also known as the print head. (D) The temperature control unit that heats the filament to a semimolten state. (E) The extruder nozzle that deposits semimolten filament in the form of a thin wire. (F) 3D-printed layers of the predesigned object. (G) The build platform, also known as the print bed.*

With FDM, the 3D-printed object can be handled soon after fabrication and material wastage is relatively low, since only the required amount of material is used to 3D-print the object and

its support material. Generally, post-processing is seldom required except for support material removal and to enhance the surface finish of the object [40,41]. Depending on the design, support material may not be required.

A notable advantage of FDM is that it can accommodate multiple extruders for multi-material fabrication. In other words, objects can be 3D-printed using different polymers in a single print [36,39,41,43]. This methodology is usually applied to fabricate intricately designed objects [40] or to deposit sacrificial support material during the build process [43]. The most typically used thermoplastic filament for FDM fabrication is polylactic acid (PLA) and acrylonitrile butadiene styrene (ABS) [44]. However, many other polymers, such as polyvinyl alcohol (PVA), polyethylene terephthalate (PET), polyethylene terephthalate glycol (PETG), polycarbonate, high impact polystyrene (HIPS), polycaprolactone (PCL), polyethylene co-trimethylene terephthalate (PETT), polypropylene (PP) and nylon are also commercially available [35,36,44].

PLA is an eco-friendly, biodegradable, and renewable thermoplastic polyester that consist of a linear aliphatic polyester chain [46] (Figure 2.7) that is mainly derived from corn starch [47]. It is used commercially as packaging films, containers, bottles, and foodware [47] and it is also a well-known and established thermoplastic filament for FDM printing with good reproducibility and mechanical strength [46]. However, practical applications for organic synthesis are limited because of low thermal stability [47] and its restricted chemical resistance to acidic media and organic solvents [46].

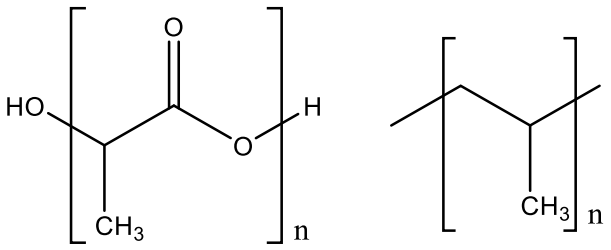

PLA PP

Figure 2.7: *The structures of polylactic acid (PLA) [47] and polypropylene (PP) [48].*

PP is a downstream petrochemical product derived from propylene through addition polymerization. It is a vinyl polymer in which methyl groups are bonded to alternating carbon atoms on one side of the polymer backbone (Figure 2.7). This is also known as the isotactic stereospecific configuration of PP [48]. Contrasting to the properties of PLA, polypropylene is well-known for its excellent chemical resistance and good thermal stability, which makes it better suited for reactionware fabrication [49,50]. In detail, PP can be described as having exceptional resistance towards concentrated and consequently diluted acids, alcohols, and bases. It has adequate resistivity towards aldehydes, esters, aliphatic hydrocarbons, and ketones with limited chemical inertness towards oxidizing agents as well as aromatic and halogenated hydrocarbons [48]. It is also a thermoplastic that is flexible, tough, and lightweight (because of its low density of 0.90 g/cm^3) [48]. Unfortunately, PP is one of the materials that is known to be difficult to 3D-print with FDM [51]. This has been reported to be due to its semi-crystalline nature [48] that causes it to cool and harden differently, which leads to an increase in material stress that consequently could lead to warping and poor bed adhesion [52].

Recently, PEEK has been used as printing material [53]. PEEK has a high tensile strength, excellent thermal stability, and is highly resistant to most laboratory solvents. However, to print using PEEK filament requires an advanced and high temperature FDM printer. These printers come with a hefty price tag which makes it inaccessible for most research laboratories, especially in developing countries. As it currently stands, PP is the most affordable chemical resistant printing material and can be used with most desktop FDM 3D-printers [34].

Common troubleshooting methods were summarized by Kitson et al. [45] when using PP as printing material. For example, if a 3D-printed object is detaching from the printer bed, the surface or material of the bed is not compatible with PP. The authors mentioned simple solutions such as using printer beds made from glass or carbon fibre. Alternatively, covering the bed with glue (from a glue stick) or applying a layer of masking tape could resolve the problem. Another common challenge often encountered would be leaky reactionware. Possible reasons could be underextrusion, wrong infill structure, or not enough solid layers before the infill. There are printing settings (number of solid layers, infill, and flow multiplier) in the slicing software that can be fine-tuned in order to resolve these problems.

In general, the learning curve for all aspects of 3D-printing is steep especially for students and researchers without prior experience. However, there is a lot to learn from open-source hardware and software, because this information is freely available and easily accessible, with the option of adjusting features when needed. The collaboration between experimental scientists, engineers, computer programmers, and data scientists should be encouraged because open-source concepts require multi-disciplinary expertise [54].

2.4. Low-budget components for use in flow chemistry

2.4.1 Open-source syringe pumps

The development of commercial laboratory equipment is in stark contrast to that of the free and open-source equipment since the former follows a secretive and protected by law approach, while the latter is fundamentally new, decentralized, participatory and transparent with regards to the creation of both hardware and software [55]. A major advantage of open-source laboratory equipment is significant cost reduction [56]. As a consequence, high-quality scientific equipment can be placed in the hands of experimental scientists ranging from the most prestigious to the most humble laboratories [55,56].

An important example of open-source laboratory equipment is the syringe pump. In 2014, Wijnen et al. [55] introduced a low-cost open-source family of syringe pumps. Their syringe pump family consisted of three syringe pump designs: two single acting syringe pumps designed specifically for two different stepper motors and a dual version. All three designs included fully customizable 3D-printed mechanical components that were designed with OpenSCAD software and made with PLA using FDM. They also used easily sourced and inexpensive hardware to complete their design. The authors developed their own open-source Python script that controls the syringe pumps. Furthermore, their syringe pumps were demonstrated to perform similarly in comparison to costly commercial versions.

Since 2014, a variety of open-source syringe pumps (some with unique features) were published in literature (Table 2.1). Akash et al. [57] developed an open-source single acting syringe pump without using any 3D-printed mechanical parts, while others [12,49,55,56,58–62] used FDM methods to 3D-print a variety of mechanical components. Some unique features of these single acting syringe pumps included: Feed-back controlled pressure regulation [59], universal serial bus (USB) port or battery operability [60], extrusion-based capabilities [56], touch screen operability and microscopic systems [62].

Table 2.1: *Summary of various open-source syringe pump types for use in flow chemistry. The open-source syringe pumps are listed according to year of publication. The estimated costs (as reported by the authors) are indicated in USD.*

Publication year	Syringe pump type	3D-Printing method	Cost (USD)	Reference
2014	Syringe pump	FDM	<100	[55]
2015	Syringe pump	None	NR	[57]
2016	Dual syringe pump	FDM	≤100	[58]
2017	Syringe pressure pump	FDM	110	[59]
2018	Syringe pump	FDM	230	[60]
2018	Dual syringe pump	FDM	350-603	[12]
2019	Multifunction syringe pump/extruder	FDM	150	[56]
2019	Dual syringe pump	FDM	<100	[61]
2019	Syringe pump array and microscope system	FDM	<400	[62]
2019	Syringe pump	FDM	<360	[49]

NR: not reported.

Garcia et al. [12] developed a programmable dual syringe pump featuring a touchscreen-based graphical user interface (GUI) that is customizable. Their design demonstrated versatile device orientation. In other words, their dual syringe pump could be oriented horizontally or vertically. Recreating their dual syringe pump could cost around USD 350 to USD 603 if optional parts are used.

Regardless of all the unique features, open-source syringe pumps have three common goals. The first goal is to significantly reduce costs [12,49,55,57–59,61,62]. This is usually achieved by using easily sourced and inexpensive hardware such as stepper motors, guide rods, bearings and electronic components. The use of 3D-printed mechanical parts further reduces costs and allows for easy design modifications. The costs involved to reproduce open-source syringe pumps can range from USD 100-600 (Table 2.1), which is considerably less than that of commercial versions (USD 260-5000) [55,57]. Secondly, open-source syringe pumps are designed to be easily reproducible and customizable by others [12,49,58,59,61,62]. Thirdly, open-source syringe pumps have to provide accurate and reliable flow rates that are comparable to their commercial counterparts [12,58,59,61,62] for a wide variety of applications. This is usually demonstrated experimentally. For example, Booeshaghi et al. [62] benchmarked their Poseidon syringe pump system to a commercial array from Harvard apparatus. The authors used a droplet generation chip to generate monodisperse emulsions and obtained comparable droplet diameter sizes for the commercial and open-source syringe pump arrays.

Open-source pumping solutions for fluidic applications are not limited to syringe pumps (single acting or dual). Neumaier et al. [53] developed a continuous syringe pump that works similar to a dual piston pump using 3D-printing technology. The pump can be operated using flow rates between 1.0 µL/min and 3000 µL/min, however pulsation and the skipping of steps (by the stepper motor) at lower and faster flow rates, respectively, are of concern. 3D-printed centrifugal pumps [63], peristaltic [64,65] and venturi pumps [65] have also been demonstrated.

All abovementioned open-source pumps have the potential to be used as cost-effective alternatives to commercial versions in research laboratories for use in flow chemistry. These pumps can be reproduced as reported, or adjustments can be made when required. These pumps are only the first step in the development of a low-cost flow system. Open-source hardware has been used to lower costs of other flow components as well.

2.4.2. 3D-printed flow reactionware fabricated using FDM

2.4.2.1. 3D-printed chip reactors, mixers, back-pressure regulators, and membrane separators

In 2012, Kitson et al. [66] were the first to report on 3D-printed reactors made with PP. The freely distributed design package, Autodesk 123D®, was used to design three reactors: Two of which were basic chip reactors with two and three inlets and volumes of 60 μL and 270 μL respectively. The third reactor design was more unconventional, because it incorporated two pre-filled reactant silos. This was achieved by filling the reactant silos during the fabrication process. All reactors were 3D-printed with a 3dTouch™ 3D-printer with PP as printing material. The 3D-printer used in this work had a printing tolerance of ± 0.2 mm and a layer height of 0.125 mm, however no additional print settings were reported. The channels of all devices were tubular in shape with 0.8 mm diameters. Commercial epoxy adhesive was used to connect the tubing to the access ports of the devices. Each reactor was 3D-printed in less than four hours and the cost of the materials was less than USD 0.35 each. To demonstrate the functionality of their 3D-printed flow reactors, an imine formation, an alkylation reaction, and inorganic self-assembly reactions were carried out, which included in-line analysis with either ultraviolet-visible (UV-Vis) or infrared (IR) spectroscopy.

With the initial success of the above 3D-printed chip reactor, Mathieson et al. [67] linked a PP three-inlet-one-outlet chip reactor (Figure 2.8) to a high-resolution electrospray ionisation mass spectrometer (ESI-MS) for real-time, in-line analysis of supramolecular chemical reactions. The design described above was improved by adding access ports that were compatible with commercial fittings to allow for enhanced connections, seals, and reusability of devices. The device was designed and fabricated similarly as above, with 1.5 mm channel diameters and a total volume of ca. 0.65 mL. In order to connect the outlet of the chip reactor to the ESI-MS, a T-piece and a PEEK microsplitter valve device was used for dilution and splitting of the product stream, respectively. It was also possible to oscillate between the synthesis of two salt complexes simultaneously by only employing two of the three reagent streams at a time.

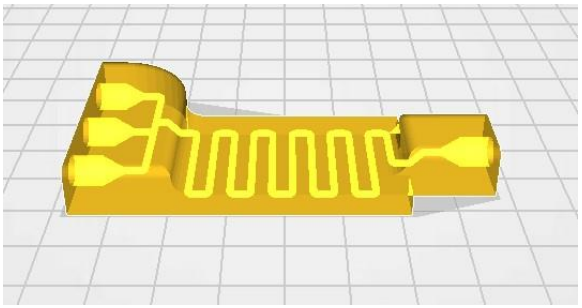

Figure 2.8: *The three inlet and single outlet chip reactor designed by Mathieson et al. [67]. The chip reactor was made freely available and is shown here as viewed with a slicing program.*

A few weeks after the publication of the above article, Dragone et al. [50] went on to report on yet another set of 3D-printed PP chip reactors. These reactors were designed and fabricated in-house similarly as described above and both had two inlets, a mixing point followed by serpentine-like channels (1.5 mm diameter) and an outlet with volumes 0.4 mL (R1) and 0.35 mL (R2). Reactor R1 was used for the synthesis of various imines, and two R2 reactors were placed in series to perform imine reduction reactions. Both applications were connected to an attenuated total reflectance infrared (ATR-IR) flow cell for in-line analysis [45].

Without a doubt, authors from the Cronin group could be considered the pioneers of the 3D-printing and flow chemistry community and shortly after the publication of the above articles many researchers followed suit. The group also published several other articles using 3D-printing to fabricate laboratory reactionware, however these articles are not necessarily related to flow chemistry [68,69].

Capel et al. [70] considered five additive manufacturing techniques for millilitre-scale reactor fabrication: stereolithography (SLA), multi-jet modelling (MJM), selective laser melting (SLM), selective laser sintering (SLS), and FDM. Leak-free devices were tested for the oxidation of an aldehyde to a methyl ester. The group started with a complex design of a split and recombine static mixer that consisted of a tube of length 510 mm, diameter 3 mm, and a total volume of 3.6 mL. An advanced FDM machine (Stratasys Dimension 3D-modelling printer) was required to 3D-print the reactor with ABS filament and with a soluble support

structure. Post-manufacture machining was used to add standard screw threads to the inlet and outlet of the device for connections to a FlowSyn continuous flow system. Unfortunately, the device was leaking when tested with water at a flow rate of 1 mL/min and a pressure of 20 bar. In an iteration, the authors successfully 3D-printed similar reactors using SLA and commercially available resin with internal volumes and diameters ranging from 16.4 mL to 23 mL and 0.25 mm and 3 mm, respectively.

Similarly, Rao et al. [51] developed a custom-made PP continuous flow column reactor that can be directly fitted into a commercial Uniqsis FlowSyn continuous flow reactor system. The 3D-printed column reactor was designed to fit directly into the space of the existing column reactor segment which could be heated automatically by the system. The column reactor was designed using open-source Tinkercad® (Autodesk) software and houses a single spiral shaped channel. The reactor was 3D-printed using Cura software and an Ultimaker 2 3D-printer. A leak-free reactor was obtained using a 100% infill and a material flow of 110%. The reactors were tapped out to provide screw threads compatible with commercial PEEK fittings. The spiral channel had a diameter of 2 mm, with a calculated internal volume of 1.6 mL and each reactor costs less than USD 0.50. The PP reactor was able to withstand harsh conditions, i.e., polar solvents and temperatures up to 150 °C. Optimized reaction conditions (150 °C, 5-minute residence time) allowed the authors to obtain a single diastereomer in good yield.

In general, flow reactors for small scale experiments can be classified as either microreactors (ID<1 mm) or as mesoreactors (ID>1 mm) [71]. Rossie et al. [72] demonstrated the use of flow reactors made from materials other than PP, including PLA, nylon and HIPS. A wide variety of mesoreactors was used for the flow synthesis of biologically active chiral 1,2-amino alcohols, such as norephedrine, metaraminol, and methoxamine. The reactors were constructed using the freely distributed software packages Autodesk 123D® and Netfabb basic 5.2 (Autodesk) and a Sharebot NG 3D-printer. The mesoreactors consisted of either two, three or four access ports with channels being circular, square, or rectangular in shape, and some even included zig-zag channels. The volumes of the reactors varied from 0.75 μL to 10 mL. PLA was the preferred fabrication material because it was less sensitive to decomposition caused by exposure to organic solvents compared to the other fabrication materials. Therefore, PLA reactors were employed for the copper-catalyzed enantioselective Henry reactions at −20 °C

and a residence time of 30 minutes. This methodology gave higher yields and enantioselectivity compared to their counterpart PTFE tube reactors. The authors successfully demonstrated the scalability of the reaction by employing a 10 mL reactor. Tabassum et al. also developed 3D-printed PP mesoreactors for educational purposes [71].

A variety of low-budget flow components were developed by Neumaier et al. [49]. They designed and fabricated various customizable flow reactor cells for multi-step glycosylation reactions. An inexpensive FDM 3D-printer (Anet 8) was custom-modified in order to improve printing quality and to allow for stable, safe and convenient operation. All devices were designed using Autodesk Inventor Professional 2018 and the G-codes were obtained using open-source software from Ultimaker (Cura 2.7.0). An early-stage prototype chip reactor was designed with tubular channels (1.5 mm inner diameter) that was spaced relatively far apart and 3D-printed with PP. Unfortunately, the chip reactor was not leak-proof due to the circular channel profile, and therefore the authors opted for square channel profiles.

Additionally, the channel path lengths were elongated by decreasing the distance between channels. Leak-free reactors were obtained using a filament flow ranging between 105-110%, printing the spaces between channels with continuous lines, and a wall thickness of 1.2 mm. As a result, a larger, leak-free, PP chip reactor was obtained with square shaped channels (1.2 mm length and width) and a total volume of 1.05 mL. This chip reactor had two initial inlets with a subsequent chaotic mixing zone, which consisted of a zig-zag shaped channel, followed by a quenching zone positioned near the outlet of the device (Figure 2.9C). Sufficient mixing was observed using two dyes in dichloromethane. An additional leak-proof chip reactor with a total volume of 1.5 mL was also designed and fabricated similarly as the others, however this reactor had to be mounted on a 3D-printed PLA L-shaped rail for connection purposes. Reliable connections from the reactors to the tubing was achieved by in-printing screw-nuts directly into the reactors or the L-shaped rail by pausing the 3D-printer and inserting the screw-nuts before continuing printing. It is important to mention that the chip reactors were designed in such a way that channels could be easily added or removed by any CAD program, which allows for versatile devices with a wide range of purposes in flow chemistry.

Impressively, the authors 3D-printed a 12 µL PP chip reactor with 200 µm square channels [49], which is the smallest FDM-printed PP microreactor to date in literature [31]. PP chip reactors with smaller channel dimensions were prone to blockages due to polymer spreading during extrusion-based printing and were thus deemed unfeasible. In addition to the chip reactors, two and three access port CSTRs were constructed similarly as the other reactors (Figure 2.9A to 2.9B). The channel diameters of the CSTRs were 2 mm, and the diameters of the tanks were 15 mm and 11 mm for the two and three access port CSTRs, respectively. The 3D-printed CSTRs were paused during printing to insert small magnetic stirring bars for active mixing purposes. Screw-nuts were imprinted in the access ports as well. These reactors were either used for premixing of reactants or extraction steps to ensure sufficient mixing between the aqueous and organic phases.

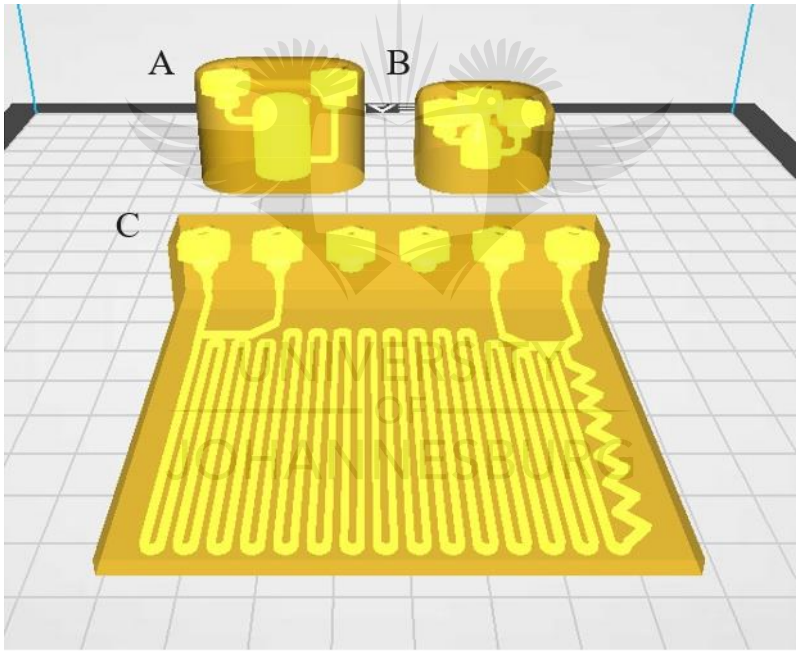

Figure 2.9: *(A) Two access port CSTR. (B) Three access port CSTR. (C) The flow reactor with four access ports (two inlets, a single outlet, and a quenching port). The chip reactor has a chaotic mixing zone (zig-zag channel) followed by standard serpentine-like channels. The STL files were downloaded as provided by the authors [49]. The CAD designs were viewed in a slicing program in transparent mode to view the spaces for the screw nuts, reaction zones and channels of the flow reactors.*

With their low-budget 3D-printed reactionware in hand, the authors performed glycosylation and azidation reactions to demonstrate the utility of their flow system [49]. Using their 3D-printed syringe pumps (see Section 2.4.1), a solution of pentaacetylglucose in dichloromethane (1 M) was mixed with a 33% hydrogen bromide in acetic acid solution in a 1.5 mL PP chip reactor at ambient temperature with a 7.5 min residence time. In-line reaction work-up and product isolation was achieved by using a 3D-printed CSTR and a phase separation system (using 10 mL syringes fitted with a CSTRs) to afford acetobromo glucose in 86% yield. Notably, the PP chip reactor withstood harsh acidic conditions and the authors successfully developed an easily scalable flow-mode protocol for the preparation of acetobromo glycoses.

Additionally, Koenigs-Knorr reaction conditions were used in the preparation of simple glycosides with the activator, silver triflate [49]. A solution of acetobromo glucose in dichloromethane (0.25 M) was mixed in a three access port CSTR with methanol (20 mol equivalents) by using two 3D-printed syringe pumps simultaneously. The mixture was then treated with silver triflate packed in a commercial packed bed reactor to afford methyl glycoside in a 44% yield and a 5-minute residence time.

A two-step glycosylation process was also demonstrated with two chip reactors placed in series [49]. Solutions of pyranose, trichloroacetonitrile (10 equivalents), and 1,8-diazabicyclo(5.4.0)undec-7-ene (0.2 equivalents) were pumped with the 3D-printed syringe pumps into the first chip reactor (1.05 mL) at room temperature and a residence time of 3.5 minutes to afford the glycosyl donor (trichloroacatimidate) *in situ*. The reaction mixture was then treated with various alcohols (methanol, propargyl alcohol and 4-pentylnol) and trimethylsilyl trifluoromethanesulfonate in a second chip reactor (1.05 mL) cooled to 0 °C to produce various glycosides with respectable yields. The residence times for the second chip reactor ranged between 3.5-4.2 minutes depending on the alcohol used.

Lastly, a potentially hazardous reaction for the preparation of glycosyl azides was demonstrated [49]. Pentaacetyl glucose was treated with trimethylsilyl azide in the presence of stannic chloride in a chip reactor (1.05 mL) to afford 2,3,4,6-tetra-*O*-acetyl-β-D-glucopyranosyl azide in 80% yield and a 7-minute residence time.

Remarkably, the authors demonstrated that their low-cost 3D-printed reactionware (pumps, CSTRs, chip reactors) for flow chemistry purposes were able to withstand harsh acidic conditions and were able to safely carry out hazardous chemical reactions. Multi-step reactions and in-line work-up was also successfully demonstrated [49].

Although BPRs are commercially available, these devices can cost up to USD 1000 [31] which is too expensive for low-budget research laboratories. A cost-effective alternative would be a self-manufactured version. A 3D-printed PP BPR was demonstrated by Walmsley and Sellier [73]. The BPR consists of a liquid (Figure 2.10A) and a gas face plate (Figure 2.10B) that was designed using the open-source software, Tinkercad®. Open-source Ultimaker Cura software and an Ultimaker 3 3D-printer was used for the fabrication of the two face plates using PP filament. A PTFE membrane diaphragm (0.1 mm thickness) was placed between the two face plates that facilitates liquid and gas separation. The authors chose PP for its moderate chemical resistivity, however by design and because of the protective layer provided by the PTFE membrane, minimal solvent contact onto the liquid face plate was reported. M4 stainless steel wing nuts were used to secure the two face plates in place and a PTFE gasket, a silicone O-ring, a straight pneumatic push fit 4 mm OD male M5 adapter completes the BPR assembly. All commercial hardware can be easily sourced and costs approximately USD 109. The BPR was tested for leaks using tetrahydrofuran and acetonitrile using flow rates up to 3 mL/min and gas pressures of up to 2 bar, however no upper limit for either parameter was established.

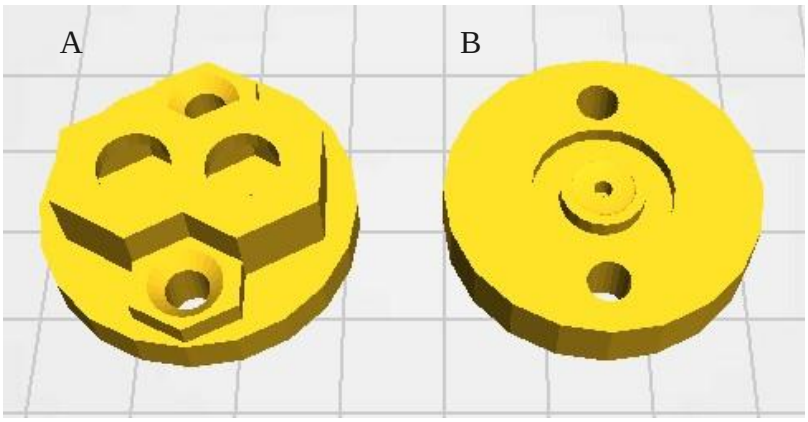

Figure 2.10: *Model of a 3D-printable back pressure regulator. The STL files were downloaded as provided by the authors [73]. The liquid face plate (A) and the gas face plate (B) were viewed in a slicing program.*

Recently, 3D-printed chip reactors using FDM were made in PEEK as printing material. Harding *et al.* [74] developed a PEEK chip reactor using an advanced and expensive FDM 3D-printer with a 0.4 mm nozzle diameter. The chip reactor was designed using Autodesk Fusion 360, and consists of three threaded access ports (two inlets and a single outlet) with serpentine channels (4 mm diameter) with eight internal helical obstacles (Kenics design) to improve mixing capabilities and lower pressure drops. The device had a total volume of 1 mL and material cost related to the reactor was less than that of an injection moulded PEEK tubing union. Additionally, the authors developed similar chip reactors with volumes less than 1 mL by decreasing channel diameters and increasing mixing elements. Post-printing annealing formed part of the fabrication process where the reactors were placed in a furnace set at 150 °C for one hour, followed by an increase to 250 °C for two hours and a subsequent decrease to 150 °C for 30 minutes. Characteristically, the PEEK device withstood elevated temperatures and high pressures (≥30 bar) leading to reactions taking place above solvent boiling points. The performance of the 3D-printed PEEK reactor was demonstrated using the S_NAr reaction of 2,4-difluoronitrobenzene with morpholine, and methanol as the solvent. A second identical PEEK reactor was placed in series for liquid-liquid extraction with water and ethyl acetate. Under optimized reaction conditions, a 97% conversion of the starting materials was achieved with a 5-minute residence time at a temperature of 80 °C.

Adding to their successful low-budget 3D-printed flow system [49], Neumaier et al. [53] went on to develop PP and PEEK flow reactors with various mixing geometries placed inside reactor channels and essential flow equipment such as a BPR and a membrane separator made from PEEK. The group added an additional 3D-printed continuous syringe pump (see Section 2.4.1) to their vast 3D-printed flow chemistry reactionware collection. The authors used their customised Anet A8 3D-printer for their PP reactors and an advanced Apium P220 3D-printer for the devices made from PEEK. All flow components were designed using Autodesk Inventor Professional 2016, and the STL files were sliced using either Cura 3.7 or Simplify 3D to obtain the G-codes for the 3D-printers. Reminiscent of their previous tubing-to-reactor-connection methodology, the authors used 3D-printed PEEK rails, where reactors can be slotted into and secured with standard flangeless flat bottom 1/4”-28 fittings. Reactors made from PP, had openings on the sides of the devices where stainless steel nuts were inserted to facilitate tubing connections.

The 3D-printed back-pressure regulator was designed in such a way that the pressure was controlled by spring force. The solvent conducting part (bottom part, Figure 2.11A) was the only part 3D-printed with PEEK, and the remaining parts (top part, spring holder, stamp, screw, Figure 2.11B to 2.11E) was 3D-pinted with PLA, because these parts were not in contact with any solvents. A 0.5 × 6.5 × 25 mm spring could be used to facilitate a backpressure ranging from 1-4 bar, and a 0.8 × 7.7 × 25 mm spring up to 20 bar. PTFE foil (100 µm) and a silicone sheet (500 µm) complete the hardware required to round off the design.

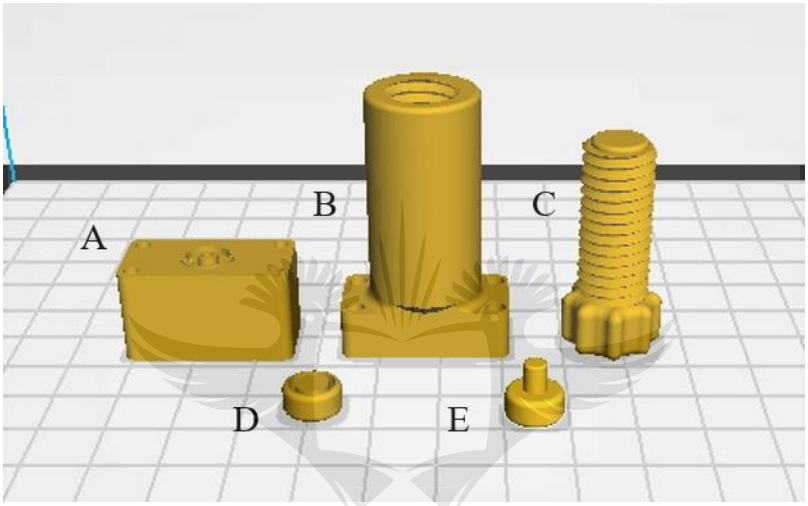

Figure 2.11: *Model of another 3D-printable back pressure regulator. The STL files were downloaded as provided by the authors [53]. (A) Bottom part. (B) Top part. (C) Screw. (D) Stamp. (E) Spring holder.*

A 3D-printed PEEK membrane separator for the separation of two immiscible liquid phases (organic and aqueous phase) was developed [53] and consists of only two 3D-printed PEEK parts (Figure 2.12A to 2.12B) and requires a PTFE membrane (1 µm pore size, 100 µm thickness). Channels of 35 × 8 × 1 mm were used for both 3D-printed parts which includes diagonal support lines to prevent bending of the membrane. The BPR and the membrane separator could be fabricated out of PP, however both designs required additional support by custom aluminium plates on top of the screw fittings to evenly distribute contact pressure. The functionality of the 3D-printed flow system components was demonstrated by the multi-step synthesis of glycosyl bromide. Optimized reaction conditions resulted in a 99% conversion of the starting material.

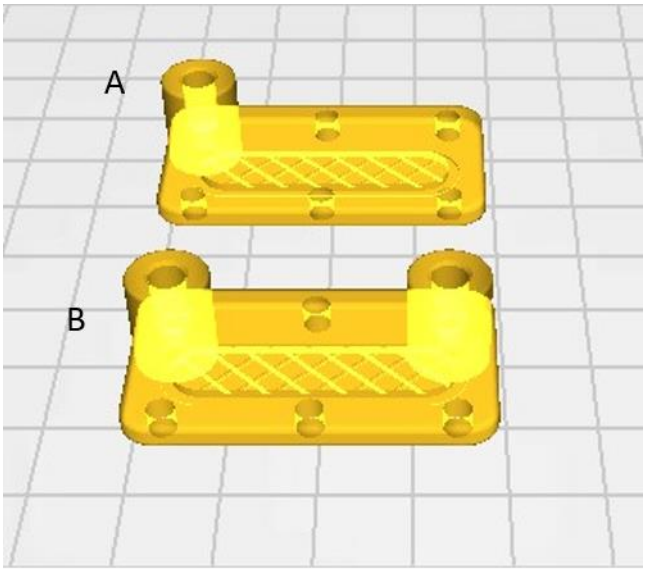

Figure 2.12: *Model of a 3D-printable membrane separator. The STL files were made freely available by the authors [53]. The membrane separator part 1 (A) and part 2 (B) was viewed transparently to see the channel profile and diagonal support structure.*

2.4.2.2. 3D-printed packed bed reactors

3D-printed flow reactors are not limited to liquid-liquid reactions. In fact, solid-liquid reactions in flow using 3D-printed reactionware have also been demonstrated. Alimi et al. [75] designed and manufactured a 3D-printed packed column reactor. The reactor was 20 mm in length and had an outer radius of 4 mm. Since the use of commercial fittings were avoided (i.e., nuts and ferrules), the inlet and the outlet were designed to have a radius of 0.97 mm each, which coincides with that of the tubing used (1/16”). The radius of the column, where the catalyst resides, was 2.2 mm. The reactor was reported to have a volume of 0.23 mL (Figure 2.13B). The flow system included a T-mixer (Figure 2.13A), where the dimensions of the access ports were similar to that of the column reactor. Both components were made from PLA. The packed column reactor was packed with Pd/Co_3O_4 during the 3D-printing process with glass wool placed at the ends of the bed to secure the catalyst in its desired location and to prevent leaching. The flow system was used for the reduction of 4-nitrophenol to 4-aminophenol. Reaction parameters (temperature, flow rate, catalyst amount) were optimized, and a 98% conversion was obtained using a temperature of 30 °C, a flow rate of 0.5 mL/min, and 20 mg Pd/Co_3O_4.

With the initial success of the abovementioned work, Alimi et al. [76] 3D-printed another column reactor using PLA filament. However, in this instance the design was more sophisticated and incorporated access ports that were compatible with commercial HPLC fittings. The reactor had a volume of 0.4 mL. The column reactor was packed with immobilised palladium nanocatalyst (Pd/Co_3O_4) for morin oxidation. Morin oxide was obtained with a 98% conversion at a residence time of 8 minutes. The packed bed reactor was submerged into a thermostatic oil bath at 40 °C.

A 3D-printed sacrificial template was used to produce an alumina monolith followed by the immobilisation of palladium nanoparticles using the deposition-precipitation method by Alimi et al. [77]. The monolith catalyst was then placed into a 3D-printed PP column reactor (Figure 2.13C) for the epoxidation of styrene with tert-butyl hydroperoxide in flow-mode, resulting in 55% styrene conversion and a 74% selectivity towards styrene oxide. The flow rate was 0.11 mL/min (50-minute residence time), and the reactor was placed in a thermostatic oil bath at 80 °C. All reactors by Alimi et al. [75-77] were designed using open-source software, OpenSCAD, and all reactors were 3D-printed using a Prusa i3 MK3S 3D-printer.

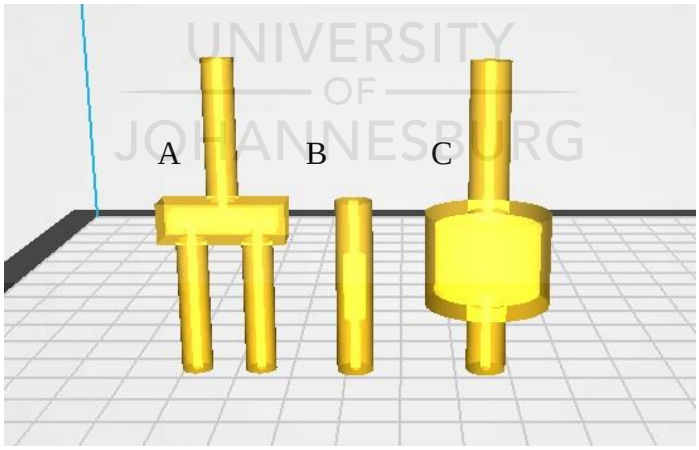

Figure 2.13: *Models of a mixer and packed bed reactors. The STL files were downloaded as part of the supplementary material provided by the authors [75,77]. The reactor designs were viewed in slicing software with the voids clearly visible. (A) Mixer. (B) The packed column reactor for the reduction of 4-nitrophenol [75]. (C) Packed column reactor used for epoxidation of styrene [77].*

A 3D-printed U-shaped packed bed reactor was developed by Onisuru et al. [78]. The 3D model of the reactor was designed using Tinkercad® and fabricated using PrusaSlic3r and a Prusa i3 MK3S 3D-printer. PLA was the fabrication material of choice because it is inexpensive, biodegradable and was chemically inert under the chosen reaction conditions. Mesoporous manganese oxide and mesoporous cobalt oxide was used as heterogeneous catalysts. Hexacyanoferrate (III) was reduced to hexacyanoferrate (II) using sodium borohydride. Reaction conditions were optimized and a 94.1% conversion of Fe^{III} to Fe^{II} in 6 minutes was obtained using a flow rate of 0.5 mL/min and a temperature of 55 °C. The U-shaped reactor was reported to have superior mixing capabilities compared to the column design and handling of the reactor was improved because it fits securely in a 100 mL beaker for the submerging of the reactor in a thermostatic bath.

2.4.2.3. 3D-printed fittings

Most of the 3D-printed fluidic devices discussed so far, rely on techniques such as tapped access ports or in-printing nuts to make them compatible with commercial fittings. In other cases, connections were established by using epoxy resins in order to secure tubing to fluidic devices.

In 2015, Bishop et al. [79] demonstrated that 3D-printed fittings (i.e., nuts) can be incorporated into 3D-printed fluidic devices using FDM. They modified open-source threaded nuts and screw design files to create threaded ports for fluidic devices and threaded fittings. Two types of nuts were designed, one for standard tubing connections and one that housed electrodes. The fluidic devices and the nuts were 3D-printed using PET and ABS as printing material, respectively. The functionality of their flow system was demonstrated by preparing Prussian blue nanoparticles. Furthermore, 3D-printed fittings were also demonstrated by Vijayan et al. [80]. However, their fittings were limited to a Y-mixer and a needle holder. In addition, they used SLA to 3D-print their fittings. Axisymmetric configurations of the 3D-printed fittings together with commercial components were used to generate complex emulsions. Droplet fluidics is a subfield of flow chemistry that is outside the scope of this work, however more examples of 3D-printed droplet generators can be found in the literature [81–84].

Recently, Price et al. [34] developed an open-source 3D-printable collection of common fittings and connectors required to connect flow systems. The toolkit consists of threaded nuts, Luer adapters, and a variety of junction connectors (Figure 2.14). Components were designed and modelled using Siemens NX software and FDM was used to 3D-print the components. The toolkit has both wetted and non-wetted components. The wetted components come into contact with common laboratory solvents and therefore has to be structurally strong and chemically inert. These parts were fabricated using multi-material 3D-printing to combine multiple polymer properties into the wetted components. In general, PLA was used as printing material for the shells and PP for the cores. The authors included a PP chip reactor with a threaded inlet and an outlet that is connected by continuous serpentine channels.

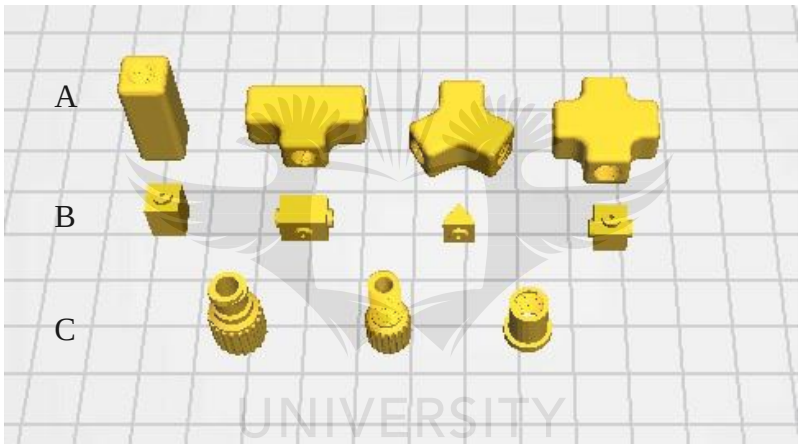

Figure 2.14: *Models of 3D-printable fittings. The STL files of the open-source toolkit was downloaded (as provided by Price et al. [34]) and viewed in a slicing program. (A) Shells of the straight union connector, T-connector, Y-connector, and the cross connector (from left to right). (B) The cores of each connector placed in front of its corresponding shell. (C) The Luer adapter shell, threaded nut, and Luer adapter core (from left to right).*

2.4.2.4. 3D-printed modular flow systems

Penny et al. [85] identified the need for a complete 3D-printed flow system that does not take up a lot of benchtop or fume hood space and is independent of commercial pumping solutions such as syringe pumps. The authors published two articles using their 3D-printed flow system: The first article served as an introduction of their bespoke flow system to the 3D-printing and

flow chemistry community [85], and the other demonstrated the use of their flow system to demonstrate educational concepts such as laminar flow, dispersion, residence time, and multi-step synthetic protocols in continuous flow [16].

The individual flow components were all designed using the web-based freeware Tinkercad® (Autodesk) software and 3D-printed using an Ultimaker 3 3D-printer. The stackable components were designed to fit onto the support rod of a commercial stirrer hotplate, and consist of a base unit, flow unit, injection unit, and a bottle holder unit that are stacked on top of each other in that order. These units were 3D-printed using PLA with a 10% infill and a layer height of 0.2 mm. The assembled system stands 341 mm tall without the addition of the solvent bottle.

The authors designed and fabricated two flow reactors namely a mixing chip and a circular disk reactor (CDR). These reactors were 3D-printed using PP filament and a 100% infill. The CDRs and the mixing chips were designed to incorporate screw thread adapters for the addition of commercial PEEK fittings. The CDR was designed to have a height of 7 mm, a 2 mm high reactor channel and a diameter of 75 mm that fits in the spaces of a DrySyn block. These reactors had a volume of 4.2 mL. All 3D-printed components cost less than USD 65, and it takes approximately 84 hours to complete the 3D-printing process.

The flow system requires Duran bottles pressurised to 1.5 bar in order to use compressed air as the driving force for the system, and the stirring hotplate functions as the heat source. Capillary resistors were placed downstream of the reactors to control the flow rate and act as back-pressure regulators. This feature enables reactions to be carried out near or above solvent boiling point. The utility of the system was tested using S_NAr reactions between 5-nitro-2-chloropyridine and 4-methoxyphenol in the presence of a 1,8-diazabicyclo(5.4.0)undec-7-ene and acetonitrile solution. A 95% conversion of the addition product (2-(4-methoxyphenoxy)-5-nitropyridine) was obtained using a temperature of 65 °C, two CDRs and a pressure of 5 PSI (0.34 bar). The S_NAr reactions were later expanded to include a variety of phenols.

In the authors' follow up educational article [16], they focussed on concepts related to passive and active mixing. They designed and 3D-printed a variety of mixing devices using Tinkercad® and an Ultimaker 3 3D-printer. All mixing devices were 3D-printed using transparent PP filament. Their passive mixing device showed relatively low mixing efficiency when mixing *p*-cresol and 2-chlorophenol. However, their active mixing devices containing a cylindrical or cross-shape magnetic stirrer bar both showed efficient mixing of the alcohols. The cross-shape stirrer bar was preferred because the cylindrical shape tended to "catch" at higher speeds. It was also demonstrated that the flow system was able to run multiple reactions in parallel by splitting the flow streams exiting the active mixing chip between two capillary resistors on the same stirrer hotplate. The mixing profiles were compared after splitting two reactor paths using a single or multiple CDRs with varying reactor volumes.

So far, a large collection of 3D-printed flow system components has been discussed as cost-effective alternatives to commercial flow systems. Furthermore, these components are mostly open-source and can be utilized in research laboratories, especially in developing countries, to self-manufacture a low-budget flow system for research purposes.

2.5. Transesterification of edible oils: Sample preparation for chromatographic analysis

2.5.1. Sample preparation

Sample preparation is a critical step for the transformation of samples to make them amenable for analysis [86,87]. In chromatographic analysis, sample preparation can be considered as the main source of errors. In addition, sample preparation can be costly since it can be labour intensive and heavy on chemicals and laboratory consumables [86]. A rudimental flow diagram displaying the position of the sample preparation step using chromatography as the main analytical technique is given in Figure 2.15. Sample preparation can be considered as the protocols carried out after sample collection and before chromatographic analysis (Figure 2.15). Well-known examples of sample preparation processes are filtration, distillation, precipitation, dilution, solvent extraction, and analyte derivatization [86,87].

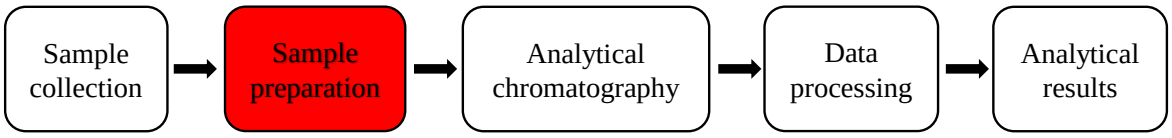

Figure 2.15: *Simplified diagram of the critical steps for a typical chromatographic method of analysis highlighting the position of sample preparation (adapted from S.C. Moldeveanu [86]).*

Samples are primarily derivatized prior to gas chromatographic (GC) analysis in order to improve separation, peak shape, and analyte response [88]. Derivatization methods are widely utilized for the quantitative GC analysis of edible oils. Edible oils consist primarily of triacylglycerol (TAG) molecules which can be described as a molecule consisting of a glycerol molecule connected to three medium or long chained fatty acid residues [89]. TAGs are not volatile enough for direct GC analysis [90], and therefore have to be converted into fatty acid alkyl esters (usually methyl esters) [91]. Fatty acid methyl esters (FAMEs) are sufficiently volatile with reduced polarity which is more suitable for GC analysis [90,92]. In general, TAG molecules react with a short chain alcohol (usually methanol) in the presence of a strong acid or a strong base (acting as a catalyst) to produce a mixture of FAMEs and glycerol (Figure 2.16). This transformation is commonly referred to as transesterification. The stoichiometric ratio of TAG to alcohol is 1:3 (Figure 2.16), however experimentally the alcohol is present in excess to increase the FAME yield and to allow phase separation [93].

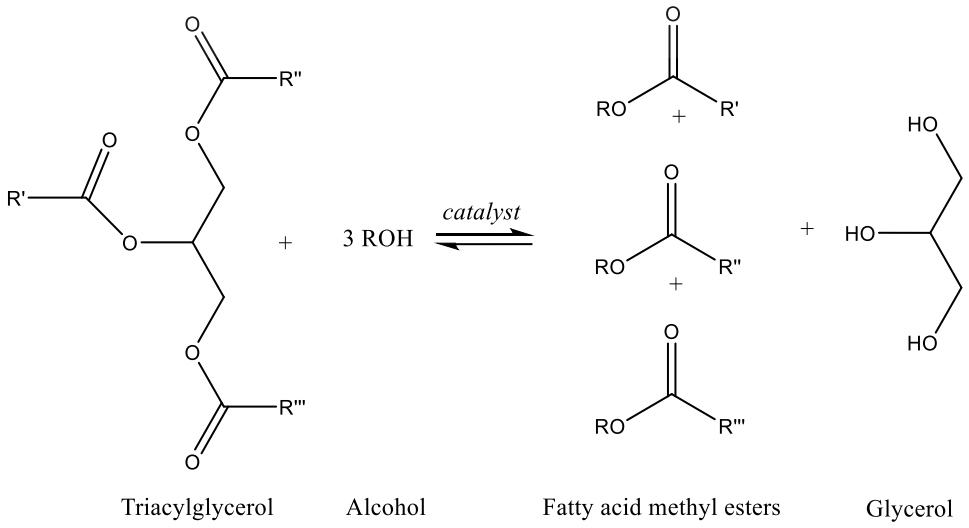

Figure 2.16: *Transesterification of edible oils (adapted from Schuchardt et al. [93])*

Transesterification reagents typically used for the derivatization of TAGs can be divided into three main groups: Acid-catalyzed alkylation reagents (e.g., boron trifluoride in methanol, sulfuric acid in methanol, and methanolic hydrochloric acid), base-catalyzed alkylation reagents (e.g., potassium hydroxide, sodium hydroxide, or sodium methoxide, all in methanol), and quaternary salts of ammonia (trimethylphenylammonium hydroxide (TMPAH) and tetramethylammonium hydroxide (TMAH)) [91,94].

Base-catalyzed alkylation reagents are preferred over acidic catalysts because transesterification reactions of neutral lipids occur faster [91]. Sodium methoxide in methanol is a well-known example of a base-catalyst with fast reaction rates at ambient temperature for the conversion of TAGs to FAMEs [94]. When mild reaction conditions are employed, the reagent does not cause any isomerization of the double bonds. However, this catalyst is unable to convert free fatty acids (FFAs) to FAMEs. Fatty acid compositions can be altered when this catalyst is used under careless and prolonged conditions. Additionally, harsh reaction conditions (high temperatures and high catalyst concentrations) can result in the formation of conjugated fatty acids [94]. It was previously reported that the reaction conditions need to be anhydrous, since the presence of water results in saponification, which consequently leads to loss of fatty acids [91,94]. However, Suter et al. [95] demonstrated that the complete absence of water was not a prerequisite for the transesterification of water-containing food products using a base-catalyst. The authors used sodium methoxide (5 wt.%) as the chosen base-catalyst, and the reaction takes about one-minute at ambient temperature.

Although batch protocols have been widely demonstrated [96] and compared [90], efforts have been made to automate the derivatization reactions of TAGs [97] and FFAs [98] to obtain the corresponding FAMEs. The automation of derivatization reactions in general has advantages such as reduced sample handling, improved throughput and reproducibility which ultimately lead to a decrease in overall costs [86,88,97], however full automation can be complicated [86]. Examples of automated commercial equipment are XYZ handlers, workstations, and online instrumentation [86]. De Koning et al. [97] demonstrated an automated method using a XYZ handler for the determination of FAMEs and *cis/trans* methyl ester composition of fats and oils. The authors chose to automate the sodium methoxide method, since it does not require heating to boiling point or the use of large amounts of reagents and solvents as is the case for

other catalysts, such as boron trifluoride. All operations were fully automated (reagent addition, agitation, sample settling, and final injection into the GC), except for sample weighing and the addition of heptane. Their automated procedure was compared to the batch mode boron trifluoride method and similar experimental results were obtained. However, the automated procedure was four times faster than the batch protocol, thus demonstrating the advantages of automation. A fully automated version was demonstrated by Schilling et al. [99]. The authors used the same base-catalyst, however the system consisted of a workstation interfaced with robotic tool change.

Another automated sample preparation method for the derivatization of TAGs and FFA is flow chemistry. A continuous flow system with in-line GC analysis for the preparation of FAMEs in olive oil and other oil types was demonstrated by Ballesteros et al. [100] in 1993. The optimized flow system introduced the diluted oil sample and acetyl chloride in methanol (flow rates 0.28 mL/min each) into a 500 cm reactor coil (0.5 mm ID) that was heated to 80 °C in a water bath. After two minutes, the flow was paused for 15 minutes to allow complete derivatization in the reactor coil. A water stream was then introduced at 1 mL/min into the flow system to separate excess derivatizing reagent (in methanol) and residual products. A phase separator was used to isolate the organic phase from the aqueous phase prior to injection into the GC. Twelve oil samples were analyzed, and the automated flow system was compared to the batch mode protocol using boron trifluoride in methanol. Similar experimental results were obtained with minimal sample handling and a reduction of overall costs since less organic solvents and reagents were consumed.

Duong and Roper [98] developed an automated sample preparation method to derivatize FFAs to its corresponding FAMEs using a glass microfluidic chip. The microfluidic derivatization chip reactor consisted of two intersecting initial inlets interfaced to a serpentine reaction channel (29 µL volume) that was connected to an outlet. The device was fabricated using conventional photolithography and wet etching techniques using hydrofluoric acid. Furthermore, additional complicated and time consuming fabrication steps were required to complete the device such as baking for 30 min at 105 °C, channel etching, drilling of access ports, and thermal bonding. Briefly, a six-port HPLC system was used to introduce a plug of FFAs into the chip reactor where it was mixed with methanolic hydrochloric acid. The reaction

mixture flowed through the heated reaction zone (55 °C) and the FAME products exited the outlet where it was collected into a vial (manually). The FAMEs were extracted with heptane and analyzed using gas chromatography-mass spectrometry (GC-MS). The authors compared their flow system to the typical sample preparation procedure (i.e., the batch protocol) provided by the manufacturers of their purchased methanolic hydrochloric acid. Their derivatization method resulted in a 20-fold and 1300-fold decrease in the required amount of methanolic hydrochloric acid and FFAs, respectively. Furthermore, the entire sample preparation process was reported to take approximately five minutes.

2.5.2. Gas chromatography-flame ionization detection (GC-FID): Basic principles and instrumentation

In principle, analytes contained in a vaporized sample are separated by being partitioned between the gaseous and chemically inert mobile-phase and a liquid stationary phase contained in a column. In essence, the samples are vaporized followed by injection into the chromatographic column head where analyte elution is brought about by the flow of the mobile phase [101].

The basic components of a typical gas chromatograph can be divided into four major components: the carrier gas source, sample injection system, column, and the detector [102]. The carrier gas source in GC is often a pressurized gas cylinder containing the mobile-phase gas that is required to be chemically inert and responsible for transporting the analyte through the column. Examples of mobile-phase gases are helium, argon, nitrogen, and hydrogen where helium and hydrogen gas are more commonly used. The sample injection system consists of an autosampler and autoinjector fitted with a calibrated microsyringe. The sample can be injected manually, however automating this step increases the reproducibility of the system. The sample injection system injects the liquid sample as a vapor plug through a septum into a heated sample port situated near the column head. The sample port is normally heated approximately 50 °C above the boiling point of the least volatile component in the sample. A sample splitter can be used to inject a known fraction (1:50-1:500) of the sample where the remainder is directed to waste. Splitless injection is also available and can be used to improve sensitivity. Capillary columns vary in length (2-60 m or more) and can be fabricated in stainless

steel, glass, fused silica, or Teflon. Columns are rolled into coils in order to fit inside the thermostated oven where the temperature depends on the sample boiling point and degree of saturation [103].

The flame ionization detector (FID) is a popular detector used in GC. Briefly, effluent exiting the column is guided into a small air-hydrogen flame where most organic compounds are pyrolyzed into ions and electrons. The detector monitors the current produced by the collection of charge carriers. Between the burner tip and the collector electrode is an applied potential difference (a few 100 V) that attracts the ions and electrons towards the electrode. A sensitive picoammeter is used to measure the resulting current (approximately 10^{-12} A) [103].

In practice, excellent chromatographic separations are accomplished by optimizing parameters such as oven temperature (isothermal or ramped programs), carrier gas flow rate and composition, and GC capillary column type [96].

2.5.3. Fatty acid methyl ester (FAME) analysis by GC-FID

Gas chromatography coupled with a flame ionization detector (GC-FID) is widely used to determine the content and compositions of fatty acids in consumable products because of its high accuracy and sensitivity, fast analysis speed, wide linear range, and convenience [92]. A general approach for the analysis of edible oils is to first derivatize TAGs to their corresponding FAMEs followed by the quantification by GC-FID. Internal standards can be added during the sample preparation step in order to calculate the FAME content in terms of mg/g [96].

Fundamentally, gas chromatographic separation of FAMEs are based on chain length, degree of saturation (i.e., number of C-C double bonds), and double bond geometry (i.e., *cis* or *trans* configurations). A wide selection of capillary columns are commercially available and have been reviewed [94,96,104]. FAME separation can be achieved by using non-polar, intermediately polar, or highly polar stationary phases. The polarity of the capillary column influences the retention times of the FAMEs, especially for polyunsaturated fatty acids [104].

In general, when a non-polar stationary phase is used the FAMEs are eluted in order of their boiling points and the unsaturated components are eluted before their saturated counterparts of the same chain length. This elution order is reversed when an intermediate and highly polar stationary phase is used [94].

Highly polar capillary columns with cyanopropyl polysilicone stationary phases (for example SP-2560 and CP-Sil 88) are commonly used for thorough separation of most positional and geometric FAME isomers [96]. These columns have the disadvantage of less thermal stability compared to non-polar phases. However, stationary phases with intermediate polarity have advantages such as relatively high-resolution capability and thermal stability with fast separation of FAMEs [104]. Examples of intermediate polarity stationary phases include those made from polyethylene glycol (e.g., Supelcowax 10, Carbowax 20M, and DB-Wax), acidified polyethylene glycol, and 86% dimethyl-14% cyanopropylphenylpolysiloxane (e.g., DB-1707) [104].

2.5.4. Fatty acid profiles of edible oils

The fatty acid composition differs significantly within edible oils originating from different plant species, but geographical origin, climate conditions, and degree of ripeness can also be contributing factors responsible for differences in fatty acid composition [105]. Generally, fatty acids are categorized according to their degree of saturation, i.e., saturated or unsaturated. Unsaturated fatty acids that have at most one C-C double bond are known as monounsaturated fatty acids, while fatty acids with more than one C-C double bonds are known as polyunsaturated fatty acids [105]. Edible oils with a high relative amount of unsaturated fatty acids are an essential component of a healthy diet [106]. For example, linoleic acid (C18:2) and linolenic acid (C18:3) are omega-6 and omega-3 essential fatty acids, respectively, which cannot be produced by the human body and must be obtained from consumable products [107].

Palmitic acid (C16:0), stearic acid (C18:0), oleic acid (C18:1), linoleic acid (C18:2), and linolenic acid (C18:3) are the major fatty acids commonly found in edible oils. In general, the edible oil type can be determined by the relative amounts of the five most abundant fatty acids.

These relative amounts determine the chemical and physical properties of the edible oils as well [90]. The internationally established ranges of the main fatty acids in edible oils are summarized in Table 2.2 for sunflower oil, canola oil, and extra virgin olive oil.

Table 2.2: *Established ranges of the most abundant fatty acids in edible oils.*

Edible oil	Fatty acid composition range (%)				
	C16:0	**C18:0**	**C18:1**	**C18:2**	**C18:3**
Sunflower oil[a]	5.0-7.6	2.7-6.5	14.0-39.4	48.3-74.0	≤0.3
Canola oil[a]	2.5-7.0	0.8-3.0	51.0-70.0	15.0-30.0	5.0-13.0
Extra virgin olive oil[b]	7.5-20.0	0.5-5.0	55.0-83.0	3.5-21.0	<1.5

[a] *Codex Standard for Named Vegetable Oils (CX-STAN 210 1999) [108].* [b] *Codex Standard for Olive Oil, Virgin and Refined, and for Refined Olive-Pomace Oil (CODEX STAN 33-1981 (Rev. 1-1989)) [109].*

Sunflower oil and canola oil are commonly found in households worldwide. Sunflowers (*Helianthus annuus* L.) grow in areas with mild temperature ranges and can thrive in dry and sunny conditions with soil capable of retaining water [110]. Sunflower seeds are grown and consumed globally and are primarily harvested for oil production since the seed contains 35-42% oil [111]. Standard sunflower oils are naturally abundant in linoleic (C18:2) and oleic acid (C18:1) with lower amounts of palmitic (C16:0) and stearic acid (C18:0) [112]. Conventional plant breeding techniques using rapeseed resulted in the development of canola (*Brassica napus* L.) oilseed plants that were fit for human consumption because the amounts of erucic acid (C22:1) was lowered [113]. The global production of canola seed oil exceeds that of soybean and sunflower oil [106]. Canola oil is characteristically rich in oleic (C18:1) and linoleic acid (C18:2) and contains lower amounts of palmitic (C16:0), stearic (C18:0), and linolenic acid (C18:3) [113].

Olive oil and avocado oil are expensive [89,114] and can be considered luxury food items. However, these oils are known for their health benefits [114,115]. There are six types of edible olive oils: extra virgin olive oil, virgin olive oil, refined olive oil, regular olive oil (mixture of refined and virgin olive oil), refined residue oil, and residue olive oil [116]. Extra virgin olive

oil is the commercial classification that indicates that the oil was obtained by cold pressing olives (*Olea europaea*) with mechanical extraction and no artificial processing [116,117].

Avocado (*Persea americana* Mill.) trees grow in warm subtropical climates and is frost sensitive. There are several varieties of avocado, but Hass, Fuerte, and Wagner are the most popular varieties [118]. In industry, avocados are used in the production of oil. Lipids are extracted from the lipid rich mesocarp (pulp) instead of the seed since the seed contains low levels of oil (~2%) and contains hepatotoxic agents [119]. Much like olive oil, avocado oil can be divided into three types: Pure, virgin, and extra virgin (ordered from lowest to highest quality). This classification is based on extraction method and fruit quality [120]. There are no international guidelines for the regulation of avocado oil fatty acid content [120]. However, the fatty acid composition of avocado oil is similar to that of olive oil [114,120,121] and therefore serves as a reference. Characteristically, both oil types consist predominantly of the monounsaturated fatty acid, oleic acid (C18:1) (>50%) [121]. Avocado and olive oil are highly valued oils, therefore oil adulteration is a common occurrence in commercial products [114,116,117].

Edible oils from a single source are not the only edible oil type commonly used. The blending of two oils is a common practice in industry in order to improve oxidative stability, the desired fatty acid profile and functional property [107]. In terms of nutrition, unsaturated oils are preferred over saturated oil types since the consumption of the latter is related to cardiovascular diseases. However, unsaturated oils are more prone to oxidation when heated compared to saturated oils. Thus, oils are blended to have low relative saturated fatty acid content and good oxidative stability at cooking temperatures. For example, soybean oil is a well-known healthy oil to consume, however due to its high unsaturated fatty acid content, it is unstable at cooking temperatures. Therefore, in order to produce a healthy oil with good cooking stability it is blended with a high saturated fatty acid oil such as palm or coconut oil [107]. It is noteworthy to mention that high oleic oils (canola and olive oil) are suitable for frying, however, to reduce costs these oils can be blended with oils that are high in linolenic acid content, such as corn oil [107].

Remarkably, there are few literature reports demonstrating the derivatization of TAGs to FAMEs in edible oils for GC analysis using fluidic reactors (micro- and mesoreactors). A possible reason for this could be the prohibitive cost of commercial equipment. A solution to make derivatization reactions more economically viable, would be to use open-source hardware and software for the in-house manufacturing of all flow components.

2.6. References

[1] M. Baumann, T.S. Moody, M. Smyth, S. Wharry, A Perspective on Continuous Flow Chemistry in the Pharmaceutical Industry, Organic Process Research and Development. (2020). https://doi.org/10.1021/acs.oprd.9b00524.

[2] F.M. Akwi, P. Watts, Continuous flow chemistry: where are we now? Recent applications, challenges and limitations, Chemical Communications. 54 (2018) 13894–13928. https://doi.org/10.1039/c8cc07427e.

[3] J. Britton, C.L. Raston, Multi-step continuous-flow synthesis, Chemical Society Reviews. 46 (2017) 1250–1271. https://doi.org/10.1039/c6cs00830e.

[4] J. Wegner, S. Ceylan, A. Kirschning, Ten key issues in modern flow chemistry, Chemical Communications. 47 (2011) 4583–4592. https://doi.org/10.1039/c0cc05060a.

[5] S.B. Ötvös, I.M. Mándity, F. Fülöp, Highly efficient 1,4-addition of aldehydes to nitroolefins: Organocatalysis in continuous flow by solid-supported peptidic catalysts, ChemSusChem. 5 (2012) 266–269. https://doi.org/10.1002/cssc.201100332.

[6] K.F. Jensen, B.J. Reizman, S.G. Newman, Tools for chemical synthesis in microsystems, Lab on a Chip. 14 (2014) 3206–3212. https://doi.org/10.1039/c4lc00330f.

[7] M.B. Plutschack, B. Pieber, K. Gilmore, P.H. Seeberger, The Hitchhiker's Guide to Flow Chemistry, Chemical Reviews. 117 (2017) 11796–11893. https://doi.org/10.1021/acs.chemrev.7b00183.

[8] F. Darvas, V. Hessel, G. Dorman, Fundamentals. In Flow Chemistry, 1st ed., de Gruyter, Berlin, 2014.

[9] B.P. Mason, K.E. Price, J.L. Steinbacher, A.R. Bogdan, T.D. McQuade, Greener approaches to organic synthesis using microreactor technology, Chemical Reviews. 107 (2007) 2300–2318. https://doi.org/10.1021/cr050944c.

[10] A. Webster, J. Greenman, S.J. Haswell, Development of microfluidic devices for biomedical and clinical application, Journal of Chemical Technology and Biotechnology. 86 (2011) 10–17. https://doi.org/10.1002/jctb.2482.

[11] P.R.D. Murray, D.L. Browne, J.C. Pastre, C. Butters, D. Guthrie, S.V. Ley, Continuous flow-processing of organometallic reagents using an advanced peristaltic pumping system and the telescoped flow synthesis of (E/Z)-tamoxifen, Organic Process Research and Development. 17 (2013) 1192–1208. https://doi.org/10.1021/op4001548.

[12] V.E. Garcia, J. Liu, J.L. DeRisi, Low-cost touchscreen driven programmable dual syringe pump for life science applications, HardwareX. 4 (2018). https://doi.org/10.1016/j.ohx.2018.e00027.

[13] J.H. Bannock, S.H. Krishnadasan, M. Heeney, J.C. de Mello, A gentle introduction to the noble art of flow chemistry, Materials Horizons. 1 (2014) 373–378. https://doi.org/10.1039/c4mh00054d.

[14] R.L. Hartman, J.P. McMullen, K.F. Jensen, Deciding whether to go with the flow: Evaluating the merits of flow reactors for synthesis, Angewandte Chemie - International Edition. 50 (2011) 7502–7519. https://doi.org/10.1002/anie.201004637.

[15] V. Hessel, H. Löwe, F. Schönfeld, Micromixers - A review on passive and active mixing principles, in: Chemical Engineering Science, 2005: pp. 2479–2501. https://doi.org/10.1016/j.ces.2004.11.033.

[16] M.R. Penny, N. Tsui, S.T. Hilton, Extending practical flow chemistry into the undergraduate curriculum via the use of a portable low-cost 3D printed continuous flow system, Journal of Flow Chemistry. 11 (2021) 19–29. https://doi.org/10.1007/s41981-020-00122-5.

[17] N.G. Anderson, Using continuous processes to increase production, Organic Process Research and Development. 16 (2012) 852–869. https://doi.org/10.1021/op200347k.

[18] A. Ghanem, T. Lemenand, D. della Valle, H. Peerhossaini, Static mixers: Mechanisms, applications, and characterization methods - A review, Chemical Engineering Research and Design. 92 (2014) 205–228. https://doi.org/10.1016/j.cherd.2013.07.013.

[19] J. Bao, G.K. Tranmer, The utilization of copper flow reactors in organic synthesis, Chemical Communications. 51 (2015) 3037–3044. https://doi.org/10.1039/c4cc09221j.

[20] F.E. Valera, M. Quaranta, A. Moran, J. Blacker, A. Armstrong, J.T. Cabral, D.G. Blackmond, The flow's the thing or is it? assessing the merits of homogeneous reactions

in flask and flow, Angewandte Chemie - International Edition. 49 (2010) 2478–2485. https://doi.org/10.1002/anie.200906095.

[21] C.G. Frost, L. Mutton, Heterogeneous catalytic synthesis using microreactor technology, Green Chemistry. 12 (2010) 1687–1703. https://doi.org/10.1039/c0gc00133c.

[22] R. Munirathinam, J. Huskens, W. Verboom, Supported catalysis in continuous-flow microreactors, Advanced Synthesis and Catalysis. 357 (2015) 1093–1123. https://doi.org/10.1002/adsc.201401081.

[23] G. Jas, A. Kirschning, Continuous Flow Techniques in Organic Synthesis, Chemistry - A European Journal. 9 (2003) 5708–5723. https://doi.org/10.1002/chem.200305212.

[24] R. Porta, M. Benaglia, A. Puglisi, Flow Chemistry: Recent Developments in the Synthesis of Pharmaceutical Products, Organic Process Research and Development. 20 (2016) 2–25. https://doi.org/10.1021/acs.oprd.5b00325.

[25] W. Liu, Multi-scale catalyst design, Chemical Engineering Science. 62 (2007) 3502–3512. https://doi.org/10.1016/j.ces.2007.02.057.

[26] K.F. Jensen, M.W. Bedore, N. Zaborenko, T.F. Jamison, Aminolysis of epoxides in a microreactor system: A continuous flow approach to β-Amino alcohols, Organic Process Research and Development. 14 (2010) 432–440. https://doi.org/10.1021/op9003136.

[27] S.V. Ley, D.E. Fitzpatrick, R.M. Myers, C. Battilocchio, R.J. Ingham, Machine-Assisted Organic Sunthesis, Angewandte Chemie. 127 (2015) 10260–10275. https://doi.org/10.1002/ange.201501618.

[28] C. Wiles, P. Watts, Continuous flow reactors: A perspective, Green Chemistry. 14 (2012) 38–54. https://doi.org/10.1039/c1gc16022b.

[29] J.M. Sauks, D. Mallik, Y. Lawryshyn, T. Bender, M. Organ, A continuous-flow microwave reactor for conducting high-temperature and high-pressure chemical reactions, Organic Process Research and Development. 18 (2014) 1310–1314. https://doi.org/10.1021/op400026g.

[30] D. Webb, T.F. Jamison, Continuous flow multi-step organic synthesis, Chemical Science. 1 (2010) 675–680. https://doi.org/10.1039/c0sc00381f.

[31] C.R. Sagandira, M. Siyawamwaya, P. Watts, 3D printing and continuous flow chemistry technology to advance pharmaceutical manufacturing in developing countries, Arabian Journal of Chemistry. 13 (2020) 7886–7908. https://doi.org/10.1016/j.arabjc.2020.09.020.

[32] C.K. Fredrickson, Z.H. Fan, Macro-to-micro interfaces for microfluidic devices, Lab on a Chip. 4 (2004) 526–533. https://doi.org/10.1039/b410720a.

[33] Y. Temiz, R.D. Lovchik, G.V. Kaigala, E. Delamarche, Lab-on-a-chip devices: How to close and plug the lab?, Microelectronic Engineering. 132 (2015) 156–175. https://doi.org/10.1016/j.mee.2014.10.013.

[34] A.J.N. Price, A.J. Capel, R.J. Lee, P. Pradel, S.D.R. Christie, An open source toolkit for 3D printed fluidics, Journal of Flow Chemistry. (2020). https://doi.org/10.1007/s41981-020-00117-2.

[35] B. Gross, S.Y. Lockwood, D.M. Spence, Recent Advances in Analytical Chemistry by 3D Printing, Analytical Chemistry. 89 (2017) 57–70. https://doi.org/10.1021/acs.analchem.6b04344.

[36] S. Rossi, A. Puglisi, M. Benaglia, Additive Manufacturing Technologies: 3D Printing in Organic Synthesis, ChemCatChem. 10 (2018) 1512–1525. https://doi.org/10.1002/cctc.201701619.

[37] V. Saggiomo, 3D Printed Devices for Catalytic Systems, in: M. Benaglia, A. Puglisi (Eds.), Catalyst Immobilization, Wiley, 2020: pp. 369–408. https://doi.org/10.1002/9783527817290.ch11.

[38] M. Renner, A. Griesbeck, Think and Print: 3D Printing of Chemical Experiments, Journal of Chemical Education. 97 (2020) 3683–3689. https://doi.org/10.1021/acs.jchemed.0c00416.

[39] B.C. Gross, J.L. Erkal, S.Y. Lockwood, C. Chen, D.M. Spence, Evaluation of 3D Printing and Its Potential Impact on Biotechnology and the Chemical Sciences, Analytical Chemistry. 86 (2014) 3240–3253. https://doi.org/10.1021/ac403397r.

[40] S. Waheed, J.M. Cabot, N.P. Macdonald, T. Lewis, R.M. Guijt, B. Paull, M.C. Breadmore, 3D printed microfluidic devices: enablers and barriers, Lab on a Chip. 16 (2016) 1993–2013. https://doi.org/10.1039/C6LC00284F.

[41] H. Agrawaal, J.E. Thompson, Additive manufacturing (3D printing) for analytical chemistry, Talanta Open. 3 (2021) 100036. https://doi.org/10.1016/j.talo.2021.100036.

[42] E.G. Gordeev, E.S. Degtyareva, V.P. Ananikov, Analysis of 3D printing possibilities for the development of practical applications in synthetic organic chemistry, Russian Chemical Bulletin. 65 (2016) 1637–1643. https://doi.org/10.1007/s11172-016-1492-y.

[43] C. Parra-Cabrera, C. Achille, S. Kuhn, R. Ameloot, 3D printing in chemical engineering and catalytic technology: structured catalysts, mixers and reactors, Chemical Society Reviews. 47 (2018) 209–230. https://doi.org/10.1039/C7CS00631D.

[44] M.R. Hartings, Z. Ahmed, Chemistry from 3D printed objects, Nature Reviews Chemistry. 3 (2019) 305–314. https://doi.org/10.1038/s41570-019-0097-z.

[45] P.J. Kitson, S. Glatzel, W. Chen, C.G. Lin, Y.F. Song, L. Cronin, 3D printing of versatile reactionware for chemical synthesis, Nature Protocols. 11 (2016) 920–936. https://doi.org/10.1038/nprot.2016.041.

[46] G. Gaal, M. Mendes, T.P. de Almeida, M.H.O. Piazzetta, Â.L. Gobbi, A. Riul, V. Rodrigues, Simplified fabrication of integrated microfluidic devices using fused deposition modeling 3D printing, Sensors and Actuators B: Chemical. 242 (2017) 35–40. https://doi.org/10.1016/j.snb.2016.10.110.

[47] K. Deshmukh, M. Basheer Ahamed, R.R. Deshmukh, S.K. Khadheer Pasha, P.R. Bhagat, K. Chidambaram, Biopolymer Composites With High Dielectric Performance: Interface Engineering, in: Biopolymer Composites in Electronics, Elsevier, 2017: pp. 27–128. https://doi.org/10.1016/B978-0-12-809261-3.00003-6.

[48] H.A. Maddah, Polypropylene as a Promising Plastic: A Review, American Journal of Polymer Science. 6 (2016) 1–11. https://doi.org/10.5923/j.ajps.20160601.01.

[49] J.M. Neumaier, A. Madani, T. Klein, T. Ziegler, Low-budget 3D-printed equipment for continuous flow reactions, Beilstein Journal of Organic Chemistry. 15 (2019) 558–566. https://doi.org/10.3762/bjoc.15.50.

[50] V. Dragone, V. Sans, M.H. Rosnes, P.J. Kitson, L. Cronin, 3D-printed devices for continuous-flow organic chemistry, Beilstein Journal of Organic Chemistry. 9 (2013) 951–959. https://doi.org/10.3762/bjoc.9.109.

[51] Z.X. Rao, B. Patel, A. Monaco, Z.J. Cao, M. Barniol-Xicota, E. Pichon, M. Ladlow, S.T. Hilton, 3D-Printed Polypropylene Continuous-Flow Column Reactors: Exploration of Reactor Utility in S_NAr Reactions and the Synthesis of Bicyclic and Tetracyclic Heterocycles, European Journal of Organic Chemistry. 2017 (2017) 6499–6504. https://doi.org/10.1002/ejoc.201701111.

[52] O.A. Alimi, T.B. Ncongwane, R. Meijboom, Design and fabrication of a monolith catalyst for continuous flow epoxidation of styrene in polypropylene printed flow reactor, Chemical Engineering Research and Design. 159 (2020) 395–409. https://doi.org/10.1016/j.cherd.2020.04.025.

[53] F. Menzel, T. Klein, T. Ziegler, J.M. Neumaier, 3D-printed PEEK reactors and development of a complete continuous flow system for chemical synthesis, Reaction Chemistry & Engineering. 5 (2020) 1300–1310. https://doi.org/10.1039/D0RE00206B.

[54] D.M. Heard, A.J.J. Lennox, Minimal manual input, Nature Chemistry. 12 (2020) 113–114. https://doi.org/10.1038/s41557-019-0416-5.

[55] B. Wijnen, E.J. Hunt, G.C. Anzalone, J.M. Pearce, Open-source syringe pump library, PLoS ONE. 9 (2014). https://doi.org/10.1371/journal.pone.0107216.

[56] V. Klar, J.M. Pearce, P. Kärki, P. Kuosmanen, Ystruder: Open source multifunction extruder with sensing and monitoring capabilities. https://doi.org/10.17605/OSF.IO/T9HPE.

[57] K. Akash, M.P. Kumar, N. Venkatesan, M. Venkatesan, A single acting syringe pump based on Raspberry Pi - SOC, in: 2015 IEEE International Conference on Computational Intelligence and Computing Research (ICCIC), IEEE, 2015: pp. 1–3. https://doi.org/10.1109/ICCIC.2015.7435694.

[58] M.S. Cubberley, W.A. Hess, An inexpensive programmable dual-syringe pump for the chemistry laboratory, Journal of Chemical Education. 94 (2017) 72–74. https://doi.org/10.1021/acs.jchemed.6b00598.

[59] J.R. Lake, K.C. Heyde, W.C. Ruder, Low-cost feedback-controlled syringe pressure pumps for microfluidics applications, PLoS ONE. 12 (2017). https://doi.org/10.1371/journal.pone.0175089.

[60] R.J. LeSuer, K.L. Osgood, K.E. Stelnicki, J.L. Mendez, OMIS: The Open Millifluidic Inquiry System for small scale chemical synthesis and analysis, HardwareX. 4 (2018) e00038. https://doi.org/10.1016/j.ohx.2018.e00038.

[61] A.S. Samokhin, Syringe Pump Created using 3D Printing Technology and Arduino Platform, Journal of Analytical Chemistry. 75 (2020) 416–421. https://doi.org/10.1134/S1061934820030156.

[62] A.S. Booeshaghi, E.d.V. Beltrame, D. Bannon, J. Gehring, L. Pachter, Principles of open source bioinstrumentation applied to the poseidon syringe pump system, Scientific Reports. 9 (2019) 1–8. https://doi.org/10.1038/s41598-019-48815-9.

[63] L. Joswig, M.J. Vellekoop, F. Lucklum, Miniature 3D-printed centrifugal pump with non-contact electromagnetic actuation, Micromachines. 10 (2019). https://doi.org/10.3390/mi10100631.

[64] M.R. Behrens, H.C. Fuller, E.R. Swist, J. Wu, M.M. Islam, Z. Long, W.C. Ruder, R. Steward, Open-source, 3D-printed Peristaltic Pumps for Small Volume Point-of-Care Liquid Handling, Scientific Reports. 10 (2020) 1543. https://doi.org/10.1038/s41598-020-58246-6.

[65] J.J. Davis, M. Padalino, A.S. Kaplitz, G. Murray, S.W. Foster, J. Maturano, J.P. Grinias, Utility of low-cost, miniaturized peristaltic and Venturi pumps in droplet microfluidics, Analytica Chimica Acta. 1151 (2021) 338230. https://doi.org/10.1016/j.aca.2021.338230.

[66] P.J. Kitson, M.H. Rosnes, V. Sans, V. Dragone, L. Cronin, Configurable 3D-Printed millifluidic and microfluidic "lab on a chip" reactionware devices, Lab on a Chip. 12 (2012) 3267–3271. https://doi.org/10.1039/c2lc40761b.

[67] J.S. Mathieson, M.H. Rosnes, V. Sans, P.J. Kitson, L. Cronin, Continuous parallel ESI-MS analysis of reactions carried out in a bespoke 3D printed device, Beilstein Journal of Nanotechnology. 4 (2013) 285–291. https://doi.org/10.3762/bjnano.4.31.

[68] P.J. Kitson, M.D. Symes, V. Dragone, L. Cronin, Combining 3D printing and liquid handling to produce user-friendly reactionware for chemical synthesis and purification, Chem. Sci. 4 (2013) 3099–3103. https://doi.org/10.1039/C3SC51253C.

[69] S.S. Zalesskiy, P.J. Kitson, P. Frei, A. Bubliauskas, L. Cronin, 3D designed and printed chemical generators for on demand reagent synthesis, Nature Communications. 10 (2019) 5496. https://doi.org/10.1038/s41467-019-13328-6.

[70] A.J. Capel, S. Edmondson, S.D.R. Christie, R.D. Goodridge, R.J. Bibb, M. Thurstans, Design and additive manufacture for flow chemistry, Lab on a Chip. 13 (2013) 4583. https://doi.org/10.1039/c3lc50844g.

[71] T. Tabassum, M. Iloska, D. Scuereb, N. Taira, C. Jin, V. Zaitsev, F. Afshar, T. Kim, Development and Application of 3D Printed Mesoreactors in Chemical Engineering Education, Journal of Chemical Education. 95 (2018) 783–790. https://doi.org/10.1021/acs.jchemed.7b00663.

[72] S. Rossi, R. Porta, D. Brenna, A. Puglisi, M. Benaglia, Stereoselective Catalytic Synthesis of Active Pharmaceutical Ingredients in Homemade 3D-Printed Mesoreactors, Angewandte Chemie International Edition. 56 (2017) 4290–4294. https://doi.org/10.1002/anie.201612192.

[73] D.L. Walmsley, E. Sellier, Design and development of a 3D-printed back-pressure regulator, EngrXiv [Preprint]. (2020) 1–3. https://doi.org/10.31224/osf.io/3t9bq.

[74] M.J. Harding, S. Brady, H. O'Connor, R. Lopez-Rodriguez, M.D. Edwards, S. Tracy, D. Dowling, G. Gibson, K.P. Girard, S. Ferguson, 3D printing of PEEK reactors for flow chemistry and continuous chemical processing, Reaction Chemistry and Engineering. 5 (2020) 728–735. https://doi.org/10.1039/c9re00408d.

[75] O.A. Alimi, N. Bingwa, R. Meijboom, Homemade 3-D printed flow reactors for heterogeneous catalysis, Chemical Engineering Research and Design. 150 (2019) 116–129. https://doi.org/10.1016/j.cherd.2019.07.024.

[76] O.A. Alimi, C.A. Akinnawo, O.R. Onisuru, R. Meijboom, 3-D printed microreactor for continuous flow oxidation of a flavonoid, Journal of Flow Chemistry. 10 (2020) 517–531. https://doi.org/10.1007/s41981-020-00089-3.

[77] O.A. Alimi, T.B. Ncongwane, R. Meijboom, Design and fabrication of a monolith catalyst for continuous flow epoxidation of styrene in polypropylene printed flow reactor, Chemical Engineering Research and Design. 159 (2020) 395–409. https://doi.org/10.1016/j.cherd.2020.04.025.

[78] O.R. Onisuru, O.A. Alimi, K. Potgieter, R. Meijboom, Continuous-Flow Catalytic Degradation of Hexacyanoferrate Ion through Electron Transfer Induction in a 3D-Printed Flow Reactor, Journal of Materials Engineering and Performance. (2021). https://doi.org/10.1007/s11665-021-05527-4.

[79] G.W. Bishop, J.E. Satterwhite, S. Bhakta, K. Kadimisetty, K.M. Gillette, E. Chen, J.F. Rusling, 3D-Printed fluidic devices for nanoparticle preparation and flow-injection amperometry using integrated prussian blue nanoparticle-modified electrodes, Analytical Chemistry. 87 (2015) 5437–5443. https://doi.org/10.1021/acs.analchem.5b00903.

[80] S. Vijayan, M. Hashimoto, 3D printed fittings and fluidic modules for customizable droplet generators, RSC Advances. 9 (2019) 2822–2828. https://doi.org/10.1039/C8RA08686A.

[81] S. Tsuda, H. Jaffery, D. Doran, M. Hezwani, P.J. Robbins, M. Yoshida, L. Cronin, Customizable 3D Printed 'Plug and Play' Millifluidic Devices for Programmable Fluidics, PLOS ONE. 10 (2015) e0141640. https://doi.org/10.1371/journal.pone.0141640.

[82] A.J.L. Morgan, L. Hidalgo San Jose, W.D. Jamieson, J.M. Wymant, B. Song, P. Stephens, D.A. Barrow, O.K. Castell, Simple and Versatile 3D Printed Microfluidics Using Fused Filament Fabrication, PLOS ONE. 11 (2016) e0152023. https://doi.org/10.1371/journal.pone.0152023.

[83] J.M. Zhang, Q. Ji, H. Duan, Three-dimensional printed devices in droplet microfluidics, Micromachines. 10 (2019). https://doi.org/10.3390/mi10110754.

[84] J.M. Zhang, A.A. Aguirre-Pablo, E.Q. Li, U. Buttner, S.T. Thoroddsen, Droplet generation in cross-flow for cost-effective 3D-printed "plug-and-play" microfluidic devices, RSC Advances. 6 (2016) 81120–81129. https://doi.org/10.1039/C6RA11724D.

[85] M.R. Penny, Z.X. Rao, B.F. Peniche, S.T. Hilton, Modular 3D Printed Compressed Air Driven Continuous-Flow Systems for Chemical Synthesis, European Journal of Organic Chemistry. 2019 (2019) 3783–3787. https://doi.org/10.1002/ejoc.201900423.

[86] S.C. Moldoveanu, Solutions and Challenges in Sample Preparation for Chromatography, Journal of Chromatographic Science. 42 (2004) 1–14. https://doi.org/10.1093/chromsci/42.1.1.

[87] F. Li, M.R. Ceballos, S.K. Balavandy, J. Fan, M.M. Khataei, Y. Yamini, F. Maya, 3D Printing in analytical sample preparation, Journal of Separation Science. 43 (2020) 1854–1866. https://doi.org/10.1002/jssc.202000035.

[88] H.L. Lord, E.A. Pfannkoch, Sample Preparation Automation for GC Injection, in: Comprehensive Sampling and Sample Preparation, Elsevier, 2012: pp. 597–612. https://doi.org/10.1016/B978-0-12-381373-2.00061-2.

[89] S. Indelicato, D. Bongiorno, R. Pitonzo, V. di Stefano, V. Calabrese, S. Indelicato, G. Avellone, Triacylglycerols in edible oils: Determination, characterization, quantitation, chemometric approach and evaluation of adulterations, Journal of Chromatography A. 1515 (2017) 1–16. https://doi.org/10.1016/j.chroma.2017.08.002.

[90] E. Tammekivi, S. Vahur, O. Kekišev, I.D. van der Werf, L. Toom, K. Herodes, I. Leito, Comparison of derivatization methods for the quantitative gas chromatographic analysis of oils, Analytical Methods. 11 (2019) 3514–3522. https://doi.org/10.1039/C9AY00954J.

[91] K.-S. Liu, Preparation of fatty acid methyl esters for gas-chromatographic analysis of lipids in biological materials, Journal of the American Oil Chemists' Society. 71 (1994) 1179–1187. https://doi.org/10.1007/BF02540534.

[92] Z. Wu, Q. Zhang, N. Li, Y. Pu, B. Wang, T. Zhang, Comparison of critical methods developed for fatty acid analysis: A review, Journal of Separation Science. 40 (2017) 288–298. https://doi.org/10.1002/jssc.201600707.

[93] U. Schuchardt, R. Sercheli, R.M. Vargas, Transesterification of vegetable oils: a review, Journal of the Brazilian Chemical Society. 9 (1998) 199–210. https://doi.org/10.1590/S0103-50531998000300002.

[94] N.C. Shantha, G.E. Napolitano, Gas chromatography of fatty acids, Journal of Chromatography A. 624 (1992) 37–51. https://doi.org/10.1016/0021-9673(92)85673-H.

[95] B. Suter, K. Grob, B. Pacciarelli, Determination of fat content and fatty acid composition through 1-min transesterification in the food sample; principles, Z Lebensm Unters Forsch A. 204 (1997) 252–258. https://doi.org/https://doi.org/10.1007/s002170050073.

[96] C.T. Srigley, M.M. Mossoba, Current analytical techniques for food lipids, Food Safety: Innovative Analytical Tools for Safety Assessment. (2016) 33–64. https://doi.org/10.1002/9781119160588.ch3.

[97] S. de Koning, B. van der Meer, G. Alkema, H.-G. Janssen, U.A.Th. Brinkman, Automated determination of fatty acid methyl ester and cis/trans methyl ester composition of fats and oils, Journal of Chromatography A. 922 (2001) 391–397. https://doi.org/10.1016/S0021-9673(01)00926-8.

[98] C.T. Duong, M.G. Roper, A microfluidic device for the automated derivatization of free fatty acids to fatty acidmethylesters, The Analyst. 137 (2012) 840–846. https://doi.org/10.1039/C2AN15911B.

[99] B. Schilling, R. Bolliger, G. Boehm, Automated Workflow for the Transesterification of Fatty Acid Methyl Esters (FAME) in Fat and Fat Containing Food Samples Using a 90 Sec. Transesterification, https://www.palsystem.com/fileadmin/public/docs/Downloads/Posters/Automated_Generation___Analysis_of_FAME_GC_ISCC_Riva_2014_Poster.pdf (accessed September 30, 2020).

[100] E. Ballesteros, M. Gallego, M. Valcárcel, Automatic method for on-line preparation of fatty acid methyl esters from olive oil and other types of oil prior to their gas chromatographic determination, Analytica Chimica Acta. 282 (1993) 581–588. https://doi.org/10.1016/0003-2670(93)80123-3.

[101] D.A. Skoog, D.M. West, F.J. Holler, S.R. Crouch, Gas Chromatography, in: Fundamentals of Analytical Chemistry, 9th ed., Cengage Learning, 2014: pp. 857–893.

[102] Z. Wang, J.R. Jocelyn Paré, Chapter 3 Gas chromatography (GC): Principles and applications, in: J.R.J. Paré, J.M.R. Bélanger (Eds.), Techniques and Instrumentation in Analytical Chemistry, Elsevier, 1997: pp. 61–91. https://doi.org/10.1016/S0167-9244(97)80012-1.

[103] D.A. Skoog, F.J. Holler, S.R. Crouch, Gas Chromatography, in: Principles of Instrumental Analysis, 7th ed., Cengage Learning, 2018: pp. 720–726.

[104] K. Eder, Gas chromatographic analysis of fatty acid methyl esters, Journal of Chromatography B: Biomedical Sciences and Applications. 671 (1995) 113–131. https://doi.org/10.1016/0378-4347(95)00142-6.

[105] V. Ivanova-Petropulos, S. Mitrev, T. Stafilov, N. Markova, E. Leitner, E. Lankmayr, B. Siegmund, Characterisation of traditional Macedonian edible oils by their fatty acid composition and their volatile compounds, Food Research International. 77 (2015) 506–514. https://doi.org/10.1016/j.foodres.2015.08.014.

[106] H. Omidi, Z. Tahmasebi, H.A. Naghdi Badi, H. Torabi, M. Miransari, Fatty acid composition of canola (Brassica napus L.), as affected by agronomical, genotypic and environmental parameters, Comptes Rendus Biologies. 333 (2010) 248–254. https://doi.org/10.1016/j.crvi.2009.10.001.

[107] A. Dhyani, R. Chopra, M. Garg, A Review on Blending of Oils and Their Functional and Nutritional Benefits, Chem Sci Rev Lett. 7 (2018) 840–847. http://chesci.com/wp-content/uploads/2019/04/V7i27_19_CS062049071_Akriti_840-847.pdf.

[108] C. Alimentarius, Codex Standard for named vegetable oils. CX-STAN 210-1999, Codex Aliment. 8 (2001) 11–25. http://www.fao.org/3/y2774e/y2774e04.htm#bm4.1 (accessed March 10, 2021).

[109] C. Alimentarius, Codex standard for olive oil, virgin and refined, and for refined olive-pomace oil. CODEX-STAN 33-1981 (Rev. 1-1989), Codex Aliment. 8 (2001) 25–39. http://www.fao.org/3/y2774e/y2774e04.htm#bm4.2 (accessed March 10, 2021).

[110] M.A. Grompone, Sunflower Oil, 2nd ed., Wiley-Blackwell, Oxford, UK, 2011. https://doi.org/10.1002/9781444339925.ch5.

[111] S. Guo, Y. Ge, K. Na Jom, A review of phytochemistry, metabolite changes, and medicinal uses of the common sunflower seed and sprouts (Helianthus annuus L.), Chemistry Central Journal. 11 (2017) 1–10. https://doi.org/10.1186/s13065-017-0328-7.

[112] R. Garcés, E. Martínez-Force, J.J. Salas, M. Venegas-Calerón, Current advances in sunflower oil and its applications, Lipid Technology. 21 (2009) 79–82. https://doi.org/10.1002/lite.200900016.

[113] B. Matthaus, M.M. Özcan, F. al Juhaimi, Some rape/canola seed oils: fatty acid composition and tocopherols, Zeitschrift Für Naturforschung C. 71 (2016) 73–77. https://doi.org/10.1515/znc-2016-0003.

[114] A.A. Rydlewski, J.S. Pizzo, L.P. Manin, M.B. Galuch, P.D.S. Santos, C. Zapiello, O.O. Santos, J. v. Visentainer, Evaluation of possible fraud in avocado oil-based products from the composition of fatty acids by GC-FID and lipid profile by ESI-MS, Chemical Papers. 74 (2020) 2799–2812. https://doi.org/10.1007/s11696-020-01119-z.

[115] A. Rotondo, G.L. la Torre, G. Dugo, N. Cicero, A. Santini, A. Salvo, Oleic Acid Is not the Only Relevant Mono-Unsaturated Fatty Ester in Olive Oil, Foods. 9 (2020) 384. https://doi.org/10.3390/foods9040384.

[116] A. Rohman, Y.B. Che Man, Authentication of Extra Virgin Olive Oil from Sesame Oil Using FTIR Spectroscopy and Gas Chromatography, International Journal of Food Properties. 15 (2012) 1309–1318. https://doi.org/10.1080/10942912.2010.521607.

[117] F. Siano, E. Vasca, GC-FID Analysis to Evaluate the Possible Adulteration of Extra Virgin Olive Oil with Different Vegetable Oils, Journal of Chemical Education. 97 (2020) 4108–4116. https://doi.org/10.1021/acs.jchemed.0c00278.

[118] C.X. Tan, S.S. Tan, S.T. Tan, Influence of Geographical Origins on the Physicochemical Properties of Hass Avocado Oil, Journal of the American Oil Chemists' Society. 94 (2017) 1431–1437. https://doi.org/10.1007/s11746-017-3042-7.

[119] X. Qin, J. Zhong, A Review of Extraction Techniques for Avocado Oil, Journal of Oleo Science. 65 (2016) 881–888. https://doi.org/10.5650/jos.ess16063.

[120] M. Flores, C. Saravia, C.E. Vergara, F. Avila, H. Valdés, J. Ortiz-Viedma, Avocado oil: Characteristics, properties, and applications, Molecules. 24 (2019) 1–21. https://doi.org/10.3390/molecules24112172.

[121] F.D. Krumreich, C.D. Borges, C.R.B. Mendonça, C. Jansen-Alves, R.C. Zambiazi, Bioactive compounds and quality parameters of avocado oil obtained by different

processes, Food Chemistry. 257 (2018) 376–381. https://doi.org/10.1016/j.foodchem.2018.03.048.

Chapter 3: Materials and methods

3.1. Poseidon syringe pump system

3.1.1. Materials

Flexible aluminium couplings (5 mm / 5 mm), linear ball bearings (LM6UU, 6 mm diameter), Steel rod (length 200 mm, diameter 6 mm), RS PRO plain stainless steel threaded rod (M5 × 0.8, length 180 mm), M5 × 0.8 nuts, M3 × 0.5 socket head screws (length 20 mm), M3 × 0.5 socket head screws (length 10 mm), M3 nuts and RS PRO black thermoplastic knobs (M5) were purchased from RS Components. The rods came in packs of 5 with lengths of 1.00 m each and thus had to be cut to size. The Nema 17 stepper motors (0.65 Nm, 60 mm), Arduino Uno R3, Arduino computerized numerical control (CNC) shield, and A4988 stepper motor driver modules were purchased from DIY Electronics. A 12 V power unit, a cable to power unit, and connectors were purchased from Communica. PLA filament (diameter 1.75 mm) and RS PRO clear PP filament (diameter 1.75 mm) was purchased from 3D Printing Factory (PTY) LTD and RS Components, respectively. Supelco tetrafluoroethylene (TFE) tubing (1.58 mm OD × 0.8 mm ID) and flangeless ferrules (1/16”) were purchased from Merck.

The open-source Poseidon syringe pump system [1] source files were downloaded from GitHub: Pachterlab/ Poseidon (https://github.com/pachterlab/poseidon and see Appendix A1, A2, and A5). The contents were open-source, allowing the user to privately use, adjust and share the software and hardware without warranty and liability [2]. This repository of files includes a detailed parts list, CAD files of the 3D-printable hardware, pump controller and GUI software to control the Arduino microcontroller and Arduino firmware that communicate commands via USB in order to drive the stepper motors. PrusaSlic3r was used to set printing conditions (extruder and bed temperature, infill, object orientation, filament type etc.) and the G-code was then exported for printing purposes.

3.1.2. Manufacturing of 3D-printed parts

A Prusa i3 MK3S 3D-printer was used to manufacture the syringe pump bases, carriage sleds, syringe braces and cover slides using PLA as printing material. The building platform of the 3D-printer is 250 mm × 210 mm × 210 mm with a removable magnetic polyetherimide (PEI) spring steel print sheet.

The Poseidon syringe pump hardware was modified using Fusion 360, a cloud-based CAD program. The 3D-printable hardware consists of a syringe pump base, cover slide, carriage sled and a syringe brace (Figure 3.1A to 3.1D). The abovementioned 3D-printed components were fabricated by a FDM 3D-printer using PLA as printing material. Print settings included an extruder temperature of 195 °C and a bed temperature of 60 °C. A 0.4 mm nozzle was used together with a layer height of 0.15 mm. A 15% infill and 95% extruder flow were used. The components were 3D-printed with object orientation as shown in Figure 3.1. All object orientations are sufficiently stable, flat and with little to no overhang in order to avoid the need for support material in the fabrication process.

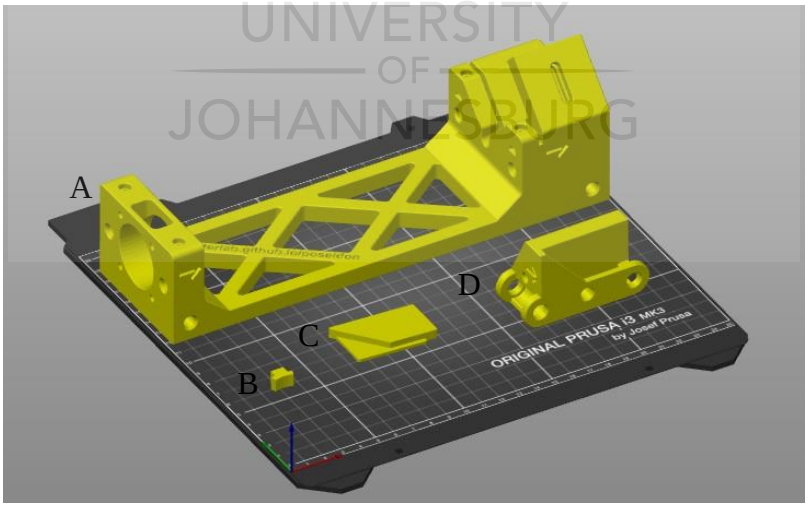

Figure 3.1: *The Poseidon syringe pump [1] hardware STL files were downloaded and imported into the PrusaSlic3r program, where the print settings was set and the G-codes were exported for 3D-printing purposes. (A) Syringe pump base. (B) Syringe brace. (C) Cover slide. (D) Carriage sled.*

3.1.3. Assembly of Poseidon pumps

Using the materials mentioned in Section 3.1.1, the Poseidon syringe pumps were assembled according to the instruction videos prepared by the original authors (see Appendix A.2) [1]. By means of a slit, the carriage sled could accommodate a wide range of commercially available syringes ranging from 1.0 mL to 60 mL. Additionally, the syringes were secured in place by the syringe brace screwed onto a male knob. The carriage sled (mounted on linear bearings) could move forwards or backwards by means of a Nema 17 stepper motor with a 1.8 ° step angle and a holding torque of 6.5 kg.cm to minimize back pressure. All commercial and 3D-printed hardware observed on the syringe pump body was secured by means of screws, nuts and rods of appropriate size (Figure 3.2A). The syringe pump system uses an Arduino board, a CNC shield, three stepper motor driver modules and an external 12 V power supply to operate three pumps simultaneously (Figure 3.2B).

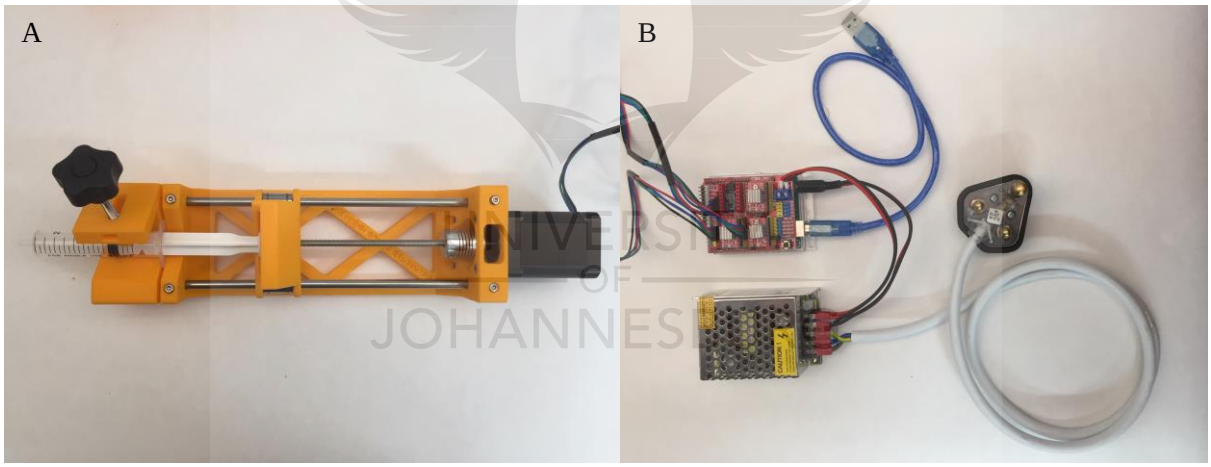

Figure 3.2: *(A) An assembled syringe pump with a 10 mL syringe securely placed on the pump body. (B) The Arduino microcontroller with a CNC shield and three stepper motor driver modules. The stepper motors are wired with Dupont wiring and connected to the CNC shield. The blue USB cable connects to a USB port on a personal computer. The 12 V power supply (with a 3-pin plug) provides a current to the CNC shield and the stepper motor driver modules in order to drive the stepper motors.*

Setting up the control of the Poseidon pump system through the provided Arduino and Python scripts were not straightforward, and thus a step-by-step protocol (see Appendix A3 to A7) was

developed to ensure correct installation and execution. The settings in the controller program are essential to obtain a controlled and smooth flow in a continuous flow system. Microstepping is used to achieve both increased step resolution and smoother transitions between steps and is dependent on the type of stepper motor driver modules placed on the CNC shield. A higher microstepping is preferred for low flow rates to achieve a smoother flow. The highest microstep selected was 16, because A4988 stepper driver modules were used. Syringe size, flow rate and amount dispensed was specified for all pumps in order to achieve a controlled continuous flow system with a smooth flow.

3.1.4. Flow rate calibration procedure

The syringe pumps were calibrated using a gravimetric method. In other words, the amount of deionised water dispensed in a vial by the syringe pumps were weighed using an analytical balance. The observed flow rate was determined using a dynamic method which consists of determining the mass or volume of the dispensed liquid per unit of time [3]. The syringes were filled with deionised water and all air bubbles were removed from the syringes and tubing before performing the calibration procedures. Several calibrations were performed. The flow rate was systematically increased to reach the recommended maximum flow rate corresponding to the syringe size [1]. Three syringe sizes (1, 5, and 10 mL) were used.

In the Poseidon operating program, it is possible to use flow rates with different units. The available flow rate units are: microlitre per hour (µL/hour), millilitre per hour (mL/hour), millimetre per second (mm/s), and millilitre per second (mL/s). Only two types of flow rate units were investigated, namely millilitre per hour (mL/hour) and millimetre per second (mm/s). The same calibration procedure was followed when using a programmed flow rate set to mL/hr or mm/s in the controller program.

In addition, Single-Factor Analysis of Variance (ANOVA) was used to determine whether the three syringe pumps in a set performed equally for a specific flow rate. Three flow rates (3.00, 6.00, and 9.00 mL/hr) with 5 mL syringes were investigated. Five repetitions were performed for each pump in the syringe pump set. The ANOVA was performed using Microsoft Excel.

3.2. 3D-printed flow components

3.2.1. Instrumentation

Two 3D-printers, a Prusa i3 MK3S and a Creality CR20 Pro were used in the self-manufacturing of the flangeless fittings kit and the modified fluidic devices using clear PP filament. This work does not aim to compare the performance of the two 3D-printers and the only reason for the use of two different printers was that only one of these printers were operational at any point in time whilst this work was completed. As mentioned above, the Prusa i3 MK3S was fitted with a removable magnetic PEI spring steel sheet. The Creality CR20 Pro had a removable magnetic cover sheet that fits onto the building platform of the 3D-printer. This sheet had to be replaced by a piece of glass (235 mm × 235 mm × 1.9 mm), because its heat resistivity is below 80 °C and its rough surface prevented the packing tape from sticking to it securely. The glass plate was secured in place by clips that were positioned in strategic places so that it will not disturb the movement of the extruder and the auto levelling BLTouch module.

The flow system components, consisting of a flangeless fittings kit and modified fluidic devices were designed using Fusion 360, a cloud-based CAD program. The STL files were converted to G-codes (with the desired print settings) for printing purposes. The modified fluidic devices were adjusted to have threaded access ports instead of spaces for in-printed screw nuts. The STL files originally designed by Neumaier et al. [4] were imported into Fusion 360, where the necessary adjustments were made. A Creality CR20 Pro 3D-printer was used to manufacture these fluidic devices by importing the new STL file into Creality Slicer 1.2.3. Here, the printing conditions were set and the G-code was exported for printing purposes.

3.2.2. Design and modification of flow system components

Models for the 3D-printed flangeless fittings kit (Figure 3.3) was based on the flangeless fittings kit (Upchurch) purchased from Merck (catalogue number 58630) for ZAR 6790.75 (ca. USD 450). It was observed that female Luers fit securely onto commercial Luer slip syringes

and was therefore redesigned as syringe adapters to facilitate leak-free connections from the syringes to other fluidic devices in a continuous flow system. Syringe adapters, flangeless nuts, male Luers, unions and mixers (modified T-connectors and crosses) were designed. All unions and mixers were designed with 1.5 mm and 2.0 mm diameter channels which can be easily adjusted. The design details of the threaded parts for each piece are described in Table 3.1. The threading is of universal standard (1/4”-28 Unified National Fine (UNF)) and is identical to that of the purchased kit, thus making the two kits compatible. Additionally, metric (M) unions and metric adapters (1/4”-28 to M6) were also designed similarly to the standard unions in the commercial kit.

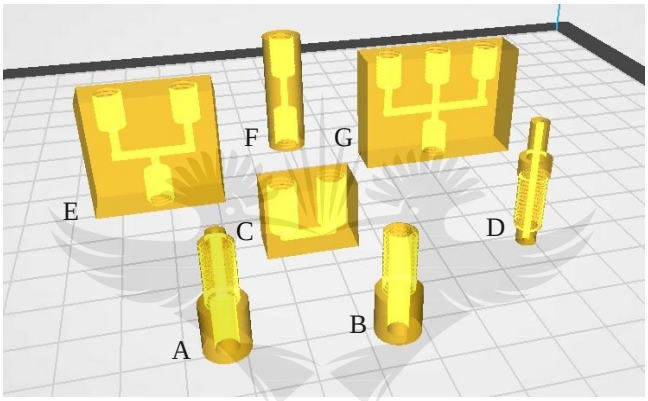

Figure 3.3: *Designs of the 3D-printed components of the flangeless fittings kit. Each design is viewed transparently in order to view the channels and access ports of each piece. (A) Syringe adapter. (B) Flangeless nut. (C) Alternative union. (D) Male Luer. (E) T-mixer. (F) Union. (G) Cross mixer.*

Table 3.1: *Thread details of the designed flangeless fittings*

Description	Adapters and flangeless nuts	Unions and mixers
Thread type	ANSI unified screw threads	ANSI unified screw threads
Size	0.25 inch	0.25 inch
Designation	1/4”-28 UNF	1/4”-28 UNF
Class	1A	1B
Direction	Right hand	Right hand

ANSI: American National Standards Institute.

The dimensions of each piece in the flangeless fittings kit can be described as follows: The syringe adapter (Figure 3.3A) was designed to have a height of 25 mm with a maximum outer diameter of 11 mm. The piece was designed to have a built-in ferrule with a height and diameter of 4 mm and 5 mm, respectively. The channel had a diameter of 2 mm, and the void at the bottom (that fits securely onto the tip of Luer slip syringes was 4.5 mm in diameter. The flangeless nut (Figure 3.3B) had a height of 21 mm, a channel with a 5 mm diameter, and a maximum outer diameter of 11 mm. The male Luer (Figure 3.3D) was designed to have a height of 28 mm and a channel diameter of 1.5 mm. The diameter of the smooth part where it is normally handled (directly above the threading) was 7 mm, and the diameters at the top and bottom of the piece was 4.5 and 5 mm, respectively. The union (Figure 3.3F) has a height of 30 mm and an outer diameter of 12 mm. Its alternative counterpart (Figure 3.3C) was designed to have a height of 15 mm, a width of 10 mm, and a length of 20 mm. The T-mixer and cross mixers (Figure 3.3E and 3.3G) had dimensions 34 mm × 10 mm × 30 mm, and 36 mm × 10 mm × 30 mm, respectively.

The flow reactors created by Neumaier et al. [4] were designed to be easily modified, and consists of a chip reactor and CSTRs with two and three access ports. The chip reactor had two initial inlets with a chaotic mixing zone (zig-zag channel) followed by serpentine-like channels, a quenching zone followed by a single outlet. The chip reactor can accommodate a maximum of 6 access ports. The reactor had a total volume of approximately 1.02 mL. The channels were square shaped with 1.2 mm × 1.2 mm diameter. The reactor itself was also square shaped with a length and width of 87.00 mm. The reaction zone was designed to be 3.00 mm high so that the channels can be visually monitored when 3D-printed with clear PP filament. The two access port CSTR had a width and height of 24.00 mm and 30.00 mm, respectively, and a tank diameter of 15.00 mm. The height from the bottom of the tank to the highest positioned channel was 12.00 mm, thus the volume of the tank was calculated to be approximately 2.1 mL. The three access port CSTR was 36.00 mm wide and 20.00 mm high with a tank diameter of 11.00 mm. The height of the tank (from the bottom to the highest positioned channel) was 5.00 mm, thus the volume of the tank was calculated to be approximately 0.48 mL. Both CSTRs had 2.00 mm diameter channels. All abovementioned fluidic devices had spaces for in-printed screw nuts to interface with standard HPLC fittings. These spaces were replaced with threaded access ports (1/4”-28 UNF) which were compatible with the threading of the 3D-printed flangeless nuts (Figure 3.4 to 3.6). In the case of the chip

reactor (Figure 3.6), the quenching inlet and its channel was closed in addition to the modification of the access ports.

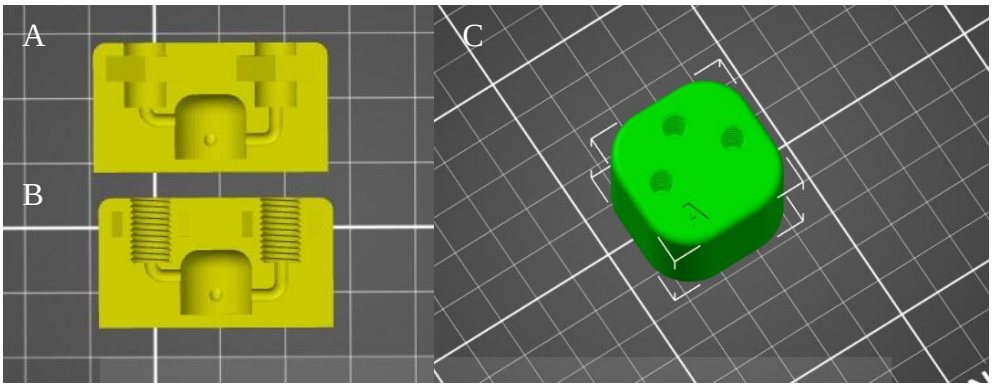

Figure 3.4: *(A) Cross-sectional view of the three access port CSTR as designed by Neumaier et al. [4]. (B) Cross-sectional view of the modified design with threaded access ports. (C) Full view of the modified CSTR.*

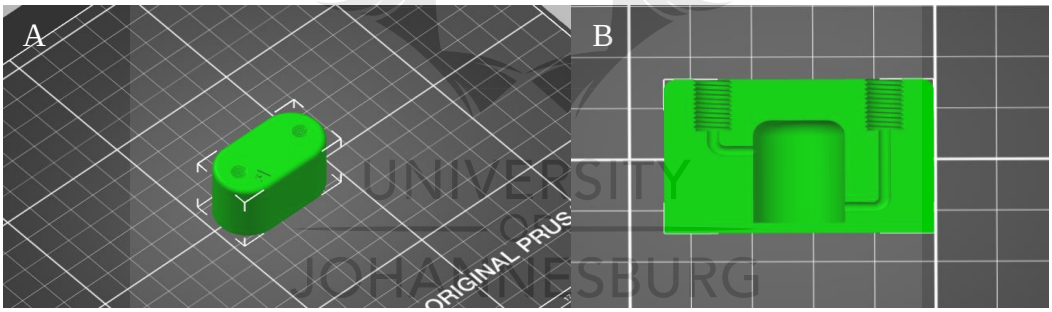

Figure 3.5: *(A) Modified two access port CSTR. (B) Cross-sectional view of the modified two access port CSTR.*

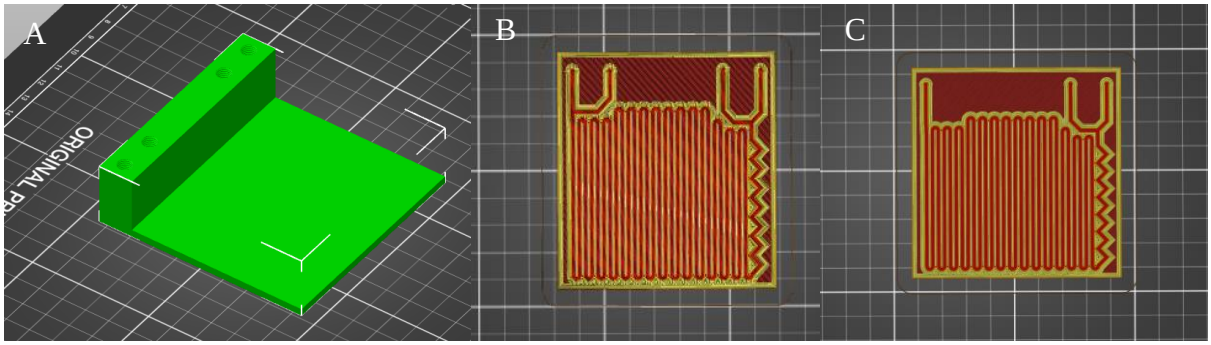

Figure 3.6: *(A) Modified chip reactor with four access ports. (B) The reaction zone of A which consist of two initial inlets (on the right) followed by a zig-zag channel (chaotic mixing zone), serpentine-like channels, a subsequent quench zone, and an outlet. The reaction zone of a three access port chip reactor where the quenching zone (access port and channel) of A was closed.*

3.2.3. Fabrication of the flow components

In this study, FDM was used in the production of the flangeless fittings kit and the modified fluidic devices. This method focuses on the extrusion of plastic filament through a heated nozzle where each layer is printed individually until the desired three-dimensional object is obtained [5–9]. FDM is an attractive alternative to other 3D-printing methods (see Chapter 2, Section 2.3.2), because both the printers [4,6,8] and materials [5,6,8] are relatively inexpensive. The 3D-printed flangeless fittings kit was manufactured in PLA and PP, whereas the flow reactor and continuous stirred tank reactors were printed using PP filament. Moreover, clear filament was chosen because the flow and mixing of reagents can be visually monitored. PP is the preferred material for the fabrication of reactionware, because it has a thermostability up to 150 °C [5] and is inert in a wide range of solvents and chemicals [4,5,7,9] however, it is challenging to 3D-print [9]. PLA has limited chemical resistivity and can only be used in temperatures ranging up to 60-66°C [5].

The design and modification steps followed for the fabrication of all 3D-printed components are summarized in Figure 3.7. The flangeless fittings were designed and fabricated following route A. First, Fusion 360, was used to design each object followed by exporting the STL file into a dedicated design folder. Next, the STL file was imported into a slicing program (PrusaSlic3r) to set the printing conditions such as object orientation and scale, layer height,

extruder and bed temperature, fill density and filament flow percent. Print settings are crucial when the aim is to obtain leak-free fluidic devices with well-defined channels. These settings are considered in detail below. After the printing was completed, the object was inspected. The fittings had to be strong and durable with threaded components that could be inserted and removed without difficulty. Moreover, when the fittings were connected and tested with water it had to be leak free before the fabrication steps were considered finalized. If any of the before mentioned qualities failed, the slicing software was used to make small changes in the print settings until a high-quality object was obtained.

The modified fluidic devices (Figure 3.7, route B) were made similarly to the flangeless fittings, however, an existing STL file from literature [4] was imported into Fusion 360 and adjusted to have threaded access ports instead of spaces for in-printed screw nuts. The process proceeded similarly as discussed above, however, a Creality CR20 Pro 3D-printer was used to fabricate these devices.

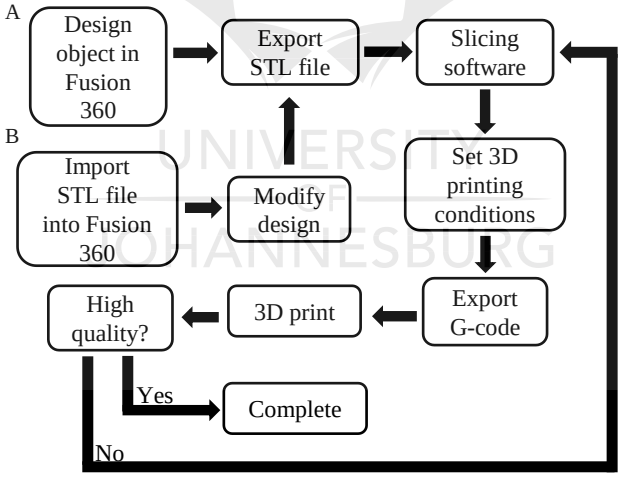

Figure 3.7: *A flow diagram of the design and modification steps followed in the manufacturing of all flow system components. (A) Flangeless fittings. (B) Modified reactors.*

The optimized printing conditions for the flangeless fittings made from PLA included a bed temperature of 60 °C and extruder temperature of 195 °C. A 0.4 mm nozzle was used together with a layer height of 0.15 mm. A 100% infill and 105% extruder flow were used. No supports were required. Mixers and unions had to be scaled by 5% in order to ensure a good fit with the

adapters and flangeless nuts. This was due to the hardness of the filament which caused too much friction in order to insert parts properly. This scaling up in size could lead to leaks in the flow system, especially when the backpressure is high. A lubricant with some scaling up (between 3 and 4 percent) can be considered, however this raises contamination concerns. Based on this, fittings printed in PLA were not pursued.

The optimized PP printing conditions included a bed temperature of 80 °C, which was increased to 85 °C for larger objects to minimize warping. Using an infill of 100% guaranteed a watertight object, whereas an extruder flow of 105% provided the necessary tightness of channels [9]. A 0.4 mm diameter nozzle and a layer height of 0.15 mm was used for both printers. No support structures were required except for a brim that was added to larger objects to improve printer bed adhesion and minimize warping. Furthermore, all components were printed on top of a layer of packing tape for strong bed adhesion. The extruder was initially set to 240 °C and systematically reduced to 233 °C in cases where stringing was observed. This was a crucial step in optimizing the threaded components printed in PP, since considerable stringing in printed threaded access ports are troublesome to remove without damaging the threading. In the presence of stringing it becomes difficult to connect threaded male and female components. Stringing was also the main cause of blocked channels in the flow reactors. The printing speed played a crucial role in the quality of the final object; in general, smaller components were printed with slower overall printing speeds. The CSTRs were paused during printing at 46% to insert a 10 mm × 3.0 mm magnetic stirrer bar.

Digital models of the ferrules in the flangeless fittings kit were created, however, it was challenging to fabricate due to its small size. Resin-based printers such as SLA can be considered for its higher resolution printing capabilities, but the photopolymer materials typically used show poor resistivity to common organic solvents [4,9]. Based on this, commercial flangeless ferrules were used in the flow system presented here. The 3D-printed flangeless nuts are compatible with both types of commercial flangeless ferrules (i.e., 1/16” and 1/8”), thus giving versatility in tubing size.

3.3. Transesterification

3.3.1. Chemicals

Sunflower seed oil from *Helianthus annuus* (tested according to The European Pharmacopoeia, Ph. Eur.) were purchased from Merck and other commercial edible oils, namely avocado oil, canola oil, extra virgin olive oil, sunflower seed oil as well as a blend of canola and olive oil were bought from a local supermarket. Analytical standards of fatty acid methyl esters (FAMEs), namely methyl palmitate (C16:0 FAME, ≥99.0%), methyl stearate (C18:0 FAME, ≥99.0%), methyl oleate (C18:1*cis* FAME, ≥99.0%), methyl linoleate (C18:2 FAME, ≥98%) and methyl linolenate (C18:3 FAME, ≥98.5%) were purchased from Merck. Additionally, methyl nonanoate (C9:0 FAME, ≥99.8%, 1-tetradecene (≥99.8%) (C14 alkene or 14:1 hydrocarbon (HC)), glycerol tridodecanoate (trilaurin, ≥99%), 1,4-dioxane (≥99%), sodium citrate dihydrate (≥99%), sodium methoxide solution (25 wt.% in methanol), heptane (99%), potassium carbonate (99%), and methanol (≥99.9%) were purchased from Merck. All chemicals and reagents were used as received.

3.3.2. Solutions

The following sodium methoxide in methanol solutions were prepared: 5 wt.% (1 mL 25 wt.% in 4 mL solvent), 1 wt.% (0.5 mL 25 wt.% in 12 mL solvent), 0.84 wt.% (0.5 mL 5 wt.% in 2.5 mL solvent), and 0.084 wt.% (1 mL 0.84 wt.% in 9 mL solvent). A solution containing trilaurin, C9:0 FAME, and 1-tertadecene (1 mg each) in 1 mL 1,4-dioxane was prepared. For each of the oils investigated, 500 mg oil was dissolved in 50 mL of the previous solution. Furthermore, 15 g sodium citrate was dissolved in 100 mL water.

An additional three solutions were prepared: A 1.26 mol% (7.45 wt.%) potassium carbonate (K_2CO_3) solution was prepared by dissolving 4.01 g K_2CO_3 in 25 mL methanol and 30 mL water. A 2 mol% (11.12 wt.%) K_2CO_3 solution was prepared by dissolving 2.26 g K_2CO_3 in 10 mL methanol and 10 mL water. Similarly, 3.43 g K_2CO_3 was dissolved in 10 mL methanol and 10 mL water to give a 3 mol% (16.07 wt.%) solution.

3.3.3. Flow system configuration and operation

Four 3D-printed Poseidon syringe pumps [1] were used to carry out the flow reactions for the transesterification of triacylglycerols in edible oils. Two sets of syringe pumps were used simultaneously where all pumps were controlled using one personal computer and two controller programs (one program for each syringe pump set). The configuration of the flow system is depicted in Figure 3.8. All fittings and reactors were 3D-printed and used together with commercial Luer slip syringes, TFE tubing, and flangeless ferrules.

Four 10 mL syringes were filled with the 1,4-dioxane solution containing the edible oil and internal standards, the sodium methoxide in methanol solution, heptane, and the sodium citrate in water solution (without air entrapment) and were placed onto the syringe pumps in the order depicted in Figure 3.8. All flow reactions were carried out at room temperature with rapid stirring facilitated by magnetic stirrers. The optimized flow rate for the oil-dioxane and sodium methoxide solutions was 3.00 mL/hr. The heptane and sodium citrate solutions were introduced at 12.00 mL/hr and 9.00 mL/hr, respectively. For each of the oils, the transesterification reaction was performed in triplicate in flow where three fractions were collected at 5-minute intervals for each replicate, followed by GC analysis. The three samples collected every five minutes for each experiment were used to evaluate the stability of the flow system over time.

The first CSTR (Figure 3.8C) was used to mix the oil-dioxane mixture with the sodium methoxide solution. The sodium methoxide acts as the base-catalyst, while the 1,4-dioxane acts as a mediator solvent that creates a single-phase system. Heptane was added to the second CSTR (Figure 3.8E) for the extraction of the FAMEs. Again, the single-phase system was maintained by mixing. Upon addition of an aqueous sodium citrate solution, the reaction was quenched (Figure 3.8G), and the organic and aqueous phases separated in the sample collection vial (Figure 3.8H). The top layer (organic phase) was transferred to a GC vial for further analysis.

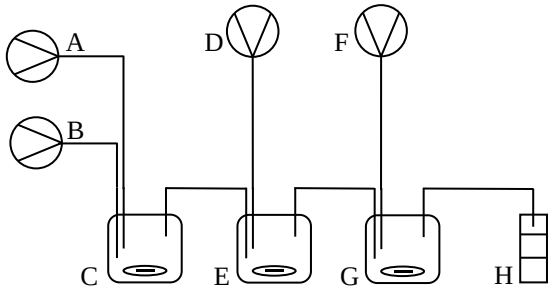

Figure 3.8: *Schematic diagram of the flow system used for the transesterification of triacylglycerols in edible oils using a base-catalyzed method at ambient temperature. All three CSTRs contained a stirrer bar and was rapidly stirred using magnetic stirrers. (A) Dioxane containing the oil and internal standards. (B) Sodium methoxide. (C) CSTR 1. (D) Heptane. (E) CSTR 2. (F) Sodium citrate. (G) CSTR 3. (H) Sample collection.*

3.3.4. Gas chromatographic analysis

All collected fractions were analyzed with a Perkin Elmer Clarus 580 gas chromatograph using a Supelcowax® 10 capillary column (30 m × 250 μm × 0.25 μm). A 1.00 μL sample was injected and the inlet temperature was 250 °C. Helium was used as the carrier gas with a flow rate of 1.00 mL/min and a split ratio of 20:1. The GC oven temperature was set to first reach 180 °C at 25 °C/min from 40 °C, followed by an increase in oven temperature to 250 °C at 15 °C/min with a 3-minute hold. The oven equilibration time was extended to 120 s to minimize peak shifts between runs. The FID was set to 300 °C. The identity of chromatographic peaks were confirmed by comparison with retention times of standards.

3.3.5. Transesterification reactions

Three internal standards were incorporated into the flow reaction. According to literature, the ratio of the C9:0 FAME peak area relative to the C14 alkene peak area indicates that saponification has occurred if it is less than 0.67. In addition, if the C12:0 FAME (originating from trilaurin) to C14 alkene peak area ratio is less than 0.75, transesterification was incomplete, or saponification has already occurred [10,11]. These ratios were used to optimize

the flow reaction conditions to ensure that the transesterification reaction was complete, but at the same time to ensure that the reaction was terminated before saponification could occur. These initial optimization reactions were carried out using the certified sunflower oil.

Various catalyst concentrations were considered. Initially, a 5 wt.% solution of sodium methoxide [10,11] was used and lower concentrations (1, 0.84, and 0.084 wt.%) were also considered. Based on preliminary results, the 1 wt.% solution was used in further experiments. Potassium carbonate (1.26, 2, and 3 mol%) was also investigated as a potential base-catalyst, however these experiments were unsuccessful.

The flow reactions were also compared to reactions performed in batch. Batch reactions were performed based on a previously reported method by Suter et al. [10], but the catalyst concentration was reduced to 1 wt.% in order to compare results with those obtained from flow reactions. Batch reactions were performed by transferring 100 μL each of the dioxane solution (including the oil and the internal standards) and the sodium methoxide solution in a 2 mL vial. The mixture was vortexed for 10 seconds and allowed to stand for 60 seconds. 1 mL heptane was added and vortexed for 10 seconds, followed by the addition of 300 μL of the sodium citrate solution. The solution was vortexed for 10 seconds, and complete phase separation was observed within 60 seconds. The organic phase was then transferred to a GC vial for further analysis.

For each of the analyzed edible oils, the relative peak area of each FAME was determined as a percentage of the sum of the areas of all FAME peaks. Solvent peaks, internal standard peaks, and peaks with an area < 0.05% were excluded from this calculation. This approach is in line with Ph. Eur. guidelines.

3.4. References

[1] A.S. Booeshaghi, E.d.V. Beltrame, D. Bannon, J. Gehring, L. Pachter, Principles of open source bioinstrumentation applied to the poseidon syringe pump system, Scientific Reports. 9 (2019) 1–8. https://doi.org/10.1038/s41598-019-48815-9.

[2] B. Wijnen, E.J. Hunt, G.C. Anzalone, J.M. Pearce, Open-source syringe pump library, PLoS ONE. 9 (2014). https://doi.org/10.1371/journal.pone.0107216.

[3] E. Batista, N. Almeida, E. Filipe, A. Costa, Calibration and use of syringe pumps, 16 Th International Congress of Metrology, EDP Sciences. 02007 (2013). https://doi.org/10.1051/metrology/201302007.

[4] J.M. Neumaier, A. Madani, T. Klein, T. Ziegler, Low-budget 3D-printed equipment for continuous flow reactions, Beilstein Journal of Organic Chemistry. 15 (2019) 558–566. https://doi.org/10.3762/bjoc.15.50.

[5] V. Dragone, V. Sans, M.H. Rosnes, P.J. Kitson, L. Cronin, 3D-printed devices for continuous-flow organic chemistry, Beilstein Journal of Organic Chemistry. 9 (2013) 951–959. https://doi.org/10.3762/bjoc.9.109.

[6] G.W. Bishop, J.E. Satterwhite, S. Bhakta, K. Kadimisetty, K.M. Gillette, E. Chen, J.F. Rusling, 3D-Printed fluidic devices for nanoparticle preparation and flow-injection amperometry using integrated prussian blue nanoparticle-modified electrodes, Analytical Chemistry. 87 (2015) 5437–5443. https://doi.org/10.1021/acs.analchem.5b00903.

[7] T. Tabassum, M. Iloska, D. Scuereb, N. Taira, C. Jin, V. Zaitsev, F. Afshar, T. Kim, Development and Application of 3D Printed Mesoreactors in Chemical Engineering Education, Journal of Chemical Education. 95 (2018) 783–790. https://doi.org/10.1021/acs.jchemed.7b00663.

[8] V. Romanov, R. Samuel, M. Chaharlang, A.R. Jafek, A. Frost, B.K. Gale, FDM 3D Printing of High-Pressure, Heat-Resistant, Transparent Microfluidic Devices, Analytical Chemistry. 90 (2018) 10450–10456. https://doi.org/10.1021/acs.analchem.8b02356.

[9] Z.X. Rao, B. Patel, A. Monaco, Z.J. Cao, M. Barniol-Xicota, E. Pichon, M. Ladlow, S.T. Hilton, 3D-Printed Polypropylene Continuous-Flow Column Reactors: Exploration of Reactor Utility in S_NAr Reactions and the Synthesis of Bicyclic and Tetracyclic Heterocycles, European

Journal of Organic Chemistry. 2017 (2017) 6499–6504. https://doi.org/10.1002/ejoc.201701111.

[10] B. Suter, K. Grob, B. Pacciarelli, Determination of fat content and fatty acid composition through 1-min transesterification in the food sample; principles, Z Lebensm Unters Forsch A. 204 (1997) 252–258. https://doi.org/https://doi.org/10.1007/s002170050073.

[11] B. Schilling, R. Bolliger, G. Boehm, Automated Workflow for the Transesterification of Fatty Acid Methyl Esters (FAME) in Fat and Fat Containing Food Samples Using a 90 Sec. Transesterification, https://www.palsystem.com/fileadmin/public/docs/Downloads/Posters/Automated_Generation___Analysis_of_FAME_GC_ISCC_Riva_2014_Poster.pdf (accessed September 30, 2020).

Chapter 4: Results and discussions

4.1. Poseidon syringe pump system

4.1.1. Cost analysis

The low-cost Poseidon syringe pump system was 3D-printed and assembled according to the original design, as reported by Booeshaghi et al. [1]. In total, the costs involved for the system with three syringe pumps was less than ZAR 2212.81 (<USD 155) (see Appendix B, Table B1). It was reported that the total costs involved to recreate their design was USD 400 (see Chapter 2, Section 2.4.1). Since the microscope system and the Raspberry Pi was excluded in this work, the costs were lower.

The Poseidon syringe pump system recreated in this work was slightly more expensive in comparison to the syringe pumps developed by Wijnen et al. [2], Cubberly et al. [3], and Lake et al. [4]. Their reported costs were approximately USD 100 (see Chapter 2, Section 2.4.1). However, these open-source syringe pump sets were limited to one or two syringe pumps in a set, whereas the Poseidon syringe pump system included three syringe pumps in total. Therefore, it was slightly more expensive because more commercial hardware was required to complete the system. Similarly, the Poseidon syringe pump set was less expensive in comparison to those created by Neumaier et al. [5] (USD 360), because their system included four syringe pumps with a standalone operating device.

4.1.2. Flow rate validation

The relationship between the programmed and observed flow rates for 1 mL (Figure 4.1A), 5 mL (Figure 4.1B), and 10 mL (Figure 4.1C) syringes are shown in Figure 4.1. The raw data are provided in Appendix B (Table B2 and B3). The flow rate was set to millilitre per hour (mL/hr) in the controller program. Coincidently, the coefficient of determination (R^2) values were all equal to 0.9998 (Figure 4.1A to 4.1C). From these linear relationships and coefficient of

determination (R^2 = 0.9998) values it is evident that the observed flow rates were in agreement with the programmed flow rates for each syringe size used.

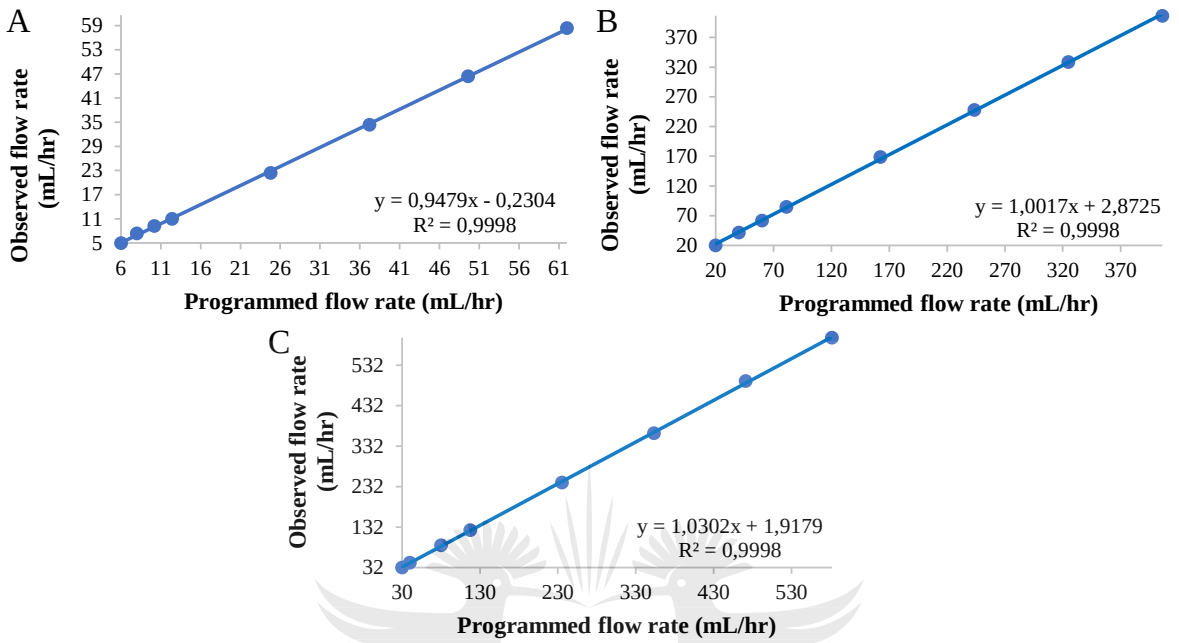

Figure 4.1: *Calibration curves using a (A) 1 mL syringe, (B) 5 mL syringe, and (C) 10 mL syringe. The flow rate was set to millilitre per hour (mL/hr) in the Poseidon operating program.*

Similarly as above, linear relationships were obtained between the programmed flow rate and the observed flow rate using a flow rate unit of millimetre per second (mm/s) in the Poseidon operating program. The obtained results were converted by a simple calculation to millimetre per minute (mm/min) for convenience. For 1 mL and 10 mL syringes, R^2 values of 0.9997 (Figure 4.2A) and 0.9998 (Figure 4.2C) were obtained respectively, whereas for a 5 mL syringe a slightly lower R^2 value of 0.9990 (Figure 4.2B) was obtained. These results (Figure 4.1 and 4.2) indicate that the open-source syringe pumps built in-house can produce sufficiently accurate programmed flow rates for flow chemistry purposes.

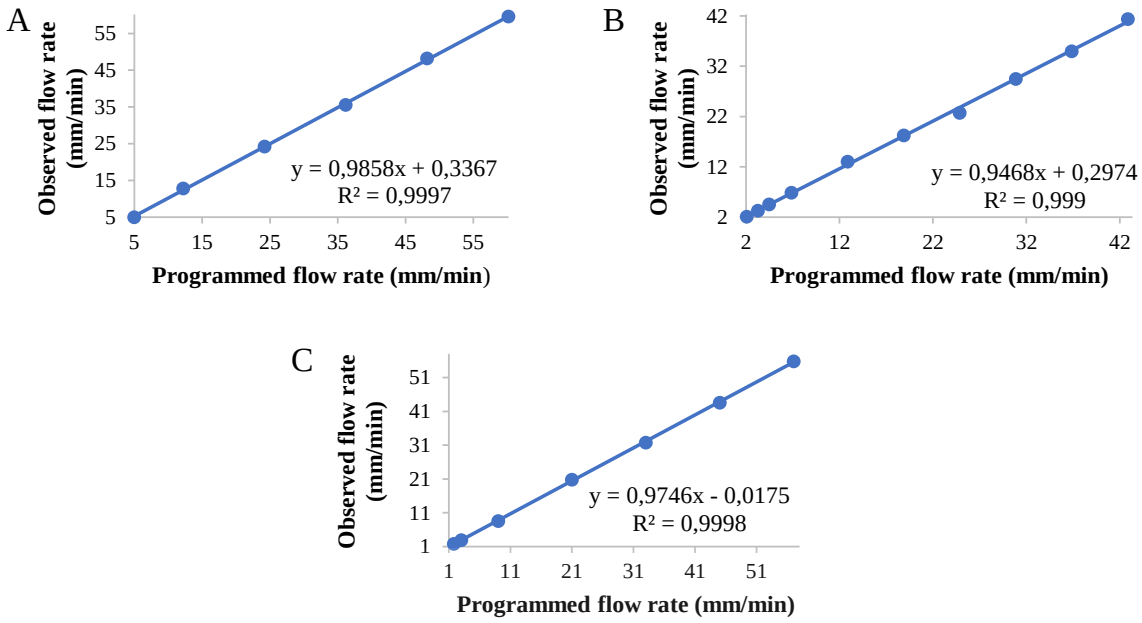

Figure 4.2: *Calibration curves using a (A) 1 mL syringe, (B) 5 mL syringe, and (C) 10 mL syringe. Experimentally the flow rate was set to millimetre per second (mm/s), but the results were converted to millimetre per minute (mm/min) for convenience.*

4.1.3. Analysis of variance (ANOVA)

For single factor ANOVA, the null hypothesis (H_0) and the alternative hypothesis (H_a) were defined as follows: H_0 in this case was that the mean values of the observed flow rates (at a specific programmed flow rate) for all three pumps were equal, and the H_a was that at least two flow rate means were different. The H_0 will be rejected if the value for test statistic (F) is greater than the critical value of F (F_{crit} = 3.89) at a 95% confidence level for two and twelve degrees of freedom (df) for the source of variation between groups and within groups, respectively.

The data obtained for the observed flow rates of each pump in the syringe pump set for a specific programmed flow rate are summarized in Table 4.1. The calculated F-values are also reported in Table 4.1. Since the F-value for each of the programmed flow rates was less than the critical value (F_{crit} = 3.89) at a 95% confidence level, the null hypothesis is accepted. Thus, there is no statistically significant difference between the average observed flow rates for all

three syringe pumps when each was programmed to operate at 3.00, 6.00, and 9.00 mL/hr, respectively.

Table 4.1: *Comparison of individual pump performance. Various flow rates were measured using 5 mL syringes.*

Programmed flow rate (mL/hr)	**Observed flow rate (mL/hr)**			**Test statistic (*F*-values)**
	Pump 1	**Pump 2**	**Pump 3**	
3.00	2.64	2.64	2.70	0.10
	3.00	3.06	2.88	
	3.06	3.06	2.82	
	3.00	2.94	3.06	
	2.94	3.06	3.06	
6.00	5.64	5.82	5.82	2.11
	6.12	5.94	6.54	
	5.88	5.88	6.00	
	6.12	4.86	6.00	
	6.06	6.06	6.54	
9.00	9.30	9.30	9.24	1.94
	9.54	9.06	9.24	
	9.18	9.24	9.42	
	8.94	9.00	9.36	
	9.48	8.94	9.24	

4.2. 3D-printed flow components

4.2.1. Flangeless fittings kit

To illustrate the versatility and cost-saving capability of 3D-printing technology, a flangeless fittings kit was designed and fabricated using PP as printing material. The flangeless fittings kit consists of syringe adapters, flangeless nuts, male Luers, unions and mixers (T-mixers and crosses) for use in continuous flow systems. Commercial flangeless ferrules (1/16” and 1/8”), syringes and tubing complete a simple assembly (Figure 4.3). Print settings and object orientation are crucial to obtain leak-free fluidic devices with well-defined channels. The

components were orientated so that the threaded parts were printed vertically (along the z-axis). In line with previous studies [6], this resulted in higher quality fittings.

Originally, the flangeless fittings kit was fabricated using the Prusa i3 MK3S 3D-printer, however the kit was found to be reproducible using the Creality CR20 Pro 3D-printer. Print settings can be found in the appendix for both 3D-printers used in this work (see Appendix C, Table C3 and C4). Two types of unions and T-mixers were designed. For example, a union consisted of either a vertical design with access ports placed at the top and bottom of the device (see Chapter 3, Figure 3.3F) or the access ports were orientated next to each other (Figure 3.3 C and Figure 4.3C). Similarly, T-mixers could have two access ports placed at the top and one at the bottom (see Chapter 3, Figure 3.3E) or three access ports placed next to each other (Figure 4.3B). Some design modifications for these components were necessary when using the Creality CR 20 Pro 3D-printer because significant shrinkage was observed at the threaded parts printed closest to the printer bed. At first, print settings were fine-tuned, however the problem could not be resolved which consequently led to it being redesigned as described above. All components were found to work equally well when inspected after fabrication.

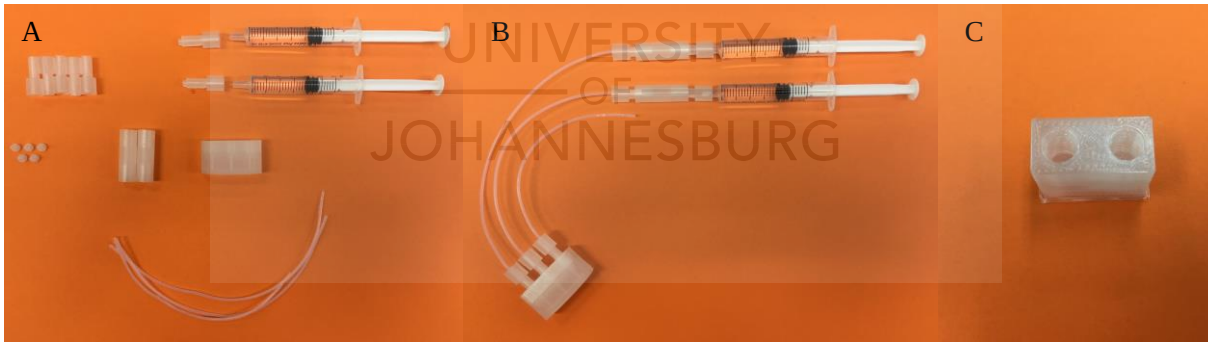

Figure 4.3: *The 3D-printed PP flangeless fittings kit where commercial flangeless ferrules, syringes and tubing complete a simple assembly. (A) The unassembled 3D-printed PP flangeless fittings kit. (B) Assembled 3D-printed PP flangeless fittings kit. (C) 3D-printed PP alternative union.*

The 1/4”-28 UNF fittings and connectors manufactured in-house were fully compatible with the commercial kit. This compatibility leads to a significant advantage because damaged or

misplaced pieces can be easily replaced at low cost, or the complete self-manufactured kit can be used on its own. The commercial flangeless fittings kit had two kinds of flangeless nuts, one that is compatible with a 1/16” flangeless ferrule and another that is compatible with a 1/8” flangeless ferrule. The difference between the two nuts were the design of the voids inside the threaded parts of the nuts. The 1/8” flangeless nut had a cylindrical shaped void while the other (1/16” flangeless nut) had a countersunk hole designed to hold a 1/16” flangeless ferrule in place. Coincidentally, it was observed that the 3D-printed nuts formed a leak-tight seal with both flangeless ferrule sizes. It is important to remember that a flangeless nut only secures a ferrule in a threaded access port. The flangeless ferrule forms the leak-tight seal from a reactor to tubing [7]. Thus, the 3D-printed cylindrical voids (4.4 mm diameter) in the threaded parts of the flangeless nuts were large enough to hold both flangeless ferrule sizes in place. This observation led to an additional advantage because one type of 3D-printed nut can accommodate connections to both tubing sizes (1/16” and 1/8” OD).

Furthermore, Figure 4.4 shows that threaded parts were not significantly altered after being used in a flow system. Only minor damage was observed at the end of the threading (Figure 4.4B). The PP fittings were reused several times during the course of this study without any problems, but it is important to note that they do not have an infinite lifespan. These fittings were also printed using PLA (see Appendix C, Figure C1 and C2) but have limited use in flow reactions since they are not compatible with most organic solvents.

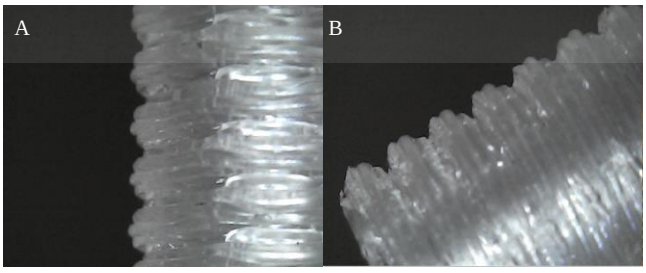

Figure 4.4: *Threaded parts of a 3D-printed PP flangeless nut (A) before and (B) after use in a flow system.*

At the time this research was conducted, the commercial flangeless fittings kit cost ZAR 6790.75 (<USD 500). The RS Pro PP filament cost ZAR 602.32 (<USD 45) for 500 g. The

open-source PrusaSlic3r program can be used to estimate the printing time, the amount of filament used as well as the associated cost per object. It was estimated that fabricating the entire flangeless fittings kit using PP filament would cost ZAR 66.63 (<USD 5) and take approximately 1315 minutes (21.92 hours) to produce, as indicated in Table 4.2. To complete the kit, the cost of 42 commercial flangeless ferrules need to be accounted for. The commercial kit had 42 commercial flangeless ferrules, half of which are of size 1/8" and the remaining half 1/16". However, it should be noted that flangeless ferrules can only be purchased in packs of ten for both sizes. Thus, two packs of each size will cost approximately ZAR 1416.80 (<USD 100). Therefore, to reproduce the complete kit utilizing 3D-printing and purchasing commercial ferrules would cost approximately ZAR 1483.43 (<USD 105). Consequently, approximately 78% of research funds can be saved when utilizing 3D-printing for the self-manufacturing of the PP flangeless fittings kit.

Table 4.2: *The estimated printing time per object and related cost per amount PP filament used. The number of pieces per kit is similar to that of the commercial Flangeless fittings kit (Upchurch) model 1454. The flangeless nuts were designed as one size that is compatible with both 1/16" and 1/8" flangeless ferrules.*

Part	Time per piece (min)	Amount of filament per piece (g)	Cost per piece (ZAR)	Amount per kit	Total cost (ZAR)
Flangeless nut	14	0.26	0.76	42	31.92
Standard union (1/4"-28)	34	2.22	1.34	6	8.04
Metric adapter (M6)	35	2.3	1.38	2	2.76
Metric adapter (1/4"-28, M6)	35	2.24	1.35	2	2.7
Syringe adapter (converted female Luer)	16	0.93	0.56	2	1.12
Male Luer	15	0.7	0.42	2	0.84
T-mixer (1.5 mm channel)	80	8.18	4.92	1	4.92
T-mixer (2 mm channel)	78	8.12	4.89	1	4.89
Cross (1.5 mm channel)	83	7.87	4.74	1	4.74
Cross (2 mm channel)	80	7.81	4.7	1	4.7
Total (ZAR)	**470**	**40.63**	**25.06**	**60**	**66.63**

A similar kit was recently produced by Price et al. [6], where a multimaterial 3D-printer was used to make standard fittings: wetted parts (those in contact with solutions) were made from PP. In contrast, non-wetted parts (specifically threaded parts) were made from PLA. The reason for their approach was based on the physical properties of PP (e.g., low flexural modulus), suggesting that it could potentially lead to leaks in a flow system [6]. However, in the work presented here, leak-tight fittings, unions, and mixers were produced with PP by carefully fine-tuning print settings. Although printing with PP is more complicated and troubleshooting can sometimes be time consuming, the advantage is that a multimaterial 3D printer is not required to manufacture the components needed to build a flow system.

4.2.2. Modified fluidic devices

The flow system components were completed by 3D-printing the modified fluidic devices using clear PP as printing material. Leak-proof CSTRs were 3D-printed using the Creality CR20 Pro 3D-printer, however it was found that the chip reactor was more challenging to 3D-print successfully even though print settings were carefully fine-tuned. A high-quality chip reactor was successfully 3D-printed using the Prusa i3 MK3S 3D-printer. All reactors were 3D-printed with access ports orientated vertically (along the z-axis) with brim support structures to avoid warping and improve printer bed adhesion.

The tank and the channels of the CSTRs were not visible from above (Figure 4.5A and 4.5B), however the bottom of the tanks were visible from below because the bottom layer of the devices were approximately 3 mm in thickness. Therefore, the stirrer bars placed inside the tanks could be seen when viewing the CSTR from below. The volume of the tank was determined by 3D-printing 50% of one CSTR in PP. The stirrer bar was placed inside the tank and was filled with water until it reached the highest positioned channel. The mass of the CSTR (containing the stirrer bar) was measured before and after being filled with water. It was determined that the volume of the tank (incl. stirrer bar) was approximately 0.38 mL.

The channels of the chip reactor (Figure 4.5C) could be visually monitored because the reaction zone of the device was fully transparent. Thus, reactions, bubbles, and channel blockages (caused by solid formation) could be visually monitored.

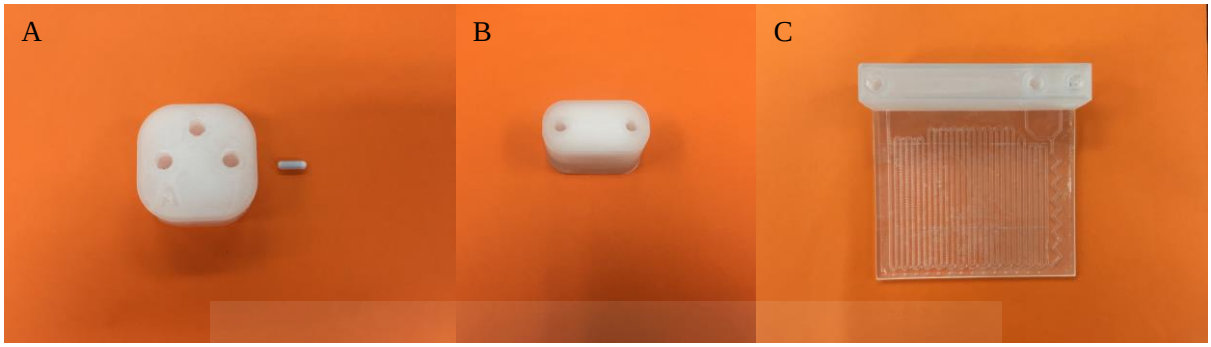

Figure 4.5: *3D-printed PP flow reactors. (A) Three access port CSTR with an identical magnetic stirrer bar (right) that was placed inside the tank during the 3D-printing process by pausing the printer. (B) Two access port CSTR. (C) Chip reactor with a total of three access ports (two inlets and a single outlet).*

In general, it was found that similar print settings can be used for all fluidic device fabrication when using the Prusa i3 MK3S 3D-printer. However, when using the Creality CR20 Pro 3D-printer, printing speeds played a crucial role in successful fluidic device fabrication. Faster printing speeds was preferred for larger devices and slower printing speeds for smaller devices. Gaps in the first layer or infill layers surpassing the outline (walls) of the 3D-printed device were examples of printing speeds set too fast. If any of the beforementioned printing errors occurred, the printing speed was systematically reduced in increments of 5 mm/s until the problem was resolved.

4.3. Transesterification

4.3.1. Flow system assembly and operation

The optimized flow system was set up according to the diagram in Figure 3.8 and is shown in Figure 4.6A with arrows indicating the flow direction (Figure 4.6B). The 3D-printed syringe

pumps further contribute to lowering the overall cost of the flow system. All fittings and unions were 3D-printed in PP and were used similarly to commercial fittings. This system is considered to be semi-automated because the fractions are collected and manually transferred to a GC vial, but the actual chemical reaction (in flow) is fully automated. The minimal manual intervention required provides the advantage of minimizing personal errors and potentially improving precision. This methodology is considered safer compared to a batch protocol because limited handling of chemicals was required. Besides, a lower catalyst concentration could be used due to the increased reactivity observed in flow. Furthermore, throughput was increased by 3D-printing multiple CSTRs that can be used as replacements for those used in a previous reaction. This was useful when multiple reactions were carried out in a single day, since cleaning each reactor (incl. tubing and connectors) and drying all components can be time consuming. The transesterification method presented here is more efficient compared to a previous version [8], since there is no pause and subsequent waiting period required to achieve complete transesterification.

Figure 4.6: *Set-up of the semi-automated 3D-printed flow system of the transesterification of edible oils. (A) A complete view of the flow system from above, consisting of the Poseidon syringe pump system, three CSTRs placed in series, and a sample collection zone. (B) A side view of the flow system where the arrows indicate the flow direction of the reagents and subsequent products. The downward pointing arrows shows the movement of fluid into the CSTRs originating from either the syringe pumps or the previous CSTR. The upward pointing arrows represent the movement of fluid exiting the CSTRs.*

4.3.2. Optimization of flow reaction parameters

To optimize parameters, the reaction mixtures were analyzed with GC-FID. The ratios of internal standards were used to determine whether the transesterification was complete, and whether saponification occurred (see Chapter 3, Section 3.3.5). The chip reactor (Figure 4.5C) was initially used instead of CSTR 1 (Figure 4.6A) where a 5 wt.% sodium methoxide solution was used as a base-catalyst. However, complete blocking of the channels due to solid formation occurred before heptane and sodium citrate could be introduced into the system, thus preventing the collection of samples for analysis. As a consequence, the chip reactor was replaced with CSTR 1.

With three CSTRs placed in a linear configuration (see Chapter 2, Figure 2.4A), a variety of preliminary experiments were carried out in flow mode where the flow rates were set to 6.00 mL/hr for all reagents (Table 4.3, Reactions 1 to 4). First, 5 wt.% sodium methoxide was used as a base-catalyst (Table 4.3, Reaction 1). However, within 5 minutes the tubing and the tanks were clogged with white solids. Leaks at the connections were observed that were caused by the constant increase in backpressure as the amount of solids in the tubing and tanks increased until the outlet was completely blocked. Analysis confirmed saponification occurred by obtaining peak area ratios (C9:0 FAME/C14 alkene and C12:0 FAME/C14 alkene) of 0.64 [9,10]. Schuchardt et al. [11] indicated that 0.5 mol% (equivalent to 0.84 wt.%) sodium methoxide may be sufficient to carry out transesterification reactions. Therefore, a 0.84 wt.% sodium methoxide was investigated. Similarly as with the 5 wt.% sodium methoxide, solid formation occurred within 5 minutes and saponification was confirmed with C9:0 FAME/C14 alkene and C12:0 FAME/C14 alkene peak area ratios of 0.60 and 0.38, respectively (Table 4.3, Reaction 2). In order to avoid the formation of solids, the sodium methoxide concentration was further reduced to 0.084 wt.%. No solid formation was observed for the 5- and 10-minute fractions. However, the transesterification reactions were incomplete for all fractions, because the C9:0 FAME/C14 alkene and C12:0 FAME/C14 alkene peak area ratios were above 0.67 and below 0.75 [9,10], respectively (Table 4.3, Reaction 3).

Schuchardt et al. [11] reported that 2 and 3 mol% (equivalent to 11.12 and 16.07 wt.%) potassium carbonate can be considered good base-catalysts because it gives high yields of fatty

acid alkyl esters. It also reduces the formation of soap (i.e., saponification) because bicarbonate is formed instead of water [11]. A 1.26 mol% (equivalent to 7.45 wt.%) solution of potassium carbonate was used as a base-catalyst in flow mode (Table 4.3, Reaction 4). Even though no solids were observed, the experiments were unsuccessful because the transesterification reactions were incomplete as indicated by the values obtained for the peak area ratios of the C9:0 FAME/C14 alkene (1.50 and 2.83) and the C12:0 FAME/C14 alkene (0.1 for both fractions). The potassium carbonate concentration was increased to 2 and 3 mol% and a quick batch mode protocol was caried out, however similar results were obtained (Table 4.3, Reactions 5 to 6) as in the flow mode protocol (Table 4.3, Reaction 4). It is possible that an increase in temperature could drive the reactions to completion, however PP interacts with heptane at 30 °C [12]. Therefore, an increase in temperature should rather be avoided in order to preserve the structural integrity of the 3D-printed flow components. For these reasons, using potassium carbonate as a base-catalyst for the transesterification of edible oils was decided to be unfeasible. Consequently, sodium methoxide was chosen as the best base-catalyst since reactions can be carried out at ambient temperature.

Table 4.3: *Preliminary results summary. Base-catalysts and concentrations were varied. Reactions were primarily carried out in flow mode, however two reactions were tested using a batch mode protocol.*

Reaction	Base-catalyst	Method	Fraction (min)	C9:0 FAME/C14 alkene ratio	C12:0 FAME/C14 alkene ratio
1	5 wt.% $NaOCH_3$	Flow	5	0.64[a]	0.64[a]
2	0.84 wt.% $NaOCH_3$	Flow	5	0.60[a]	0.38[a]
3	0.084 wt.% $NaOCH_3$	Flow	5	0.99	0.15[b]
			10	1.09	0.13[b]
4	7.45 wt.% K_2CO_3	Flow	5	1.50	0.01[b]
			10	2.83	0.01[b]
5	11.12 wt.% K_2CO_3	Batch	-	0.70	0.01[b]
6	16.07 wt.% K_2CO_3	Batch	-	0.72	0.01[b]

[a] *Saponification.* [b] *Incomplete transesterification.*

By revisiting the amount of the reagents present after each sequential step in a batch mode protocol (see Chapter 3, Section 3.3.5), it was realised that there was not enough quenching agent present in the tanks of the CSTRs when flow rates of 6.00 mL/hr were used for each reagent in order to stop the reaction before the occurrence of saponification. This was considered to be the main reason why solid formation was problematic when 5 and 0.84 wt.% sodium methoxide was used (Table 4.3, Reactions 1 and 2).

Translating the amounts of reagents used in a batch mode protocol while considering the basic principles of flow chemistry, specifically relating to the flow rates of fluids entering and exiting a reactor (see Chapter 2, Section 2.1), the following flow rates were calculated as follows: Equal amounts of the edible oil (incl. internal standards) in 1,4-dioxane solution and the sodium methoxide solution are required to facilitate transesterification (i.e., 1:1 ratio). Thus, a flow rate of 3.00 mL/hr was chosen for each of these solutions. The resulting flow rate of the fluid exiting CSTR 1 is 6.00 mL/hr. The ratio of oil in 1,4-dioxane and sodium methoxide to the sodium citrate solution was calculated to be 2:3. Therefore a flow rate of 9.00 mL/hr was calculated to be sufficient to quench the reaction in order to prevent saponification (i.e., solid formation). The ratio of oil in 1,4-dioxane and sodium methoxide to heptane was 1:5. This translates to a flow rate of 30.00 mL/hr, which is too fast and would certainly increase the backpressure of the system. Considering the fact that low-pressure 3D-printed fittings were used and that it is well known that less solvent is required when carrying out reactions in flow [13], the flow rate of heptane was chosen to be 12.00 mL/hr which corresponds to a ratio of 1:2 instead of 1:5. The flow rate of the products leaving CSTR 3 was calculated to be 27.00 mL/hr.

Additional preliminary reactions were performed to determine if the adjusted flow rates solved the saponification or the incomplete transesterification challenges. From Table 4.4, the adjusted flow rates prevented the occurrence of saponification since all reactions had peak area ratios exceeding 0.67 for the C9:0 FAME/C14 alkene relationship (Table 4.4, Reaction 1 to 3) and no solid formation was observed in the tubing or the CSTR tanks.

The ideal catalyst concentration was also determined (Table 4.4). Initially a base-catalyst concentration of 5 wt.% was used, but the 0.84 wt.% was also considered as suggested by

Schuchardt et al. [11]. A 0.084 wt.% concentration was tested to determine if even lower concentrations of base would be suitable. No solid formation was observed in any of the reactions and based on the C9:0 FAME/C14 alkene ratios, no saponification occurred. However, complete transesterification was only observed for higher concentrations (Table 4.4, Reactions 1 to 2). Reaction 3 had very low C12:0 FAME/C14 alkene ratios, indicating that a sodium methoxide concentration of 0.084 wt.% (or 0.05 mol%) was too low to drive the reaction to completion. Since reactions 1 and 2 yielded similar results, 0.84 wt.% sodium methoxide was chosen as the best base-catalyst and reactions were repeated in triplicate on different days to evaluate its robustness and reliability.

Table 4.4: *A summary of the optimization process by varying the base-catalyst concentration.*

Reaction	Base-catalyst	Fraction (min)	C9:0 FAME/C14 alkene ratio	C12:0 FAME/C14 alkene ratio
1	5 wt.% $NaOCH_3$	5	0.72	0.79
		10	0.74	0.79
		15	0.74	0.80
2	0.84 wt.% $NaOCH_3$	5	0.70	0.77
		10	0.82	0.87
		15	0.69	0.78
3	0.084 wt.% $NaOCH_3$	5	0.71	0.14[a]
		10	0.74	0.12[a]
		15	0.75	0.11[a]

[a] *Incomplete transesterification.*

Replicate analysis using 0.84 wt.% sodium methoxide resulted in half of the fractions collected as incomplete transesterifications reactions for replicates 2 and 3 (Table 4.5). This observation was suspected to be caused by cooler and more humid weather conditions in comparison to the warmer and less humid conditions for the first replicate. Therefore, the base-catalyst concentration was increased to 1 wt.% and was found to be more robust and reliable with only the first reaction taking slightly longer to reach completion in comparison to the second and third replicates.

It is important to mention that the cylindrical stirrer bars tended to catch (or get stuck) against the walls of cylindrical tanks when stirring at high speeds. A similar observation was made by

Penny et al. [14], where their cylindrical stirrer bars got stuck in their 3D-printed mixing chips when a fast stirring speed was used. To ensure that the mixtures were continuously stirred without interruptions, the stirring had to be checked on a regular basis. If the stirrer bars were not rotating and hence not stirring the reaction mixtures, the CSTRs had to be gently tapped. If the stirring resumed, the experiments continued as normal. Penny et al. [14] reported that cross-shape stirrer bars had improved speed stability that led to perfect mixing and therefore these stirrer bars could be a solution to avoid this problem in future.

Table 4.5: *A summary of the triplicate analysis of the transesterification reactions using 0.84 wt.% and 1 wt.% sodium methoxide as base-catalysts.*

Base-catalyst	Replicate	Fraction (min)	FAME-9/C14 alkene ratio	FAME-12/C14 alkene ratio
0.84 wt.% $NaOCH_3$	1	5	0.70	0.77
		10	0.82	0.87
		15	0.69	0.78
	2	5	0.69	0.78
		10	0.76	0.74[a]
		15	0.76	0.75
	3	5	0.74	0.75
		10	0.77	0.72[a]
		15	0.77	0.74[a]
1 wt.% $NaOCH_3$	1	5	0.74	0.74[a]
		10	0.73	0.76
		15	0.72	0.77
	2	5	0.71	0.80
		10	0.72	0.78
		15	0.71	0.79
	3	5	0.74	0.77
		10	0.74	0.77
		15	0.73	0.78

[a] *Incomplete transesterification.*

4.3.3. Comparison of reactions in batch and flow

Results obtained for reactions in batch (1 and 5 wt.%) and flow (1 wt.%) are shown in Figure 4.7, where the peak area ratios of internal standards were used to evaluate the extent of transesterification and saponification. No saponification was observed for both batch and flow reactions because all C9:0 FAME/C14 alkene peak area ratios were above the saponification limit of 0.67. As expected, performing a batch mode protocol using a 5 wt.% base-catalyst concentration yielded complete transesterification peak area ratios (C12:0 FAME/C14 alkene ratio) of approximately 0.81 on average. However, the results indicate that the transesterification reactions performed in batch with 1 wt.% sodium methoxide were incomplete, based on the average C12:0 FAME/C14 alkene peak area ratio at 0.71 [9,10].

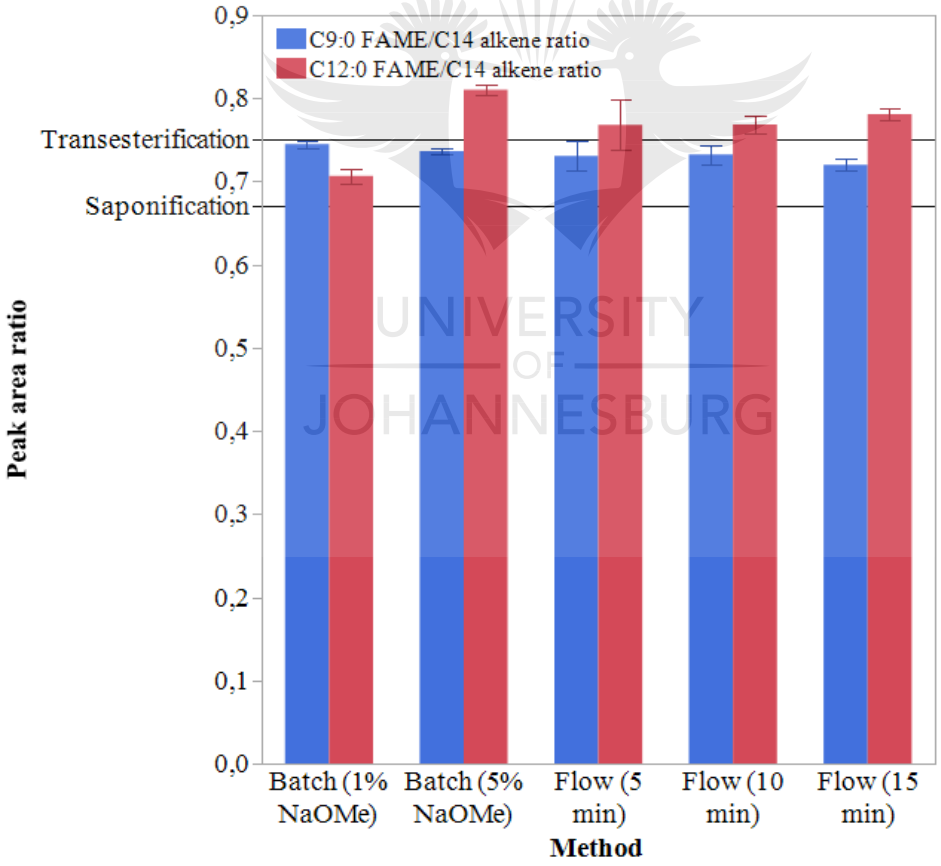

Figure 4.7: *A bar chart displaying the difference between the peak area ratios of the internal standards following a batch (1 and 5 wt.%) or flow mode (1 wt.%) protocol. All reactions were run in triplicate, the height of the bars represents the mean, and the error bars indicate the standard deviation.*

Notably, flow mode outperforms its batch counterpart by having all C12:0 FAME/C14 alkene peak area ratios above 0.75, indicating complete transesterification. This observation can be accounted for due to the reduced reaction time of flow reactions because of efficient mixing and accurate control over reaction parameters in small reactors, which enhances chemical selectivity and improve product yield [15]. There is some variability in the C12:0 FAME/C14 alkene peak area ratio values in the first 5-minute fractions as illustrated by the error bars in Figure 4.7. In some cases, a C12:0 FAME/C14 alkene peak area ratio can be slightly below 0.75. This observation implies that some reactions may only reach completion after 5 minutes. However, it can be expected to be complete in the second and third 5-minute fractions because the C12:0 FAME/C14 alkane peak area ratios are more clustered around the mean.

4.3.4. Suitability of the flow system for transesterification

The fatty acid (FA) content of certified sunflower seed oil was determined in triplicate using the mostly 3D-printed continuous flow system, followed by GC-FID analysis. The FA content (expressed as a percentage of total FAMEs observed) for the fractions collected at 5, 10, and 15 minutes are summarized in Table 4.6. Single factor ANOVA was used to compare the FA content of the fractions collected at 5, 10, and 15 minutes. In other words, Single factor ANOVA was used to determine whether the FA content of each 5-minute fraction differs significantly at a 95% confidence level. Furthermore, the *F*-values (determined using MS Excel) is given in Table 4.6. The obtained results indicated that the composition of the three 5-minute fractions that were collected under optimized conditions did not differ significantly at a 95% confidence level, since the critical value (F_{crit} = 5.14) exceeded the test statistic for each FA. Therefore, only the data for samples collected in the second fraction (10 minutes) will be considered here.

Results were compared to certified values and experimental results obtained from batch reactions (Table 4.7). The relative error observed for the reactions performed in batch and flow were similar and less than 5%, except for stearic acid (C18:0), which had larger relative errors in batch. Since the experiments for the reactions performed in flow yielded results with relative errors below 5%, it was concluded that the 3D-printed flow system could be used to determine FA content with sufficient accuracy. The relative standard deviations shown in Table 4.7 also

indicate that the precision of both the batch and flow reactions were acceptable. Markedly, the precision of the continuous flow method is comparable with the batch reaction with a higher catalyst concentration.

Table 4.6: *Fatty acid content of certified sunflower oil as determined for fractions collected at 5-minute intervals. The calculated test statistic (F-value) for each fatty acid is also shown.*

Replicate	Fraction (min)	C16:0 (%)	C18:0 (%)	C18:1 (%)	C18:2 (%)
1	5	6.86	3.35	30.75	58.53
2	5	6.33	3.46	30.53	58.35
3	5	7.57	3.23	30.10	58.70
1	10	6.56	3.47	30.45	58.64
2	10	6.37	3.45	30.20	58.02
3	10	6.53	3.50	30.52	58.84
1	15	6.40	3.50	30.51	58.60
2	15	6.35	3.48	30.41	58.24
3	15	6.42	3.46	30.44	58.58
F-value		1.81	3.44	0.10	0.03

Table 4.7: *Comparison of the certified fatty acid content in sunflower seed oil from Helianthus annuus and values obtained experimentally by making use of an automated flow system followed by GC analysis. The experimental results represent the mean value of three replicates, together with the relative standard deviation.*

Fatty acid	Certified values	Experimental Results (%)[a]			Relative error (%)		
		Flow (1 wt.%)[b]	Batch (1 wt.%)	Batch (5 wt.%)	Flow (1 wt.%)[b]	Batch (1 wt.%)	Batch (5 wt.%)
C16:0	6.5	6.48 ± 0.02	6.68 ± 0.04	6.39 ± 0.02	-0.2	2.8	-1.7
C18:0	3.6	3.47 ± 0.01	3.21 ± 0.06	3.26 ± 0.04	-3.5	-10.7	-9.4
C18:1	30.6	30.39 ± 0.01	30.29 ± 0.03	30.78 ± 0	-0.7	-1.0	0.6
C18:2	56.8	58.5 ± 0.01	58.07 ± 0.02	59.4 ± 0.01	3.0	2.2	4.6

[a] *Expressed as percentage of total FAMEs observed.* [b] *Results obtained for the second 5-minute fraction.*

Thorough investigation of the fatty acid content typically found in edible oils, revealed that lauric acid (C12:0) was reported in discernible amounts for sunflower seed oil [16] and avocado oil [17]. Specifically, values ≤0.1 have been reported for this fatty acid in sunflower seed oil according to the Codex Standard for named vegetable oils [16]. This poses a significant problem for method validation, since methyl laurate (C12:0 FAME) is produced from glyceryl tridodecanoate which is one of the internal standards used. Glyceryl tridodecanoate was a much less expensive internal standard in comparison to glyceryl triundecanoate.

In order to preserve the integrity of method validation, it had to be determined if methyl laurate (C12:0 FAME) was present in all edible oils (certified and commercial). A solution of each diluted oil was prepared individually excluding all internal standards and derivatized under optimized batch mode reaction conditions (i.e., 5 wt.% sodium methoxide). The samples were then analyzed by GC-FID.

Fortunately, the C12:0 FAME was not detected in all edible oils. Therefore, the use of glyceryl tridodecanoate as an internal standard does not compromise the integrity of this work. However, it is recommended that in future glyceryl triundecanoate should be used as recommended in literature [9,10]. Because undecyclic acid (C11:0) is not naturally found in edible plant oils, since FAs from plants usually contain even numbered carbon atoms [18].

4.3.5. Gas chromatographic results and interpretation

The GC-FID chromatograms of the analyzed edible oils are shown in Figures 4.8. In the first five minutes the solvent eluted and was excluded in Figure 4.8. The inert internal standard, 1-tetradecene (14:1 HC), was first eluted at around 5.96 min, followed by internal standards methyl nonanoate (C9:0 FAME) and methyl laurate (C12:0 FAME). These two internal standards had retention times of approximately 6.31 min and 8.03 min, respectively. Methyl palmitate (C16:0 FAME) had a retention time of approximately 10.41 min on average. Methyl palmitoleate (C16:1 FAME) was tentatively identified with a retention time of about 10.58 min. Avocado oil was the only analyzed oil that contained a notable amount of this fatty acid (Figure 4.8A). However, extra virgin olive oil contained a relatively small amount of this fatty

acid (Figure 4.8D). Methyl stearate (C18:0 FAME), methyl oleate (C18:1 FAME), methyl linoleate (C18:2 FAME), and methyl linolenate (C18:3 FAME) had retention times of approximately 11.76 min, 12.00 min, 12.40 min, and 13.02 min, respectively. It can be seen that avocado oil and extra virgin olive oil (Figure 4.8A and 4.8D) contained low amounts of linolenic acid (C18:3) since the peaks for its corresponding FAME were broad with low peak heights. Furthermore, canola oil and the canola and olive oil blend (Figure 4.8 B and 4.8C) were observed to contain higher amounts of linolenic acid (C18:3) compared to the other analyzed oils (Figure 4.8A and 4.8D to 4.8F). All peaks of interest were of Gaussian shape with no coelution. Furthermore, there was no fronting or tailing observed for the peaks of interest.

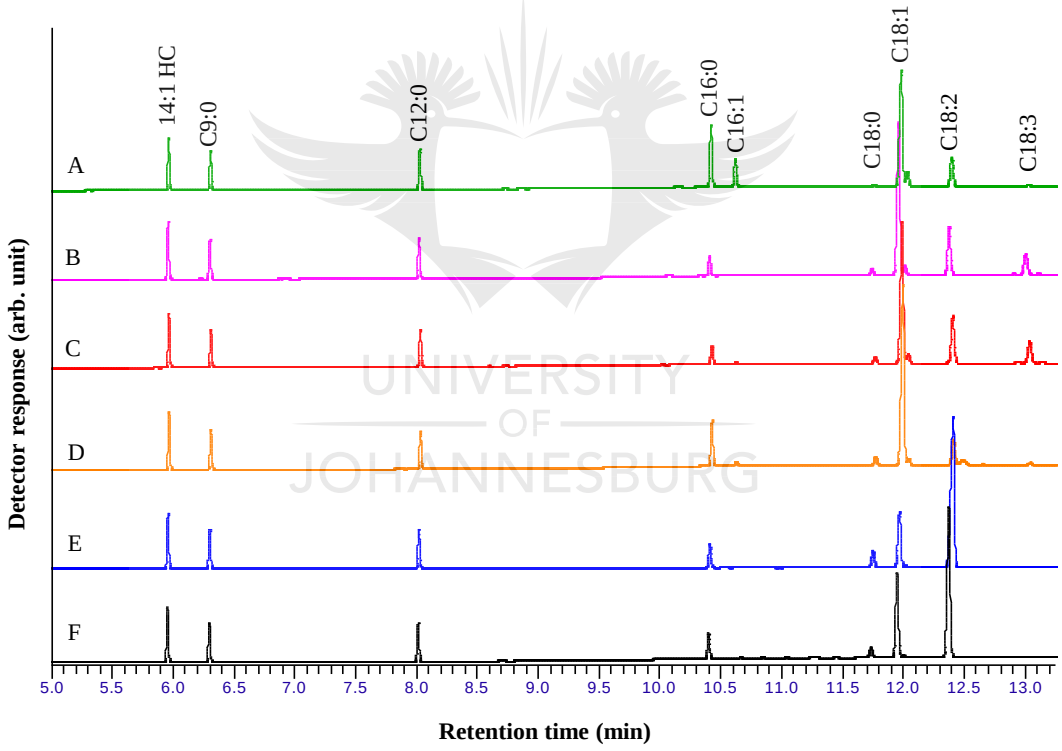

Figure 4.8: *GC-FID chromatograms of (A) avocado oil, (B) canola and olive oil blend, (C) canola oil, (D) extra virgin olive oil, (E) commercial sunflower oil, and (F) certified sunflower oil.*

4.3.6. Fatty acid content of commercial edible oils

The continuous flow system was also used to determine the FA content of commercial edible oils (Figure 4.9 and Table D2). No saponification was observed in any of the reactions. The transesterification was complete for all the oils except the canola and olive oil blend (see Appendix D, Table D1). Consequently, the sodium methoxide concentration was increased slightly to 1.5 wt.% to drive the reaction to completion.

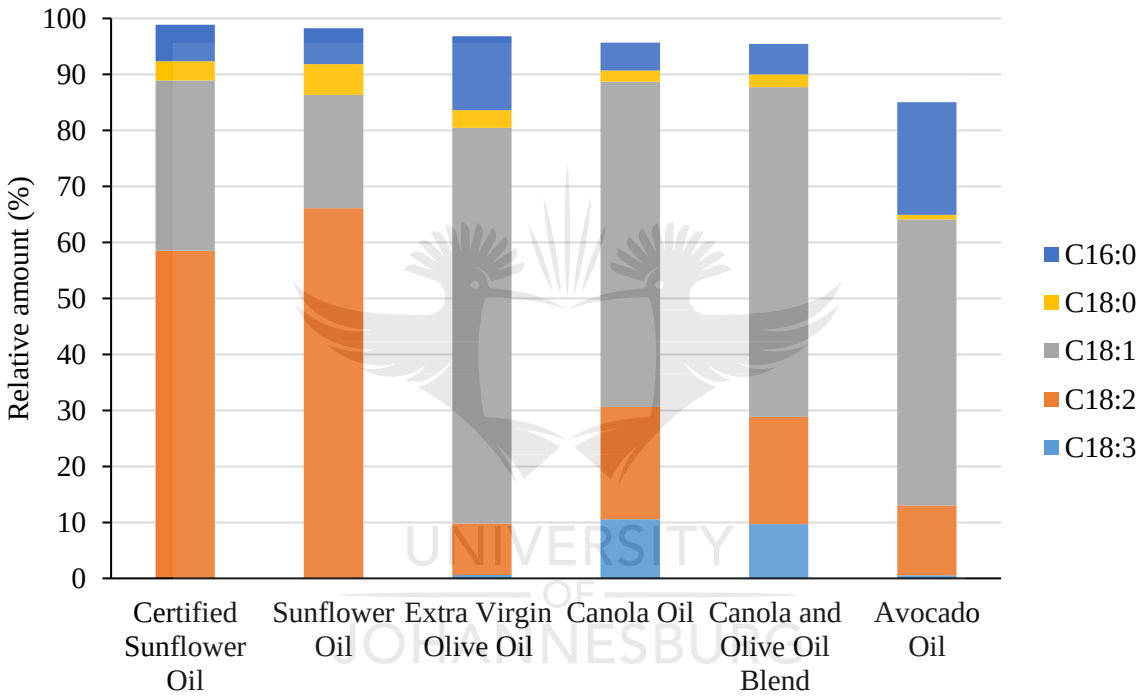

Figure 4.9: *Fatty acid composition of edible oils, based on the percentage of FAMEs observed. The relative amounts represent the average of three replicate fractions collected during the second 5-minute interval. A 1 wt.% sodium methoxide concentration was used for all oils, except for the canola and olive oil blend which required a 1.5 wt.% concentration to achieve complete transesterification.*

The FA content of the sunflower and canola oil fall within the established ranges of the Codex Standard for named vegetable oils (CX-STAN 210 1999) [16]. Additionally, the obtained FA content of sunflower and canola oil is similar to the values reported by Zimmerman et al. [19] and Matthaus et al. [20], respectively. Moreover, the FA content of extra virgin olive oil is in

complete agreement with the European Union statements [21] and the Codex Standard for olive oil, virgin and refined, and for refined olive-pomace (CODEX STAN 33-1981 (Rev. 1-1989)) [22]. Since avocado oil has a FA composition similar to olive oil, and there are no internationally established parameters defining the quality of avocado oil, the Codex Standard for olive oil [22] suffices as a reference [17].

The observed relative amounts of stearic acid (C18:0), linoleic acid (C18:2), and linolenic acid (C18:3) of the analyzed avocado oil agreed with the established ranges of the Codex Standard for olive oil [22]. The relative amount of palmitic acid (C16:0) slightly exceeded the range of the Codex Standard [22] by approximately 0.1%. However, values for this saturated FA can be as high as 29% [23]. The oleic acid (C18:1) value (~51%) was below the Codex Standard minimum of 55% [22]. Tan et al. [24] reported similar values for this monosaturated FA; however, Santana et al. [25] and Rydlewski et al. [26] reported lower oleic acid concentrations of 46% to 48%, respectively. Methyl palmitoleate (C16:1 FAME) was only tentatively identified and was therefore not included in Figure 4.9. This monounsaturated FA (C16:1) presented a value of approximately 10%, which is higher than the established maximum of olive oil (3.5%) [22]. However, similar values have been published for avocado oil elsewhere [17]. It has been reported that the geographical conditions in which the avocado fruit was grown accounts for variations in FA content [17,24,26].

Sunflower seed oil can be categorized as regular or high-linoleic, mid-oleic, and high-oleic [16,27]. The polyunsaturated FA, linoleic acid (C18:2), was the major component in both the certified and commercial sunflower oil. Based on this, these oils are of the regular (high-linoleic) type. The commercial sunflower oil contained relatively more linoleic acid (C18:2) in comparison to the certified oil, 66%, and 58%, respectively. The certified oil contained relatively more oleic acid (C18:1) compared to the commercial version. Both types of sunflower oils had similar amounts of palmitic acid (C16:0) and linolenic acid (C18:3), 6% and <0.1%, respectively.

The other commercial oils were high (>50%) in oleic acid (C18:1). Avocado oil had the highest palmitic acid (C16:0) content (~19%), followed by extra virgin olive oil (~13%), sunflower oil,

and canola oil, 6% and 5%, respectively. All oils contain very low levels of (<1%) linolenic acid (C18:3), except canola oil, which contained on average approximately 10%. The FA profile of the canola and olive oil blend closely resembles that of canola oil. This suggests that the blend consists mainly of canola oil, which corresponds with the label on the bottle, which stated that it is a mixture of 90% canola oil and 10% olive oil.

4.4. References

[1] A.S. Booeshaghi, E.d.V. Beltrame, D. Bannon, J. Gehring, L. Pachter, Principles of open source bioinstrumentation applied to the poseidon syringe pump system, Scientific Reports. 9 (2019) 1–8. https://doi.org/10.1038/s41598-019-48815-9.

[2] B. Wijnen, E.J. Hunt, G.C. Anzalone, J.M. Pearce, Open-source syringe pump library, PLoS ONE. 9 (2014). https://doi.org/10.1371/journal.pone.0107216.

[3] M.S. Cubberley, W.A. Hess, An inexpensive programmable dual-syringe pump for the chemistry laboratory, Journal of Chemical Education. 94 (2017) 72–74. https://doi.org/10.1021/acs.jchemed.6b00598.

[4] J.R. Lake, K.C. Heyde, W.C. Ruder, Low-cost feedback-controlled syringe pressure pumps for microfluidics applications, PLoS ONE. 12 (2017). https://doi.org/10.1371/journal.pone.0175089.

[5] J.M. Neumaier, A. Madani, T. Klein, T. Ziegler, Low-budget 3D-printed equipment for continuous flow reactions, Beilstein Journal of Organic Chemistry. 15 (2019) 558–566. https://doi.org/10.3762/bjoc.15.50.

[6] A.J.N. Price, A.J. Capel, R.J. Lee, P. Pradel, S.D.R. Christie, An open source toolkit for 3D printed fluidics, Journal of Flow Chemistry. (2020). https://doi.org/10.1007/s41981-020-00117-2.

[7] J.H. Bannock, S.H. Krishnadasan, M. Heeney, J.C. de Mello, A gentle introduction to the noble art of flow chemistry, Materials Horizons. 1 (2014) 373–378. https://doi.org/10.1039/c4mh00054d.

[8] E. Ballesteros, M. Gallego, M. Valcárcel, Automatic method for on-line preparation of fatty acid methyl esters from olive oil and other types of oil prior to their gas chromatographic determination, Analytica Chimica Acta. 282 (1993) 581–588. https://doi.org/10.1016/0003-2670(93)80123-3.

[9] B. Suter, K. Grob, B. Pacciarelli, Determination of fat content and fatty acid composition through 1-min transesterification in the food sample; principles, Z Lebensm Unters Forsch A. 204 (1997) 252–258. https://doi.org/https://doi.org/10.1007/s002170050073.

[10] B. Schilling, R. Bolliger, G. Boehm, Automated Workflow for the Transesterification of Fatty Acid Methyl Esters (FAME) in Fat and Fat Containing Food Samples Using a 90 Sec. Transesterification, https://www.palsystem.com/fileadmin/public/docs/Downloads/Posters/Automated_Generation___Analysis_of_FAME_GC_ISCC_Riva_2014_Poster.pdf (accessed September 30, 2020).

[11] U. Schuchardt, R. Sercheli, R.M. Vargas, Transesterification of vegetable oils: a review, Journal of the Brazilian Chemical Society. 9 (1998) 199–210. https://doi.org/10.1590/S0103-50531998000300002.

[12] Chemical Resistance Chart, (2010) 1–13. https://www.emerson.com/documents/automation/handbook-chemical-resistance-chart-rosemount-en-70768.pdf (accessed June 30, 2021).

[13] S.B. Ötvös, I.M. Mándity, F. Fülöp, Highly efficient 1,4-addition of aldehydes to nitroolefins: Organocatalysis in continuous flow by solid-supported peptidic catalysts, ChemSusChem. 5 (2012) 266–269. https://doi.org/10.1002/cssc.201100332.

[14] M.R. Penny, N. Tsui, S.T. Hilton, Extending practical flow chemistry into the undergraduate curriculum via the use of a portable low-cost 3D printed continuous flow system, Journal of Flow Chemistry. 11 (2021) 19–29. https://doi.org/10.1007/s41981-020-00122-5.

[15] F.M. Akwi, P. Watts, Continuous flow chemistry: where are we now? Recent applications, challenges and limitations, Chemical Communications. 54 (2018) 13894–13928. https://doi.org/10.1039/c8cc07427e.

[16] C. Alimentarius, Codex Standard for named vegetable oils. CX-STAN 210-1999, Codex Aliment. 8 (2001) 11–25. http://www.fao.org/3/y2774e/y2774e04.htm#bm4.1 (accessed March 10, 2021).

[17] M. Flores, C. Saravia, C.E. Vergara, F. Avila, H. Valdés, J. Ortiz-Viedma, Avocado oil: Characteristics, properties, and applications, Molecules. 24 (2019) 1–21. https://doi.org/10.3390/molecules24112172.

[18] H.D. Waktola, A.X. Zeng, S.-T. Chin, P.J. Marriott, Advanced gas chromatography and mass spectrometry technologies for fatty acids and triacylglycerols analysis, TrAC Trends in Analytical Chemistry. 129 (2020) 115957. https://doi.org/10.1016/j.trac.2020.115957.

[19] D.C. Zimmerman, G.N. Fick, Fatty acid composition of sunflower (Helianthus annuus L.) oil as influenced by seed position, JAOCS, Journal of the American Oil Chemists' Society. 50 (1973) 273–275. https://doi.org/10.1007/BF02641352.

[20] B. Matthaus, M.M. Özcan, F. al Juhaimi, Some rape/canola seed oils: fatty acid composition and tocopherols, Zeitschrift Für Naturforschung C. 71 (2016) 73–77. https://doi.org/10.1515/znc-2016-0003.

[21] EUR-Lex. Commission Implementing Regulation (EU) no. 1348/2013 of 16 December 2013 amending Regulation (EEC) no. 2568/91 on the characteristics of olive oil and olive-residue oil and on the relevant methods of analysis. https://eur-lex.europa.eu/legal-content/GA/TXT/?uri=CELEX:32013R1348 (accessed March 10, 2021).

[22] C. Alimentarius, Codex standard for olive oil, virgin and refined, and for refined olive-pomace oil. CODEX-STAN 33-1981 (Rev. 1-1989), Codex Aliment. 8 (2001) 25–39. http://www.fao.org/3/y2774e/y2774e04.htm#bm4.2 (accessed March 10, 2021).

[23] E.R. Abaide, G.L. Zabot, M.V. Tres, R.F. Martins, J.L. Fagundez, L.F. Nunes, S. Druzian, J.F. Soares, V. Dal Prá, J.R.F. Silva, R.C. Kuhn, M.A. Mazutti, Yield, composition, and antioxidant activity of avocado pulp oil extracted by pressurized fluids, Food and Bioproducts Processing. I02 (2017) 289–298. https://doi.org/10.1016/j.fbp.2017.01.008.

[24] C.X. Tan, S.S. Tan, S.T. Tan, Influence of Geographical Origins on the Physicochemical Properties of Hass Avocado Oil, Journal of the American Oil Chemists' Society. 94 (2017) 1431–1437. https://doi.org/10.1007/s11746-017-3042-7.

[25] I. Santana, V.N. Castelo-Branco, B.M. Guimarães, L.d.O. Silva, V.O.D.S. Peixoto, L.M.C. Cabral, S.P. Freitas, A.G. Torres, Hass avocado (Persea americana Mill.) oil enriched in phenolic compounds and tocopherols by expeller-pressing the unpeeled microwave dried fruit, Food Chemistry. 286 (2019) 354–361. https://doi.org/10.1016/j.foodchem.2019.02.014.

[26] A.A. Rydlewski, J.S. Pizzo, L.P. Manin, M.B. Galuch, P.D.S. Santos, C. Zapiello, O.O. Santos, J. v. Visentainer, Evaluation of possible fraud in avocado oil-based products from the composition of fatty acids by GC-FID and lipid profile by ESI-MS, Chemical Papers. 74 (2020) 2799–2812. https://doi.org/10.1007/s11696-020-01119-z.

[27] M.A. Grompone, Sunflower Oil, 2nd ed., Wiley-Blackwell, Oxford, UK, 2011. https://doi.org/10.1002/9781444339925.ch5.

Chapter 5: Conclusion

5.1. Conclusion

The versatility and cost-saving capabilities of 3D-printing technology were demonstrated by producing an inexpensive flangeless fittings kit consisting of syringe adapters, flangeless nuts, male Luers, unions, and mixers that are often used in continuous flow systems. The kit was reproducible in both PLA and PP, although only PP components were used in the flow system presented here. The flangeless fittings kit can be printed in PP for a total material cost of ZAR 66.63 (<USD 5.00) in approximately 22 hours. Besides reducing costs significantly, the 3D-printed flangeless fittings kit presents an added advantage of easily replacing misplaced or damaged commercial pieces, or the entire kit can be used independently. The fittings printed in PP could be reused several times but have a finite lifetime. Another disadvantage of this fabrication method was the need to purchase commercial flangeless ferrules, which were too small to 3D-print with FDM. The continuous flow system was further expanded by the addition of 3D-printed PP reactors that were compatible with the 3D-printed fittings. This was accomplished by modifying original designs by Neumaier et al. [1]. A design and modification protocol for the fabrication of all 3D-printed flow components were demonstrated, illustrating the complexity of fine-tuning PP print settings. The 3D-printed flow components can be assembled in a variety of configurations, increasing its application potential in flow chemistry. Importantly, the flow components were made entirely from PP, giving the best thermal stability and chemical resistance possible until 3D-printing in PEEK is more accessible.

The open-source Poseidon syringe pump system [2] was used for fluid delivery. The syringe pumps were individually calibrated. Each syringe pump was found to produce sufficiently reliable and accurate flow rates. In addition, the open-source Poseidon syringe pump system contributed to lowering the overall costs of the flow system even more.

A well-known derivatization technique, namely transesterification, was explored using the automated flow system to determine the fatty acid content of edible oils. Two base-catalysts were initially investigated: Sodium methoxide and potassium carbonate. Potassium carbonate

gave unfavourable results (in batch and flow mode) and therefore the remainder of this work focussed on using sodium methoxide as a base-catalyst. Reaction parameters (flow rate and base-catalyst concentration) were optimized. Importantly, the flow rates of each reagent had a notable effect on limiting the undesired saponification side reaction (i.e., solid formation). Furthermore, lower base-catalyst concentration (1-1.5 wt.%) were required to achieve complete transesterification using the automated flow method compared to the sodium methoxide (in methanol) batch mode procedure due to enhanced reactivity in flow. Based on the comparison of the fatty acid content of certified sunflower oil and commercial edible oils (sunflower oil, avocado oil, canola oil, extra virgin olive oil, and a blend of canola and olive oil) to certified and literature values, respectively, demonstrated that the 3D-printed flow system was suitable for performing automated transesterification reactions. This methodology required minimal manual intervention. Specifically, the preparation of reagent mixtures and the transferring of FAME products to GC vials for analysis had to be performed manually. The throughput of the automated flow system was increased by having multiple CSTRs on hand that can be replaced with a clean CSTR after use. Although fully automated robotic systems are commercially available and can be used to perform similar derivatization reactions, this 3D-printed semi-automated procedure is a cost-effective alternative for research laboratories.

In future, this semi-automated flow system can be fully automated by including a 3D-printed PP membrane separator [3] (see Chapter 2, Section 2.4.2.1) and interfacing the flow system with direct in-line analysis by GC-FID by purchasing commercial connectors. This methodology could still serve as an economically viable alternative compared to fully automated robotic systems. Furthermore, the three CSTRs can be replaced by a single 3D-printed PP chip reactor with a total of 5 access ports. The chip reactor will have to consist of two initial inlets with channels merging to a single reaction zone (to facilitate transesterification), followed by a heptane introduction zone (for extraction), a sodium citrate quenching zone, and a sample collection zone. Of course, an optional 3D-printed membrane separator and in-line analysis by GC-FID can be included if a fully automated system is desired. This methodology could potentially reduce the base-catalyst concentration and the amount of chemicals (i.e., heptane and sodium citrate) required to obtain complete transesterification even more. In addition, the flow system can possibly be adapted for extraction applications and consequently be compared to known sample preparation methods such as QuEChERS (quick, easy, cheap, effective, rugged, and safe) [4].

5.2. References

[1] J.M. Neumaier, A. Madani, T. Klein, T. Ziegler, Low-budget 3D-printed equipment for continuous flow reactions, Beilstein Journal of Organic Chemistry. 15 (2019) 558–566. https://doi.org/10.3762/bjoc.15.50.

[2] A.S. Booeshaghi, E. da V. Beltrame, D. Bannon, J. Gehring, L. Pachter, Principles of open source bioinstrumentation applied to the poseidon syringe pump system, Scientific Reports. 9 (2019) 1–8. https://doi.org/10.1038/s41598-019-48815-9.

[3] F. Menzel, T. Klein, T. Ziegler, J.M. Neumaier, 3D-printed PEEK reactors and development of a complete continuous flow system for chemical synthesis, Reaction Chemistry & Engineering. 5 (2020) 1300–1310. https://doi.org/10.1039/D0RE00206B.

[4] T. Rejczak, T. Tuzimski, A review of recent developments and trends in the QuEChERS sample preparation approach, Open Chemistry. 13 (2015) 980–1010. https://doi.org/10.1515/chem-2015-0109.

Appendix A. Poseidon syringe pump system installation and operation

This section serves as a simple and easy to follow guide for the installation and operation of the open-source Poseidon syringe pump system. The links to download the STL files for the 3D-printable hardware and a parts list are also included. A step-by-step installation protocol for the Arduino microcontroller and Python is potentially useful for anyone without prior experience. Additionally, the steps to open the controller program are also included. The reader is also referred to instructional videos for hardware assembly and syringe pump operation. The Raspberry Pi and microscope was excluded in this work and was therefore not described here.

A1. Hardware

The syringe pump 3D-printable components (i.e., STL files) and a detailed parts list can be downloaded at: https://github.com/pachterlab/poseidon/tree/release/HARDWARE

A2. Instructional videos

- Pump Assembly: https://www.youtube.com/watch?v=7YSiO6usR1M&ab_channel=SinaBooeshaghi
- Controller program operation: https://www.youtube.com/watch?v=VmoB_fPc4L4&ab_channel=SinaBooeshaghi

A3. Software for Arduino

- Arduino IDE software: https://www.arduino.cc/en/Main/Software
- Arduino sketch (Arduino_serialCOM_v0.1.ino) at: https://github.com/pachterlab/poseidon/tree/release/SOFTWARE/arduino_serialCOM_v0.1

- AccelStepper library for Arduino: http://www.airspayce.com/mikem/arduino/AccelStepper/AccelStepper-1.61.zip

A4. Arduino software installation

1. Install the Arduino IDE software.
2. Install the AccelStepper library (download zip file and do not unzip it).
    a. In Arduino IDE > Sketch > Include library > Add .ZIP library > select .zip file > Open.
    b. Sketch > Include library > Select AccelStepper.
3. Connect your Arduino Uno to your PC with a USB cable. Note green LED light.
4. Test:
    a. File > Examples > 0.1 Basics > Blink.
    b. Test > Board > Arduino Uno.
    c. Check Arduino Port connection: Tools > Port > COM5 (COM3 or higher is also acceptable).
    d. Click “Upload”.
    e. Wait a few seconds. Observe flashing lights labelled RX and TX on the borad. If the upload was successful, “Done uploading” will appear in the status bar.
    f. Pin 13 (L) LED will blink in orange.
5. File > Open > Browse to Arduino_serialCOM_v0.1.ino > click ok.
6. Click “Upload”. Take note of the “Done uploading” message in the status bar.

A5. Software for Python

- Python 3 (e.g., Python 3.9.5) at: https://www.python.org/downloads/windows/
- Poseidon_controller_gui.py and Poseidon_main.py at: https://github.com/pachterlab/poseidon/tree/release/SOFTWARE

A6. Python installation procedure

1. Python can be installed by double clicking on the python-3.X.Y.exe file. In the first window select “Add Python to PATH”.
2. Open Windows commander: Click on Start > type CMD > press Enter.
3. Execute the following in CMD:
    - python -m pip install PyQt5
    - python -m pip install pyqt5-tools
    - python -m pip install –upgrade pip
    - pip install pyserial
    - pip install opencv-python

A7. Procedure to open the controller program

1. Open the folder where “Poseidon_controller_gui.py” and “Poseidon_main.py” was saved.
2. Right click on Poseidon_main.py.
3. Edit with IDLE > click Edit with IDLE 3.X (32/64 bit).
4. Run > click Run module.
5. Wait a few seconds for the GUI to appear.

Appendix B. Poseidon syringe pump bill of materials and calibration

The bill of materials, including the suppliers and the item amounts required to reproduce the Poseidon syringe pumps is given in Table B1.

Table B1: *Poseidon syringe pump bill of materials.*

Item description	Amount	Supplier	Price per item (ZAR)	Total cost (ZAR)
Nema 17 stepper motor (0.65 Nm, 60 mm)	3	DIY Electronics	330.00	990.00
Flexible aluminium couplings (5 mm / 5 mm)	3	RS Components	39.95	119.85
Steel rod (length 200 mm, diameter 6 mm)	6	RS Components	350.13	84.03
Linear ball bearings (LM6UU, 6 mm diameter)	6	RS Components	26.95	161.70
Stainless steel threaded rod (M5 × 0.8, length 180 mm),	3	RS Components	392.07	54.11
M5 × 0.8 nut	6	RS Components	150.17	9.01
M3 × 0.5 socket head screws (length 20 mm)	12	RS Components	180.47	43.31
M3 × 0.5 socket head screws (length 10 mm)	6	RS Components	251.59	30.19
M3 nut	6	RS Components	115.58	6.93
M5 knob	3	RS Components	155.56	93.34
12 V power unit	1	Communica	250.00	250.00
Cable to power unit	1	Communica	33.53	33.53
Arduino Uno R3	1	DIY Electronics	145.00	145.00
CNC shield	1	DIY Electronics	59.00	59.00
A4988 stepper motor driver module	3	DIY Electronics	43.00	129.00
Connectors	3	Communica	1.27	3.81
Total (ZAR)				**2212.81**

A summary of the raw data collected from the calibration procedure (see Section 4.1.2) is provided in Table B2-B3.

Table B2: *Test result summary of a single pump using 1, 5, and 10 mL syringes. The flow rate was set to mL/hr in the Poseidon controller program.*

Syringe (mL)	Programmed flow rate (mL/hr)	Programmed flow rate (mL/min)	Time (s)	Volume (mL)	Observed flow rate (mL/min)	Observed flow rate (mL/hr)
1	62	1.03	60	0.98	0.98	59
	50	0.83	60	0.78	0.78	47
	37	0.62	60	0.58	0.58	35
	25	0.41	60	0.38	0.38	23
	12	0.21	60	0.19	0.19	11
	10	0.17	60	0.16	0.16	10
	8	0.13	60	0.13	0.13	8
	6	0.10	60	0.09	0.09	5
5	406	6.77	30	3.39	6.78	407
	325	5.41	30	2.74	5.48	329
	244	4.06	30	2.07	4.14	248
	162	2.71	30	1.41	2.82	169
	81	1.35	30	0.71	1.42	85
	60	1.00	30	0.52	1.04	62
	40	0.67	30	0.35	0.70	42
	20	0.33	30	0.17	0.34	20
10	582	9.70	60	9.99	9.99	599
	471	7.85	60	8.21	8.21	493
	353	5.89	60	6.06	6.06	364
	236	3.93	60	4.03	4.03	242
	118	1.96	60	2.07	2.07	124
	80	1.33	60	1.44	1.44	86
	40	0.67	60	0.72	0.72	43
	30	0.50	60	0.53	0.53	32

Table B3: *Test result summary of a single pump using 1, 5, and 10 mL syringes. The flow rate was set to mm/s in the Poseidon controller program.*

Syringe (mL)	Programmed flow rate (mm/s)	Programmed flow rate (mm/min)	Time (s)	Volume (mL)	Observed flow rate (mm/min)	Observed flow rate (mm/s)
1	1.00	60.00	60	0.99	59.40	0.99
	0.80	48.00	60	0.80	48.00	0.80
	0.60	36.00	60	0.59	35.40	0.59
	0.40	24.00	60	0.40	24.00	0.40
	0.20	12.00	60	0.21	12.60	0.21
	0.08	4.80	60	0.08	4.80	0.08
5	0.71	42.50	60	4.83	41.06	0,68
	0.61	36.50	60	4.08	34.68	0.58
	0.51	30.50	60	3.43	29.16	0.49
	0.41	24.50	60	2.64	22.44	0.37
	0.31	18.50	60	2.11	17.94	0.30
	0.21	12.50	60	1.50	12.75	0.21
	0.11	6.50	60	0.77	6.55	0.11
	0.07	4.10	60	0.50	4.25	0.07
	0.05	2.90	60	0.35	2.98	0.05
	0.03	1.70	60	0.21	1.79	0.03
10	0.95	57.00	60	9.79	55.80	0.93
	0.75	45.00	60	7.65	43.61	0.73
	0.55	33.00	60	5.58	31.81	0.53
	0.35	21.00	60	3.65	20.81	0.35
	0.15	9.00	60	1.50	8.55	0.14
	0.05	3.00	60	0.52	2.96	0.05
	0.03	1.80	60	0.32	1.82	0.03

Appendix C. 3D-printed flow components

The optimized PP and PLA print settings for all flow components are provided in Table C1 and Table C2. Table C1 summarizes the settings used for the Prusa i3 MK3S 3D-printer and Table C2 for the Creality CR20 Pro.

Table C1: *The optimized printing conditions for the fabrication of the flow components using PLA and PP as printing material. The flow components were fabricated using a Prusa i3 MK3S 3D-printer.*

Description	**Setting (PLA)**	**Setting (PP)**
Extruder temperature	195 °C	240 °C
Extruder flow	105%	105%
Infill	100%	100%
Printing bed temperature	60 °C	80 °C (with clear packing tape)
Speed	100%	100%
Support	None	Brim (larger devices)
Scale	5%	100%
Nozzle size	0.4 mm	0.4 mm
Layer resolution	0.05 mm	0.05 mm
Filament diameter (mm)	1.75	1.75
Minimum fan speed (%)	35	35
Maximum fan speed (%)	100	100
Travel speed (mm/s)	130	130
Infill speed (mm/s)	80	80

Table C2: *The optimized printing conditions for the fabrication of the flow components using PP as printing material. The flow components were fabricated using a Creality CR20 Pro 3D-printer.*

Description	Flangeless nuts and syringe adapters	Unions	CSTRs
Layer height (mm)	0.15	0.15	0.15
Shell thickness (mm)	0.8	0.8	0.8
Bottom/top thickness (mm)	1.2	1.2	1.2
Fill density (%)	100	100	100
Print speed (mm/s)	20	20	50
Print temperature (°C)	233	233	233
Bed temperature (°C)	80	80	85
Support type: Brim width (mm)	None	20	40
Filament diameter (mm)	1.75	1.75	1.75
Flow (%)	105	105	110
Nozzle (mm)	0.4	0.4	0.4
Travel speed (mm/s)	20	20	50
Bottom layer speed (mm/s)	20	20	50
Infill speed (mm/s)	20	20	50
Top/bottom speed (mm/s)	20	20	50
Inner shell speed (mm/s)	20	20	50
Minimum fan speed (%)	25	25	20
Maximum fan speed (%)	100	100	100

The components in the flangeless fittings kit were fabricated using clear PLA (Figure C1). Figure C2 shows the quality of threaded parts printed in PLA in comparison with threaded parts printed in PP. Even though the threading is better defined when printed in PLA, the flexibility of PP ensured that leak-tight fittings were obtained.

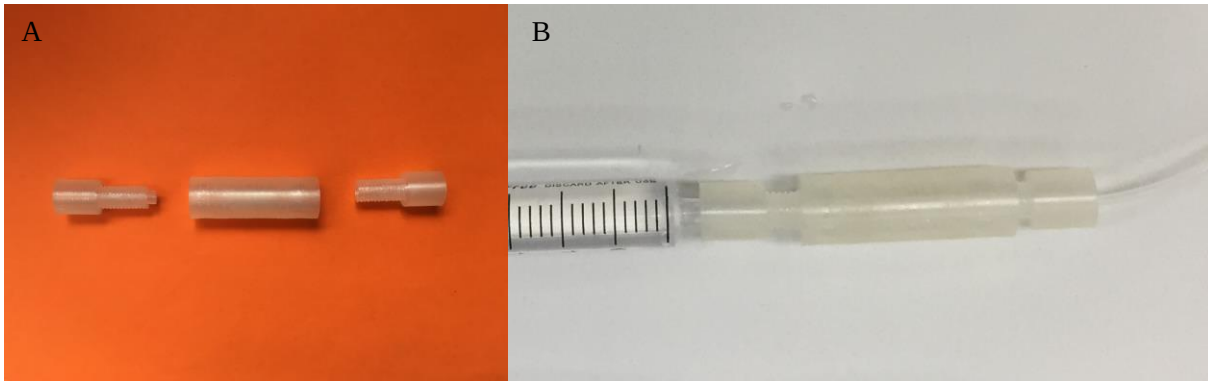

Figure C1: *Flangeless fittings kit 3D-printed using PLA as printing material. (A) Syringe adapter, union, and a flangeless nut (left to right). (B) Fittings from A connected to a syringe and tubing for use in a flow system.*

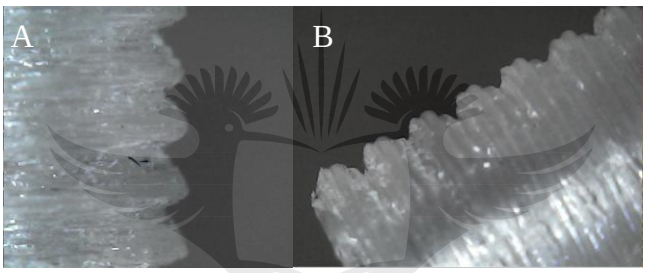

Figure C2: *A comparison between the threading of a 3D-printed flangeless nut in (A) PLA, and (B) PP.*

Appendix D. Transesterification

The internal standard peak area ratios (C9:0 FAME/C14 alkene and C12:0 FAME/C14 alkene) are summarized in Table D1. The mean values of three replicates together with its standard deviation is given for all analyzed oils. All oils were derivatized using 1 wt.% sodium methoxide, except the canola and olive oil blend which required a concentration of 1.5 wt.% to reach completion.

Table D1: *C9:0 FAME/C14 alkene and C12:0 FAME/C14 alkene peak area ratios of the certified and commercial edible oils. The mean value of three replicates is shown together with its standard deviation.*

Commercial oil	**Fraction (min)**	**C9:0 FAME/C14 alkene ratio**	**C12:0 FAME/C14 alkene ratio**
Certified sunflower oil	5	0.73 ± 0.018	0.77 ± 0.031
	10	0.73 ± 0.011	0.77 ± 0.011
	15	0.72 ± 0.0066	0.78 ± 0.0077
Commercial sunflower oil	5	0.73 ± 0.016	0.79 ± 0.031
	10	0.72 ± 0.014	0.77 ± 0.012
	15	0.72 ± 0.011	0.79 ± 0.015
Avocado oil	5	0.73 ± 0.061	0.83 ± 0.044
	10	0.74 ± 0.025	0.78 ± 0.019
	15	0.70 ± 0.014	0.81 ± 0.030
Extra virgin olive oil	5	0.74 ± 0.021	0.75 ± 0.026
	10	0.75 ± 0.032	0.76 ± 0.0052
	15	0.76 ± 0.045	0.76 ± 0.015
Canola oil	5	0.76 ± 0.037	0.77 ± 0.021
	10	0.74 ± 0.0078	0.78 ± 0.0051
	15	0.77 ± 0.024	0.78 ± 0.021
Canola and olive oil blend	5	0.67	0.69[a]
	10	0.71	0.70[a]
	15	0.74	0.69[a]
	5	0.70 ± 0.025	0.78 ± 0.0019
	10	0.71 ± 0.016	0.78 ± 0.0020
	15	0.74 ± 0.0090	0.76 ± 0.010

[a] *Incomplete transesterification. Incomplete transesterification was obtained for the canola and olive oil blend when 1 wt.% sodium methoxide was used as a base-catalyst.*

Table D2 summarizes the determined fatty acid content of all oils analyzed using optimized reaction conditions in flow mode. Since similar results were obtained for all three 5-minute fractions (see Table 4.6), the results obtained for the 10-minute fraction is presented in Table D2.

Table D2: *Fatty acid content of edible oils. The mean value of three replicates is shown together with the standard deviation.*

Commercial oil	**C16:0**	**C18:0**	**C18:1**	**C18:2**	**C18:3**
Certified Sunflower Oil	6.48 ± 0.02	3.47 ± 0.01	30.39 ± 0.01	58.5 ± 0.01	0.01 ± 1.73
Sunflower Oil	6.38 ± 0.01	5.49 ± 0.01	20.23 ± 0.00	66.1 ± 0.00	0.01 ± 1.73
Extra Virgin Olive Oil	13.19 ± 0.06	3.18 ± 0.06	70.63 ± 0.01	9.19 ± 0.01	0.62 ± 0.08
Canola Oil	4.98 ± 0.00	2.04 ± 0.08	58.05 ± 0.00	20.1 ± 0.01	10.52 ± 0.00
Canola and Olive Oil Blend	5.42 ± 0.01	2.31 ± 0.02	58.86 ± 0.00	19.18 ± 0.00	9.68 ± 0.02
Avocado Oil	20.12 ± 0.01	0.79 ± 0.08	51.1 ± 0.01	12.44 ± 0.05	0.57 ± 0.11